NOTICE

The quality of this microform is heavily dependent upon the quality of the original thesis submitted for microfilming. Every effort has been made to ensure the highest quality of reproduction possible.

If pages are missing, contact the university which granted the degree.

Some pages may have indistinct print especially if the original pages were typed with a poor typewriter ribbon or if the university sent us an inferior photocopy.

Reproduction in full or in part of this microform is governed by the Canadian Copyright Act, R.S.C. 1970, c. C-30, and subsequent amendments.

AVIS

La qualité de cette microforme dépend grandement de la qualité de la thèse soumise au microfilmage. Nous avons tout fait pour assurer une qualité supérieure de reproduction.

S'il manque des pages, veuillez communiquer avec l'université qui a conféré le grade.

La qualité d'impression de certaines pages peut laisser à désirer, surtout si les pages originales ont été dactylographiées à l'aide d'un ruban usé ou si l'université nous a fait parvenir une photocopie de qualité inférieure.

La reproduction, même partielle, de cette microforme est soumise à la Loi canadienne sur le droit d'auteur, SRC 1970, c. C-30, et ses amendements subséquents.

PYRITE AND CHALCOPYRITE CATHODES FOR SECONDARY LITHIUM CELLS

by

Rosamaría Fong

B. Sc. (Honours), University of British Columbia, 1981.

A THESIS SUBMITTED IN PARTIAL FULFILLMENT OF
THE REQUIREMENTS FOR THE DEGREE OF
MASTER OF SCIENCE
in the Department
of
Chemistry

SIMON FRASER UNIVERSITY
December, 1987

ISBN 0-315-48717-8

APPROVAL

Name: Rosamaría Fong

Degree: Master of Science

Title of Thesis: Pyrite and Chalcopyrite Cathodes for Secondary Lithium Cells

Examining Committee:

Chairman: Dr. T. N. Bell

Dr. J. R. Dahn

Dr. C. H. W. Jones, Senior Supervisor

Dr. I. D. Gay

Dr. F. W. B. Einstein, Internal Examiner

Date approved: 16 Dec. 87

PARTIAL COPYRIGHT LICENSE

I hereby grant to Simon Fraser University the right to lend my thesis, project or extended essay (the title of which is shown below) to users of the Simon Fraser University Library, and to make partial or single copies only for such users or in response to a request from the library of any other university, or other educational institution, on its own behalf or for one of its users. I further agree that permission for multiple copying of this work for scholarly purposes may be granted by me or the Dean of Graduate Studies. It is understood that copying or publication of this work for financial gain shall not be allowed without my written permission.

Title of Thesis/Project/Extended Essay

PYRITE AND CHALCOPYRITE CATHODES FOR SECONDARY LITHIUM CELLS

Author: _____
(signature)

ROSAMARIA FONG
(name)

December 8/87.
(date)

ABSTRACT

Naturally occurring minerals such as pyrite (FeS_2), chalcopyrite ($CuFeS_2$), and materials synthesized from them have been investigated as cathode materials in lithium secondary batteries. The mechanism of the first discharge of Li/FeS_2 cells is both temperature and rate dependent. At near room temperature, and high discharge rate, the reaction proceeds via one-step, forming Li_2S and Fe. However, when the discharge rate is sufficiently slowed, and the temperature is increased to above 37°C, this reaction proceeds step-wise, forming Li_2FeS_2, which is amorphous when formed at these low temperatures. Single crystal X-ray diffraction determines this compound to have the structural characteristics of intercalation compounds. Its structure consists of hexagonal close-packed layers of sulfur with iron and lithium, equally and randomly, filling all of the tetrahedral interstices between two sulfur layers. The remaining lithium atoms fill the octahedral interstices between the adjacent sulfur layers.

The recharge of a Li/FeS_2 cell, which has been discharged to $x = 2$, shows behaviour which is similar to the first recharge of a cell fabricated with chemically synthesized Li_2FeS_2. Between the voltage range of 1.45 and 2.45 volts, the cell mechanism is intercalation. Above 2.45 volts, the hexagonal framework of Li_2FeS_2 decomposes, and disproportionation of the compound into a mixture of FeS_y and S occurs. Subsequent to a complete discharge to 1.0 volt, the cell chemistry and thermodynamics of both of these cells, as indicated by the $V(x)$ curves, are the same.

Chemical reaction of lithium with $CuFeS_2$ at elevated temperatures yields $LiCuFeS_2$, which is a member of the solid solution $Li_{2-x}Cu_xFeS_2$ where $0 < x \leq 1$. Single crystal X-ray diffraction determines this compound to be isostructural to Li_2FeS_2. Electrochemical and chemical removal of lithium from $Li_{2-x}Cu_xFeS_2$ result in well-defined Cu_xFeS_2 phases. The crystal structure determination of a partially delithiated $Li_{1-\delta}CuFeS_2$ phase, where $\delta = 0.35$, indicates that as lithium is removed, copper atoms diffuse into the tetrahedral sites of the lithium layer. Calorimetric data show that Cu_xFeS_2 phases are metastable, and upon heating, phase transitions back to the starting minerals, chalcopyrite and pyrite, occur.

To Kenneth

ACKNOWLEDGEMENTS

It is a great pleasure to thank my supervisor, Dr. Jeff Dahn, for his advice and guidance throughout the course of this project. His enthusiasm and encouragement in my work have been my inspiration and motivation. I also wish to express my sincere appreciation to Dr. Colin Jones for his discussions and comments during the completion of this work.

Special thanks to Dr. Fred Einstein, and Dr. Ray Batchelor for their interest and contribution to the crystallographic portion of the thesis. I have benefitted from many stimulating discussions with them.

To the entire research and development group at Moli Energy Ltd., I extend my gratitude for their willingness to discuss problems and provide prompt attention in the fabrication and maintenance of equipments.

I gratefully ackenowledge financial support from the Science Council of B. C. in the form of a postgraduate scholarship and Moli Energy Ltd.

Finally, I would like to thank my husband, Dr. Ken Fong, for his assistance in the preparation of this thesis, and specially for being my source of strength in this past year.

TABLE OF CONTENTS

LIST OF TABLES

LIST OF FIGURES

1 INTRODUCTION

1.1 The Electrochemical Cell

The fabrication of electrodes from lithium intercalation compounds has received considerable attention in recent years. High energy-density rechargeable electrochemical cells employing layered transition metal dichalcogenides, denoted by MX_2, (M = transition metal, X = chalcogen), as cathodes and lithium as the anode have about twice the energy density per unit weight of Nickel-Cadmium cells. The development of these systems has resulted in the first mass produced battery based on Li/MoS_2 (1).

Intercalation is the reversible insertion of guest species into a host without significant changes occurring in the host structure. Suitable hosts must have sites in their lattices which are accessible from the surface. Consequently, these materials generally have open passages through which intercalants can diffuse. In MX_2 materials, layers of metal atoms are sandwiched between layers of chalcogens. The adjacent planes of chalcogens are bonded together by weak van der Waals forces as shown in figure 1. Intercalant atoms diffuse into and occupy sites within the van de Waals' gaps between the MX_2 sandwiches. An electrochemical cell based on intercalation can be represented in the following way:

$$\text{Li /organic electrolyte containing } Li^+ \text{ ions/} Li_xMX_2$$

using MX_2 as the cathode and lithium as the anode. A schematic of such a cell is shown in figure 2. As the cell is discharged, two half-cell reactions occur. At the anode the lithium atoms dissociate into Li^+ ions and electrons.

$$x\ Li \rightleftharpoons x\ Li^+ + x\ e^- \qquad (1.1.1)$$

The Li^+ ions migrate through the electrolyte to the cathode. The electrons travel through the external circuit, and combine with the Li^+ ions at the surface of the MX_2 cathode to form lithium atoms, which diffuse into the cathode host structure.

$$x\ Li^+ + x\ e^- + MX_2 \rightleftharpoons Li_xMX_2 \qquad (1.1.2)$$

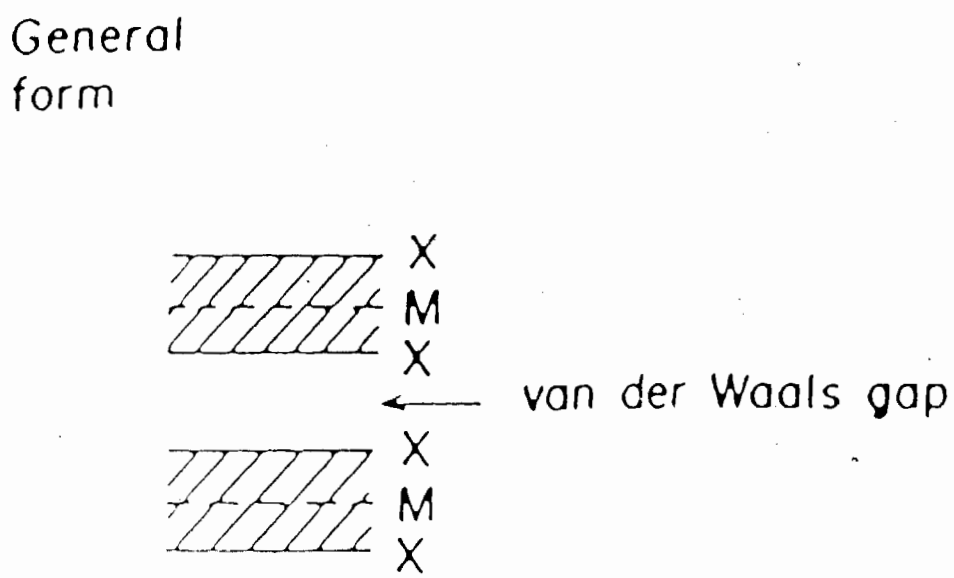

Figure 1: The general form of an MX_2 layer compound sandwich.

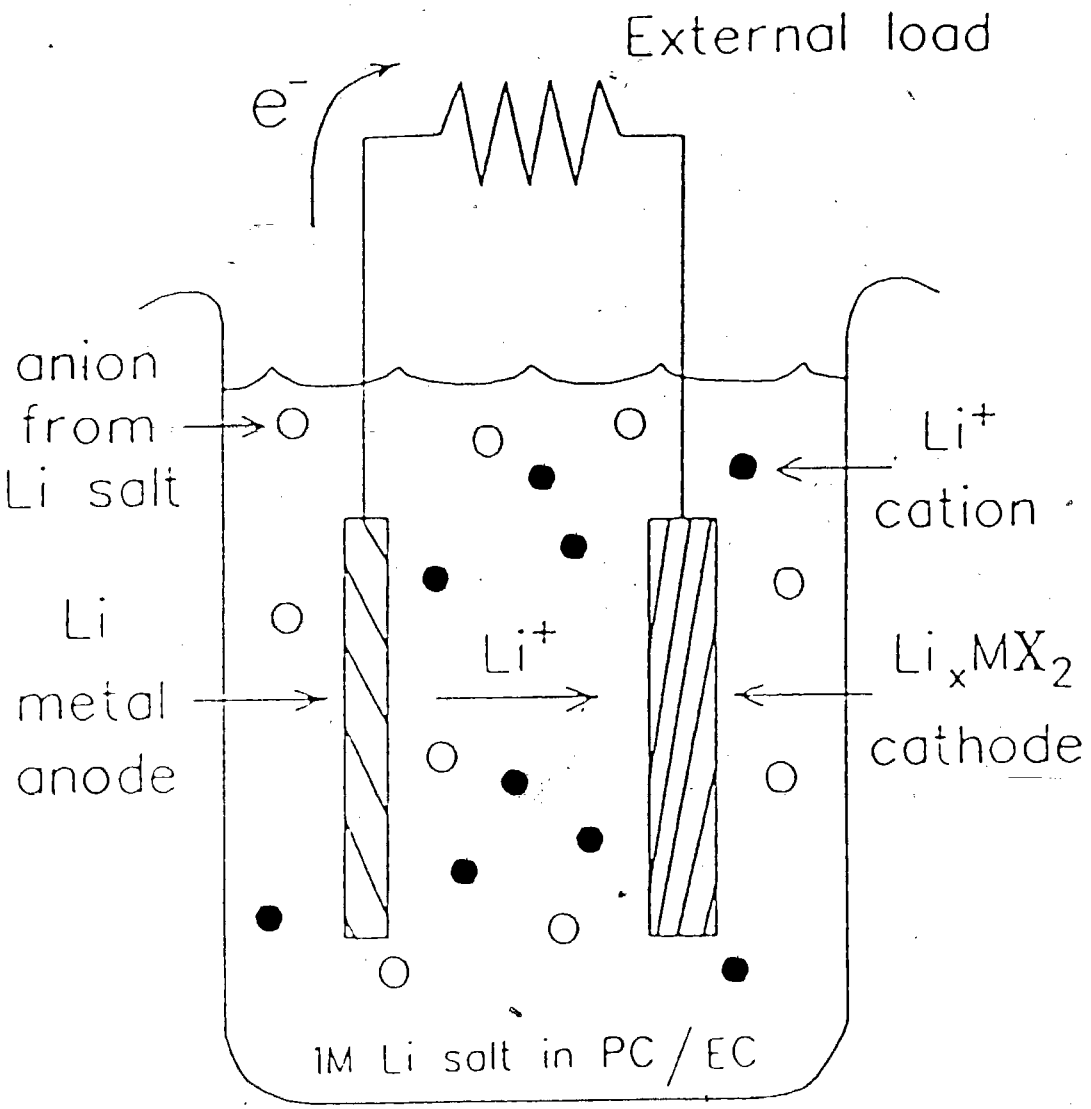

Figure 2: Schematic diagram of an intercalation cell. (PC and EC denote propylene carbonate and ethylene carbonate respectively.)

The overall reaction is the transfer of lithium atoms from the anode to the cathode.

$$x\,\mathrm{Li} + \mathrm{MX_2} \longrightarrow \mathrm{Li}_x\mathrm{MX_2} \tag{1.1.3}$$

The voltage across the cell can be expressed in terms of Δg, the change in partial molar free energy.

$$V = -\frac{\Delta g}{\mathrm{F}} \tag{1.1.4}$$

where F is Faraday's constant. Since Δg is defined to be the difference in chemical potential of the lithium atoms in the anode and cathode, μ_a and μ_c respectively, the voltage can also be expressed as

$$V = -\frac{(\mu_c - \mu_a)}{e} \tag{1.1.5}$$

where e is the magnitude of the electronic charge, and μ_a is a constant because the composition of the lithium anode is unchanged. Since the electrode reaction involves changes in the composition of the cathode, variations in the voltage as the cell charges and discharges result from changes in μ_c.

On recharge, a current is driven through the external circuit so that the electrons flow from the cathode to the anode. This causes Li^+ ions to migrate from the cathode to the anode where they combine with electrons and electroplate onto the lithium metal.

1.2 Pyrite and Chalcopyrite

Naturally occurring minerals such as pyrite (FeS_2) and chalcopyrite ($CuFeS_2$) are attractive electrode materials. These minerals have the desirable characteristics of reasonably low equivalent weight, low cost, abundance, and nontoxicity.

Much of the early work on the Li-Fe-S system was conducted by the Argonne National Laboratory to develop high power cells for vehicle propulsion. Studies showed that Li/FeS_2 cells have excellent reversibility at 450°C (2,3) and attempts were made to determine the compositions of the equilibrium intermediate $Li_xFe_yS_z$ phases formed during charge and discharge. This work resulted in the Li-Fe-S phase diagram at 450°C, shown in figure 3, which identified Li_2FeS_2 as one of the intermediate phases formed. The X-ray diffraction powder pattern was indexed with a hexagonal cell with a = 3.90 Å and c = 6.28 Å (3, 4, 5).

More recently, the behaviour of chemically synthesized Li_2FeS_2 was studied in lithium batteries at room temperature (6). Two intermediate hexagonal phases were identified and they were thought to have the CdI_2-type structure. By analogy with Li_xTiS_2 (7), the cycling mechanism was interpreted as intercalation of lithium between the layers in the van de Waals' gap. Although Li_2FeS_2 exhibited good electrochemical reversibility, electrical conductivity measurements showed it to be a poor conductor (8). On the other hand, substitution of copper for lithium ($Li_{2-x}Cu_xFeS_2$) increased conductivity by two orders of magnitude. This property of the copper substituted compound is particularly desirable as it decreases the internal resistance of the battery.

To date, information on the $Li_{2-x}Cu_xFe_2$ phase is limited. X-ray diffraction showed that substitution of copper to $x = \frac{2}{3}$ ($Li_{\frac{1}{3}}Cu_{\frac{2}{3}}FeS_2$) decreased a to 3.833 Å and increased c to 6.339 Å. The Mössbauer spectrum of this compound ressembled that of Li_2FeS_2 (5). Both showed two overlapping quadrupole doublets which suggested two non-equivalent iron sites in the hexagonal crystal structure.

Due to the complexity of the iron-sulfur system, even though phases

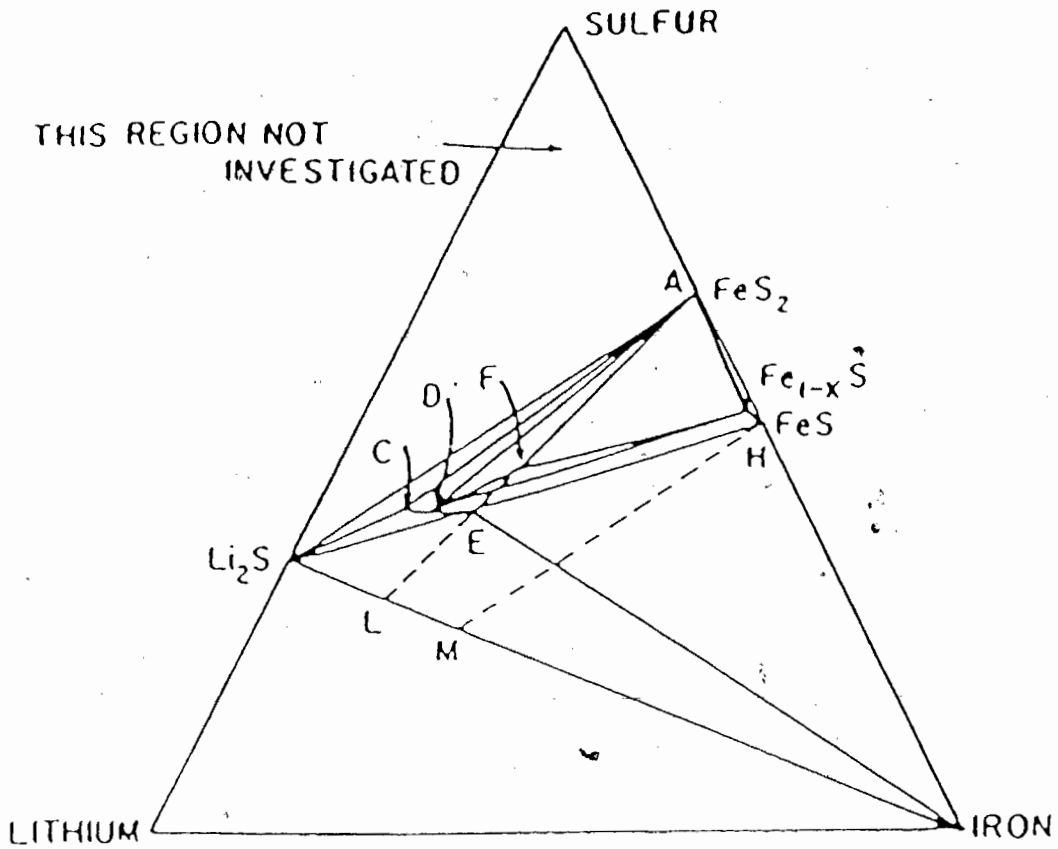

Figure 3: The Li-Fe-S phase diagram at 450°C (3).

in both the pyrite and chalcopyrite systems have been reported, little is known about their chemistry. But an understanding of their cell reactions, electrochemical behaviour, crystal structures, and physical properties is crucial for further development of these electrode materials.

2 EXPERIMENTAL PROCEDURES

2.1 Electrochemical Cell Fabrication

2.1.1 Cell Components

An electrochemical cell based on lithium intercalation is made up of four components: (1) the cathode, which is the host material for intercalation, (2) the lithium metal anode, (3) the electrolyte, and (4) the separator, which allows Li^+ ions to pass and prevents shorting of the electrodes. Each of these components requires special preparation so that their reactions with lithium metal are minimized. Otherwise, occurrences of such "side reactions" contribute to the electrochemical properties of the cells and can lead to misinterpretations of the behaviour of the host material under investigation.

Cathodes were prepared by mixing together ethylene carbonate (EC), polyethylene oxide (PEO; molecular weight 2,000,000), and the powdered material of interest in the proportions of 2:4:94 respectively. The powder was sifted through a 80-mesh sieve (180 μm) to prevent lumping. Dichloromethane was added to the mixture and stirred until a uniform slurry was obtained. An even layer was spread on the surface of a 0.0018 cm thick aluminum substrate, and evaporated to dryness. Cathodes were then pressed between a set of rollers to ensure good mechanical adhesion of the powder to the aluminum substrate, and cut to a suitable size for cell fabrication. The cathodes generally consisted of 30 to 40 mg of powdered material covering a 1.2 cm $\times$ 1.2 cm square substrate. Typical weight per unit area ranged from 20 to 30 mg/cm^2 . When air sensitive cathodes were prepared, the above process was carried out inside an inert atmosphere glove box.

Lithium foil (Foote) was used as received, and stored inside a sealed chamber in the glove box to prevent formation of lithium oxide or lithium hydroxide surface films. Anodes were made with 0.0127 cm thick lithium, cut to a size which covered the entire cathode surface.

The electrolyte was a 1M solution of lithium hexafluoroarsenate ($LiAsF_6$) in a 50:50 solvent mixture of propylene carbonate (PC) and EC by volume. These solvents were separately vacuum distilled to reduce moisture content and major impurities such as propylene glycol in PC and ethylene glycol in EC. Analyses of the purified solvents showed that this procedure reduced impurity levels to less than 20 ppm in propylene and ethylene glycol, and less than 30 ppm in water. The $LiAsF_6$ salt (U.S. Agric. Chemical) was used as received.

The separators used were Celgard #2500 microporous polypropylene films, cut into sheets that were larger than the cathode. They were immersed in the prepared electrolyte and wetted under 150 psi pressure to open the micropores.

2.1.2 Cell Assembly

Four different types of electrochemical cell were employed in the work of this thesis: (1) an experimental test cell, (2) a gas evolution cell, (3) an in-situ X-ray diffraction cell, and (4) an in-situ Mössbauer cell. These two-electrode cells were designed to meet the following requirements. The cathode and the anode must be electrically isolated. There must be sufficient pressure on the electrode surfaces to provide good electrical contact, and at the same time, minimize the internal resistance of the cell. The cell must fit within the constraints and specifications of the equipment and apparatus associated with each experiment. Finally, they must be sealed. Although the physical sizes and shapes of these cells are quite different, the assembly of each cell was basically the same.

Cell construction involved the assembly of a "cathode–separator–anode" sandwich between two stainless steel surfaces. The cathode mass was determined to $\pm$ 1 mg. Three to four drops of electrolyte were added to the cathode and a separator was placed on top. To complete the sandwich, a piece of anode was placed over the top of the separator. Figure 4 gives an exploded view of the cell. The two metal contact surfaces which hold the sandwich together are the positive and negative terminals of the cell.

As shown in figure 5, the electrical contacts of an experimental test cell were stainless steel plates. The spring assembly which is inserted into a Nickel-plated mild steel can, applies a 225 psi pressure on the cathode–separator–anode sandwich. Electrical isolation is achieved by the glass–to–metal seal between the anodic center pin and the rest of the cell. Welding around the rim of the cell gives a hermetic seal.

The gas evolution cell, shown in figure 6, consists of two stainless steel flanges which are held together by insulated screws (9). A narrow tube (0.07 cm ID, 15 cm length) extends through the top flange and is connected to the gas evolution apparatus. Tightening the bolts presses the two electrodes together, and compresses the O-ring sufficiently to make a gas tight seal.

The design of the in-situ X-ray diffraction cell used in this thesis was

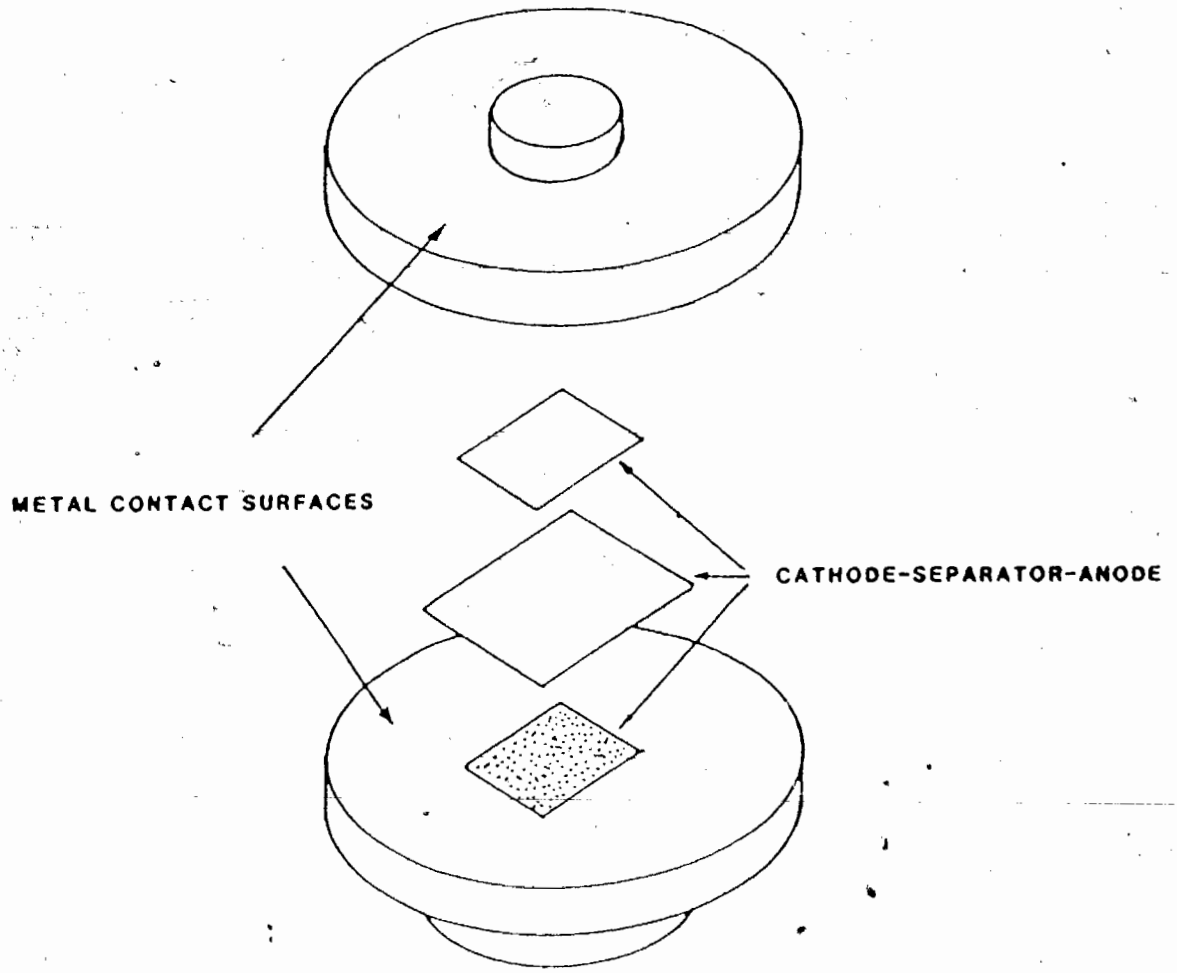

Figure 4: Exploded view of the "cathode-separator-anode" sandwich.

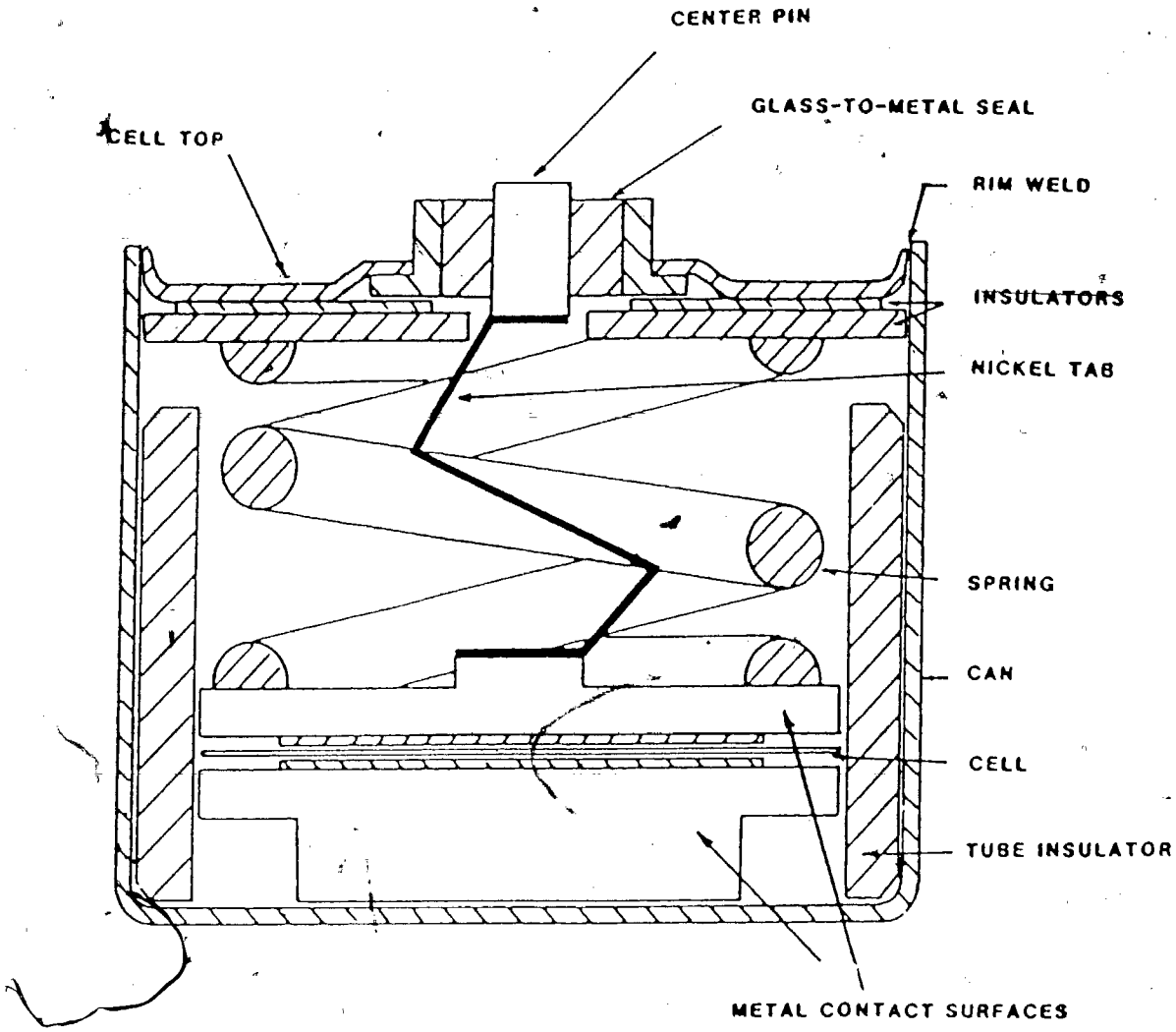

Figure 5: An experimental test cell.

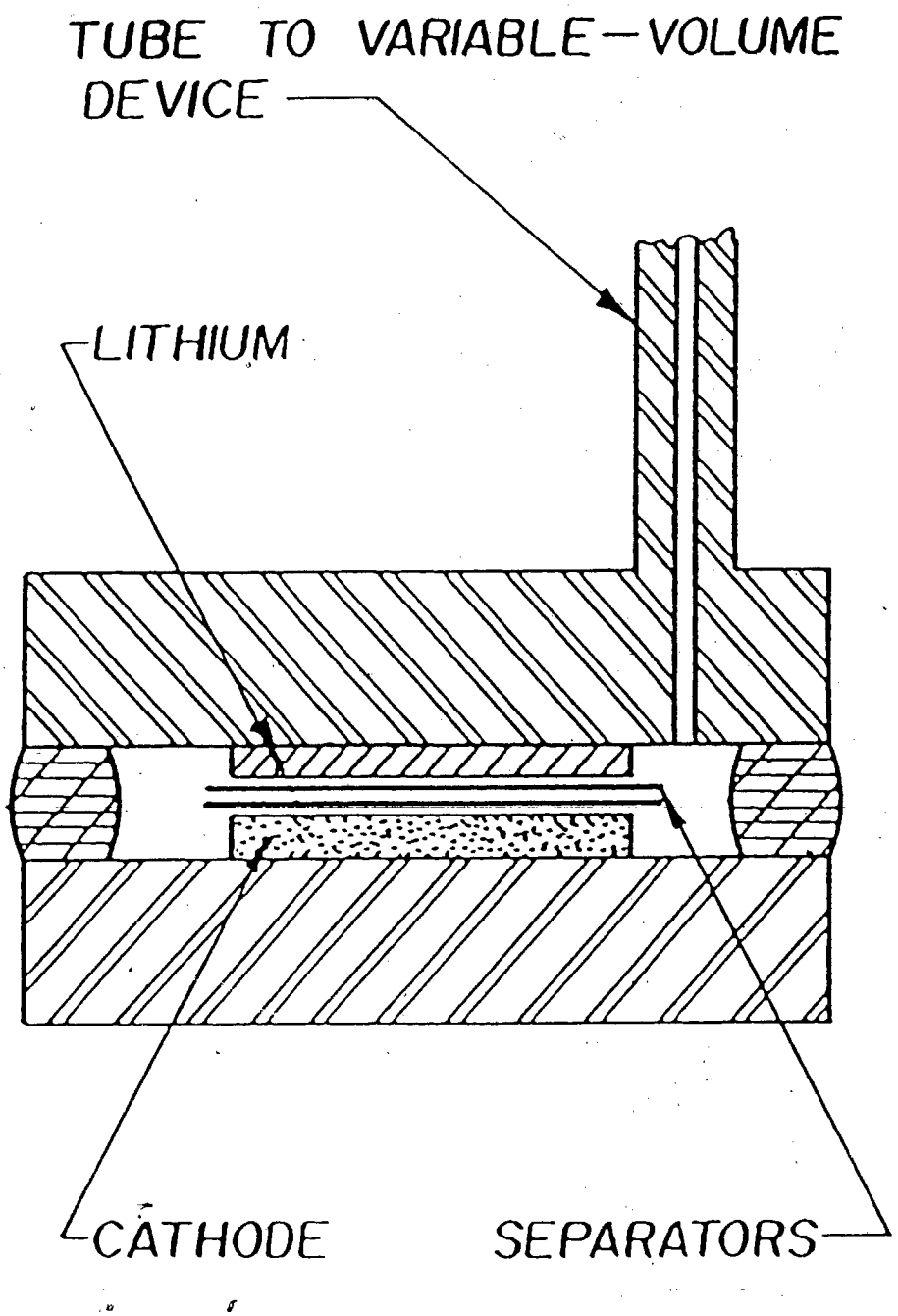

Figure 6: A gas evolution cell.

developed by Dahn et al. (10). The cell, shown in figure 7, was used to monitor changes in the cathode lattice while its composition was altered electrochemically. The top cover, made of brass, incorporates a 0.025 cm thick beryllium window in the recess on the bottom surface. The center beam in the cell top prevents the beryllium from flexing excessively. A 0.043 cm thick greased polypropylene gasket provides the gas tight seal between the top cover and the stainless steel cell base.

The in-situ Mössbauer cell is similar to the X-ray diffraction cell described above. The major difference between these cells is that the Mössbauer cell requires beryllium windows on both contact plates such that gamma ray can pass through the cell and into the detector. The cell, shown in figure 8, sits on top of the detector mount, which is equipped with heaters and a temperature sensor so that the cell can be operated at elevated temperatures. The flexing of the beryllium windows, which causes uneven pressure on the electrode surfaces, results in poor electrical contact. Typically, cathode utilization, which is the percentage of the cathode that is electrically connected, is approximately 70 to 75%. Poor cathode utilization of in-situ Mössbauer cells is difficult to overcome.

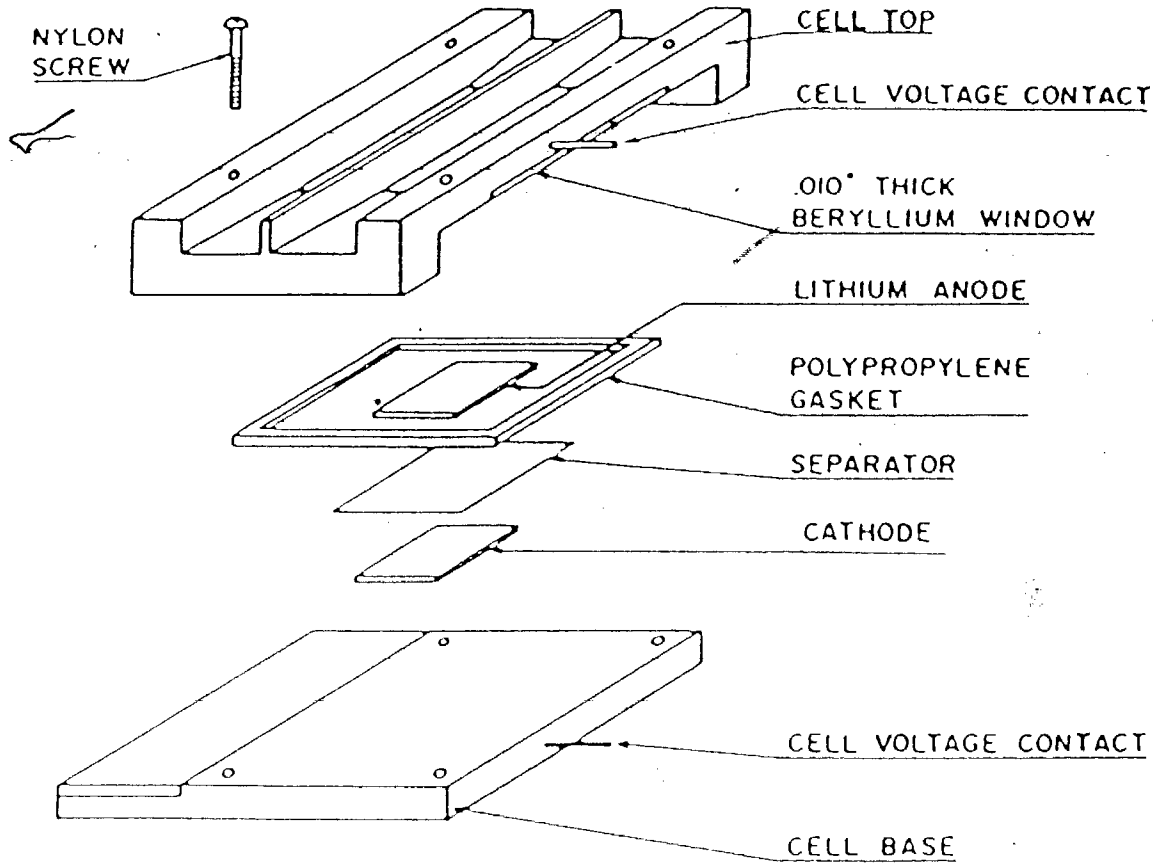

Figure 7: An in-situ X-ray diffraction cell.

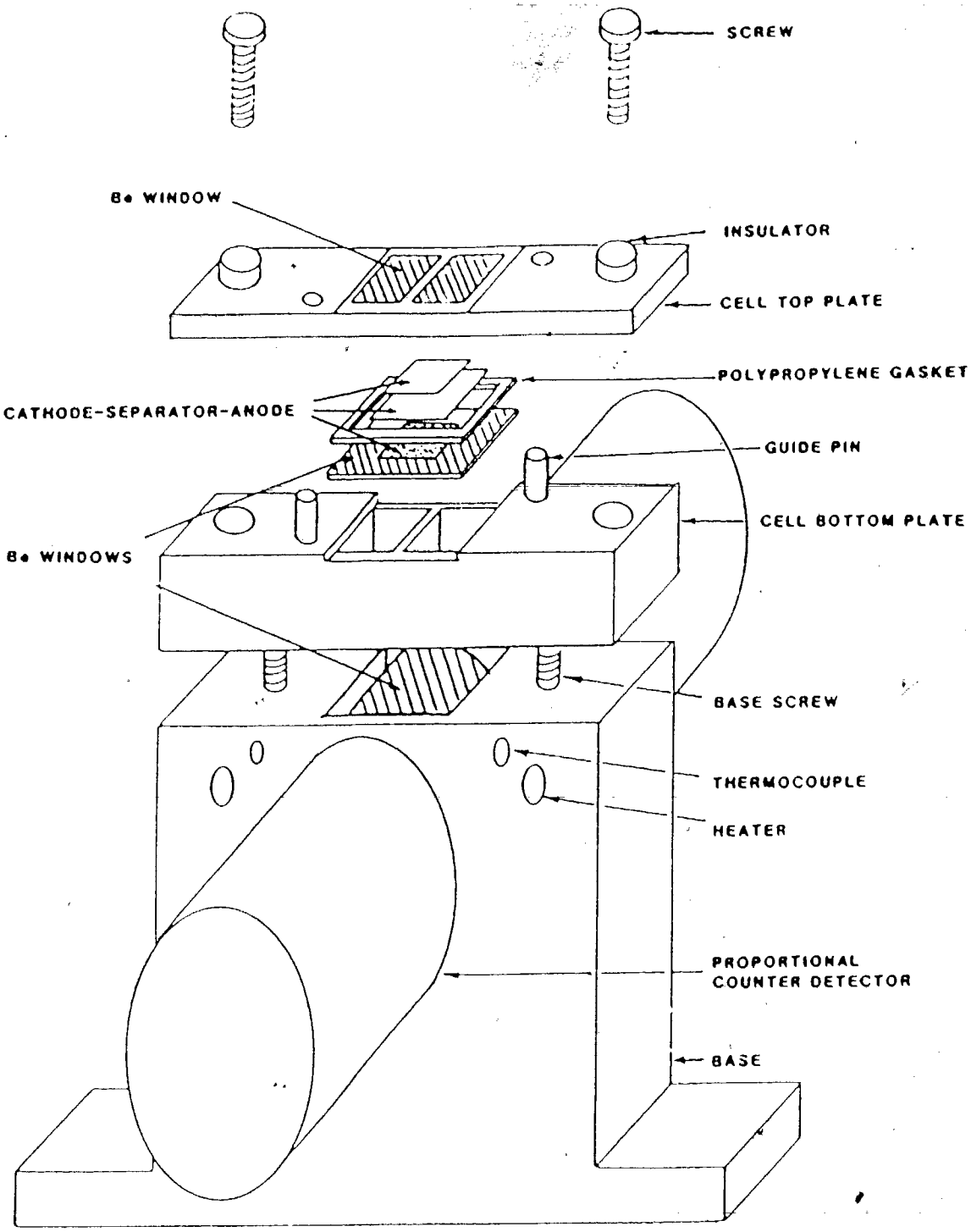

Figure 8: An in-situ Mössbauer cell.

2.2 Synthesis of Materials

There were two methods of preparation of lithiated cathode materials. The first (the more economical method), used lithium naphthalide to chemically synthesize the lithiated phase (11). In the second method, a stoichiometric solid mixture was heated. Since the lithiated materials were air-sensitive, preparations were carried out inside a helium atmosphere glove box.

Lithiated samples were typically prepared in 50 grams samples. The starting minerals, either natural pyrite, chalcopyrite (Teck Mining Corp.) or both, were added to a stirring solution of napthalene (NAPH) (Fisher) in tetrahydrofuran (THF) (Fisher). Upon the addition of lithium metal, a redox reaction with NAPH produced the reduced form of the reagent.

$$(2-x)\ \mathrm{Li} + (2-x)\ \mathrm{NAPH} \xrightarrow{\mathrm{THF}} (2-x)\ \mathrm{Li^+NAPH^-} \qquad (2.2.1)$$

Lithium napthalide then reacted with the starting minerals to give a mixture containing lithium sulfide, metals of the starting minerals (copper and iron), and unreacted starting materials.

$$\begin{aligned}(2-x)\ \mathrm{LiNAPH} + (1-x)\ \mathrm{FeS_2} + x\ \mathrm{CuFeS_2} \longrightarrow \\ \tfrac{1}{2}(2-x)\ \mathrm{Li_2S} + (x-a)\ \mathrm{Cu} + (\tfrac{1}{2}-\tfrac{x}{4})\ \mathrm{Fe} + \\ (\tfrac{1}{2}+\tfrac{x}{4}-a)\ \mathrm{FeS_2} + a\ \mathrm{CuFeS_2} + (2-x)\ \mathrm{NAPH}\end{aligned} \qquad (2.2.2)$$

The solution was left stirring overnight to ensure the reaction proceeded to completion. The resulting material was filtered, then washed three times with THF, and pumped to dryness to remove all the residual organic material. Finally, the lithiated powder was placed in a graphite tube within a quartz tube. A steady flow of argon was maintained in the quartz tube as the sample was slowly heated to 800°C for 16 hours. The reaction which took place during the heating process was the formation of the appropriate lithiated compound.

$$\begin{aligned}\frac{1}{2}(2-x)\ \mathrm{Li_2S} + (x-a)\ \mathrm{Cu} + (\frac{1}{2}-\frac{x}{4})\ \mathrm{Fe} + \\ (\tfrac{1}{2}+\tfrac{x}{4}-a)\ \mathrm{FeS_2} + a\ \mathrm{CuFeS_2} \xrightarrow{heat} \mathrm{Li_{2-x}Cu_xFeS_2}\end{aligned} \qquad (2.2.3)$$

Since the mole ratio of Cu : FeS_2 : $CuFeS_2$ in the reaction mixture was not determined the quantity of a remained unknown. But typical values for x (ie. the amount of copper substitution) ranged between 0 to 1, and the values of a were, therefore, limited from 0 to x.

The second method was primarily used for the preparation of single crystals of the lithiated materials. The procedure involved mixing together Li_2S (Alfa, 99%), Fe (Spex, 99.9%), Cu (Alfa, 99%), natural FeS_2, and natural $CuFeS_2$ in the correct stoichiometry. The powders were mixed and heated under the same conditions described above. For the preparation of Li_2FeS_2, the sample was heated to 900°C , fifteen degrees above the reported melting point (4). For $LiCuFeS_2$, the heating was only taken to 800°C. The samples were cooled to room temperature over a period of 8 hours so that sizeable single crystals (0.2 to 0.5 mm) were obtained. Since this procedure involved only a solid state reaction, it was possible to determine accurately the weight loss of the sample due to heating in an unsealed system. This was important for the preparation of samples for crystallographic work.

2.3 Deintercalation of Lithium

Lithium can be removed from a lithium intercalation compound either chemically or electrochemically. In a battery, this corresponds to the charging half-cell reaction, which can be described by equation 1.1.2 proceeding to the left. Chemically, it is equivalent to the oxidation of the lithiated compound, whose reduction potential relative to Li/Li^+ is greater than that of the host. A particularly useful reagent, developed by Murphy et al. (11) is iodine in acetonitrile (AN). It was reported that the reduction of iodine to the colourless iodide ion indicated a voltage of approximately 2.8 volts. Thus, this is a useful technique to synthesize the reaction products of a fully charged electrochemical cell.

Finely ground lithiated compound was allowed to react in a stirring solution of iodine (Fisher) in acetonitrile (Fisher) for 16 hours. The reaction involved was the formation of lithium iodide which was soluble in AN.

$$Li_xMX_2 + \ n\ I_2 \longrightarrow x\ LiI\ +\ "MX_2"\ +\ (n - \frac{x}{2})\ I_2 \qquad (2.3.1)$$

The reaction product, $"MX_2"$, may be formed as a compound, or may disproportionate to MX and X. Typically twice the required amount of iodine was used to make a 0.2 M solution with AN. The resulting material was washed with AN, filtered, and dried as previously described.

For the preparation of single crystals of a partially delithiated compound, the above procedure was modified. Instead of grinding the lithiated compound to a fine powder, small chunks were put into a bottle containing AN. Iodine was added in small quantities up to approximately 20% of the amount required for complete delithiation. The reaction was allowed to proceed undisturbed until the solution turned clear. Typically, this took two to three weeks.

2.4 Summary of Samples Synthesized

Table I is a summary of all the samples which have been mentioned in this thesis. It should be noted that the pyrite and chalcopyrite used in these syntheses came from mines located in different parts of the world. They were labelled "spanish pyrite", "UBC chalcopyrite", "Teck pyrite", and "Teck chalcopyrite". These minerals came in the form of large crystals which were hand-picked from the mines. Upon receiving, they were ground to a powder of less than 45 μm in size. Metal analysis (by Can test Ltd.) using an Inductively Coupled Argon Plasma Spectrograph (ICAP) showed that Teck pyrite and Teck chalcopyrite have a consistently lower level of elemental impurities. Table II gives a summary of the reported values. Hence, all the results reported in this thesis are from samples prepared using the minerals from Teck Mining Corporation.

TABLE I - A summary of the synthesized compounds mentioned in the thesis.

Name	Stoich-iometry	Reaction Method/ Temperature	Product(s)	Comments
A	Li_2FeS_2	NAPH;600°C	Li_2FeS_2	spanish FeS_2 broad peaks
B	Li_2FeS_2	NAPH;800°C	Li_2FeS_2	spanish FeS_2
C	$LiFeS_2$	NAPH;600°C	Li_2FeS_2 + FeS + ...	spanish FeS_2
D	$LiFeS_2$	NAPH;800°C	Li_2FeS_2 + FeS +...	spanish FeS_2
E	Li_3FeS_2	NAPH;800°C	Li_2S + Fe + FeS	spanish FeS_2
F	$Li_{\frac{1}{3}}FeS_2$	NAPH;600°C	Li_2FeS_2 + FeS + ...	spanish FeS_2 broad peaks
G	$Li_{\frac{1}{3}}FeS_2$	NAPH;800°C	Li_2FeS_2 + FeS + ...	spanish FeS_2
H	Li_2FeS_2	NAPH; 200°C 300°C, 400°C 500°C, 800°C	Li_2S + FeS Li_2FeS_2	TECK FeS_2
I	Li_2FeS_2	NAPH; 900°C	Li_2FeS_2	TECK FeS_2; crystal det. of $LiFe_{1.5}S_2$
J	Li_2FeS_2	Li_2S+ Fe+FeS_2 900°C	Li_2FeS_2	TECK FeS_2; crystal det. of Li_2FeS_2

TABLE I (cont'd)- A summary of the synthesized compounds mentioned in the thesis.

Name	Stoich-iometry	Reaction Method/ Temperature	Product(s)	Comments
K	delithiated Li_2FeS_2	I_2/AN; room temp	FeS + S + $Li_{2-x}FeS_2$	delithiation of J; 20 hours of stirring
L	$Li_{\frac{1}{3}}Cu_{\frac{2}{3}}FeS_2$	NAPH; 800°C	$Li_{\frac{1}{3}}Cu_{\frac{2}{3}}FeS_2$	TECK FeS_2 and
M	$Li_{\frac{1}{4}}Cu_{\frac{1}{4}}FeS_2$	NAPH; 800°C	$Li_{\frac{1}{4}}Cu_{\frac{1}{4}}FeS_2$	TECK FeS_2 and $CuFeS_2$
N	$LiCuFeS_2$	NAPH; 800°C	$LiCuFeS_2$	TECK FeS_2 and $CuFeS_2$
O	delithiated $Li_{\frac{1}{3}}Cu_{\frac{2}{3}}FeS_2$	I_2/AN; room temp	metastable $Cu_{\frac{2}{3}}FeS_2$	delithiation of L; 20 hours of stirring
P	delithiated $Li_{\frac{1}{4}}Cu_{\frac{1}{4}}FeS_2$	I_2/AN; room temp	metastable $Cu_{\frac{1}{4}}FeS_2$	delithiation of M; 40 hours of stirring
Q	delithiated $LiCuFeS_2$	I_2/AN; room temp	metastable $CuFeS_2$	delithiation of N; 40 hours of stirring
R	$LiCuFeS_2$	$Li_2S + FeS_2 +$ Cu + Fe; 800°C	$LiCuFeS_2$	TECK FeS_2; crystal det. of $LiCuFeS_2$
S	partially delithiated $Li_{1-\delta}CuFeS_2$	I_2/AN; room temp	metastable $CuFeS_2$	delithiation of R; crystal det. of $Li_{1-\delta}CuFeS_2$
T	FeS	Fe + S; 450°C	$FeS_{1.064}$	non-stoichiometric FeS_y, where $y_{avg} = 1.064$

Table II - Impurities detected in pyrite and chalcopyrite from different sources. Method of analysis is by Inductively Coupled Argon Plasma (by Can test Ltd).

Impurities	Spanish Pyrite (ppm)	TECK Pyrite (ppm)	UBC Chalcopyrite (ppm)	TECK Chalcopyrite (ppm)
Al	240	265	< 30	740
Ca	400	150	3300	450
Co	21	22	290	10
Cu	460	1820	*	*
Mg	120	40	380	160
Mn	60	10	280	8
Ni	20	10	580	16
Pb	600	53	50	<30
Zn	280	57	400	4

* - Copper is not an impurity in chalcopyrite.

3 EXPERIMENTAL TECHNIQUES

3.1 Powder X-ray Diffraction

Powder diffraction is a standard technique which is used to identify unknown substances. Its theory is well-known (12) and, therefore, will not be discussed here. However, the limitations associated with this technique will be considered carefully.

The diffractometer used was equipped with a copper tube and a vertical goniometer, which was modified to accomodate the sample holder (10). The motor control was capable of determining 2θ values to an accuracy of 0.01°.

Samples were prepared in flat plate form by using the same air-tight holders that were described for the in-situ X-ray diffraction experiments. The surface of the sample, when mounted on the goniometer, must make equal angles with the incident and and diffracted beams. In this geometry, the absorption factor becomes independent of theta provided that the sample exceeds a minimum thickness (12). For a typical absorption coefficient of 550cm^{-1} in CuK_{α} and a maximum theta value of 35°, the minimum required thickness of the sample is 0.0036 cm.

The variations in thickness from sample to sample can lead to a systematic shift in 2θ. This effect results from a displacement of the surface of the sample from the goniometer axis of rotation and ultimately affects the determination of the dimensions of the unit cell (10). Therefore, a correction to the peak positions was included in the least squares refinements for determining the lattice constants (10).

Finally, preferred orientation exhibited by layered structures is the biggest limitation associated with sample preparation of this type. For layered structures, the tendency of the platelets to lie flat enhances the basal $(00l)$ reflections with respect to the $(hk0)$ reflections. This effectively alters the relative intensities of the diffraction peaks and results in incorrect placements of the atoms in the unit cell.

3.2 Electrochemical Measurements

The variation of the $V(x)$ curve is related to the thermodynamics of the components of the cell. To extract thermodynamic information about the intercalation system, it is helpful to draw an analogy between the $V(x)$ curve of an intercalation cell and an isotherm of a gas.

3.2.1 Thermodynamics of a Gas

Let the equation of state for a substance of volume v, pressure p, and temperature T to be

$$p = p(v, T) \tag{3.2.1}$$

for the range of variables where the substance is a gas or a liquid. The equation of state 3.2.1, represented by a set of of $p(v)$ curves for various temperature, is shown schematically in figure 9. Each curve of constant temperature is an isotherm.

For the isotherm illustrated in figure 10, at $p < p_1$, the curve yields a unique value of v, and a positive value for the isothermal compressibility, k, where k is defined to be

$$k = -\frac{1}{v}\left(\frac{\partial v}{\partial p}\right)\Bigg|_{T.} \tag{3.2.2}$$

When $k \geq 0$, or when the slope of the curve $\frac{\partial p}{\partial v} \leq 0$, stability conditions are satisfied. Hence, in this region, a well-defined single phase with a relatively large compressibility, such as that for a gaseous phase, exists. At $p > p_2$, the stability condition is again satisfied. But since the compressibility of this phase is relatively small, the single phase which exists is liquid. At the intermediate pressure range $p_1 < p < p_2$, there are three possible values of volume v for each pressure p. But the portion of the curve labelled JDN violates the stability condition, therefore, values of v in this range are not possible as they lead to an intrinsically unstable situation. This leaves two possible values of v, v_A and v_B. To consider the relative stability of v_A and

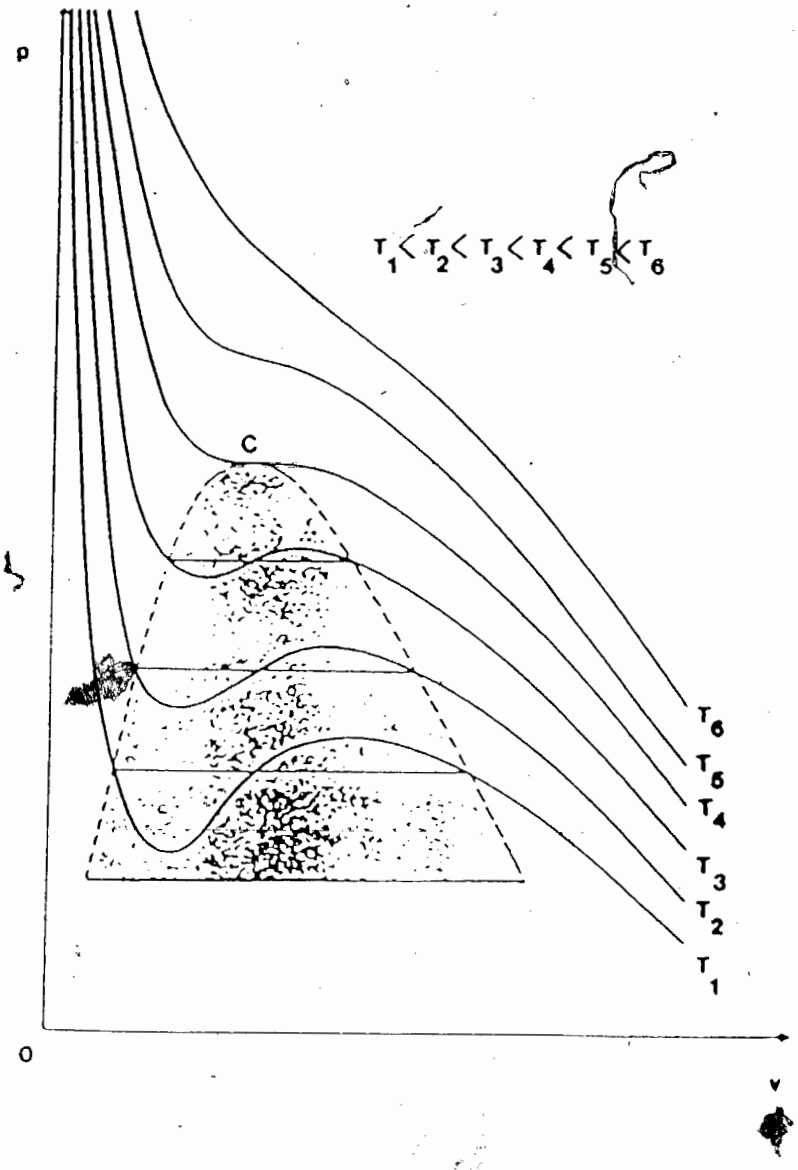

Figure 9: Schematic diagram describing an equation of state 3.2.1 for various temperatures. The point C is the critical point. The shaded region is the area where two phases can coexist along the horizontal lines.

v_B, the relative magnitude of partial molar Gibbs free energies, $g_A(p,T)$ and $g_B(p,T)$, must be considered.

The function $g(p,T)$ is defined to be

$$g = \epsilon - Ts + pv \tag{3.2.3}$$

where ϵ is the molar energy, and s is the entropy. For infinitesimal changes in pressure and temperature

$$dg = -sdT + vdp \tag{3.2.4}$$

At constant T,

$$g - g_o = \int_{p_\delta}^{p} vdp \tag{3.2.5}$$

By performing the integral in equation 3.2.5 on the isotherm in figure 10, a curve of $g(p,T)$ versus p, as shown in figure 11, is obtained. When $p < p_X$, the substance behaves as a gas. At pressures $p > p_X$, it behaves as a liquid. At point X, the system shifts from the gas phase to the liquid phase. Thus, p_X corresponds to the pressure where the phase transition occurs, and that both phases coexist in equilibrium with each other in arbitrary proportions.

The pressure of the phase transformation p_X corresponds to $p = p_A$ in figure 11. The horizontal line ADB, which joins points A and B at p_A, is characterized by the fact that

$$g_A = g_B \tag{3.2.6}$$

It is along this line which phase transformation occurs. From equation 3.2.2, phase transitions are signaled by the divergences of the compressibility of the substance.

During the course of the phase transformation the total molar volume, v_{tot}, is given by

$$v_{tot} = \xi v_B + (1 - \xi)v_A \tag{3.2.7}$$

where v_B is the molar volume of the gas, v_A is that of the liquid, and ξ is the fraction of the total molar volume in the gas phase.

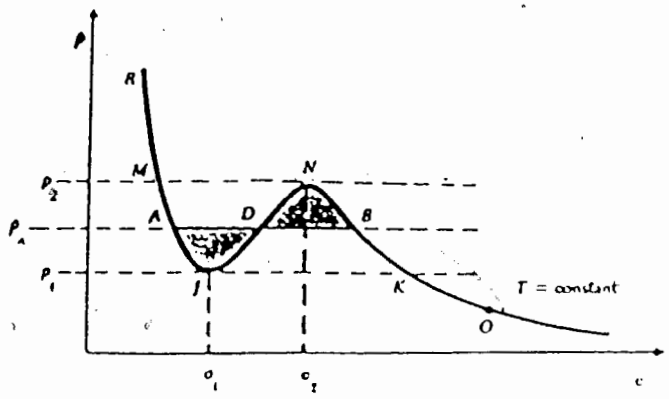

Figure 10: An isotherm for an equation of state 3.2.1.

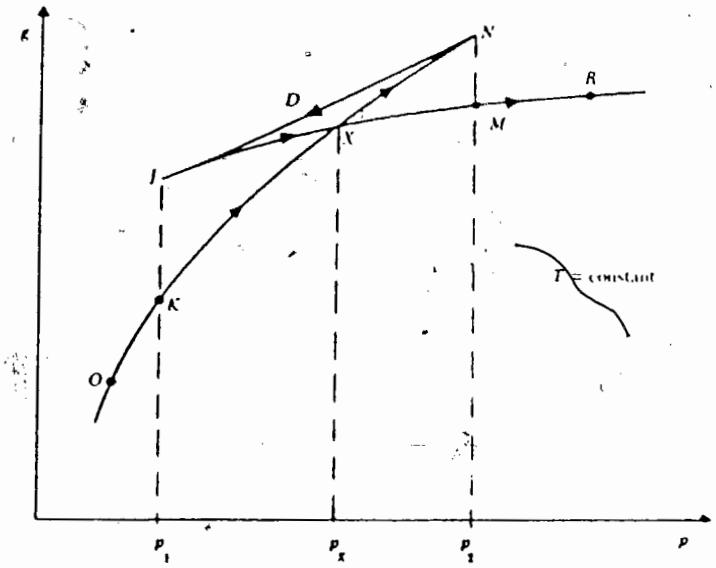

Figure 11: The behaviour of $g(p)$ at constant temperature implied by the curve of 10.

3.2.2 Thermodynamics of an Intercalation Battery

As shown in equation 1.1.4, the voltage of an intercalation battery can be related to Gibbs free energy, G, where

$$G(p,T) = \sum_{i=1} \nu_i g_i(p,T) \tag{3.2.8}$$

ν_i is the number of moles of phase i present. Like $g(p,T)$, the function $G(p,T)$ is defined to be

$$G = E - TS + pv \tag{3.2.9}$$

where S is the entropy, and E is the internal energy.

In an intercalation battery, the number of lithium atoms in the cathode, n, can vary. This quantity is usually referenced to the number of metal atoms in the cathode, N, such that

$$n = xN \tag{3.2.10}$$

Therefore, the fundamental relation, dE, is of the general form

$$dE = TdS - pdv + \mu dn \tag{3.2.11}$$

In the battery, where the pressure is constant, the change in free energy, dG, is given by

$$dG = -SdT + \mu dn \tag{3.2.12}$$

Thus, the Maxwell relation,

$$\left.\frac{\partial \mu}{\partial T}\right|_n = -\left.\frac{\partial S}{\partial n}\right|_T \tag{3.2.13}$$

can be derived.

Equations 3.2.4 and 3.2.12 are identical if the substitutions v to n and p to $-\mu$ are made. Thus, the thermodynamics of a gas is analogous to the thermodynamics of the intercalation battery. Following the analogy,

the equation of state of an intercalation battery, $\mu = \mu(n, T)$, which can be related to the electromotive force, V, by equations 1.1.5 and 3.2.10 is

$$V = V(x, T) \tag{3.2.14}$$

The isothermal compressibility, as defined in equation 3.2.2, has the analogous form of

$$-\frac{1}{n}\frac{\partial n}{\partial \mu}\bigg|_T = \frac{1}{ex}\frac{\partial x}{\partial V}\bigg|_T \tag{3.2.15}$$

for the intercalation battery. Divergences, or peaks (when kinetic effects are included) signal first order phase transitions. The fraction ζ of the cathode in phase 1 and the fraction $(1 - \zeta)$ in phase 2, are determined by

$$x = \zeta x_1 + (1 - \zeta)x_2 \tag{3.2.16}$$

where x_1 and x_2 are the compositions in the two coexisting phases. Table III summarizes the analogies between thermodynamics of the intercalation battery and the gas.

TABLE III - Analogy between thermodynamics of the intercalation battery and the gas

Thermodynamic Quantity	Intercalation † Battery	Gas †
Equation of State	$V = V(x,T)$	$p = p(v,T)$
Free Energy	$G = G(n,T)$ $dG = -SdT + \mu dn$	$g = g(p,T)$ $dg = -sdT + vdp$
Compressibility	$-\frac{1}{n}\frac{\partial n}{\partial \mu}\Big\|_T = \frac{1}{ex}\frac{\partial x}{\partial V}\Big\|_T$	$k = -\frac{1}{v}\left(\frac{\partial v}{\partial p}\right)\Big\|_T$
Maxwell relation	$\frac{\partial \mu}{\partial T}\Big\|_n = -\frac{\partial S}{\partial n}\Big\|_T$	$\frac{\partial P}{\partial T}\Big\|_v = \frac{\partial S}{\partial v}\Big\|_T$

† - the thermodynamics of a gas is identical to the thermodynamics of the intercalation battery when the substitutions v to n, and p to $-\mu$ are made.

3.2.3 Phase Transitions in an Intercalation Battery

When a cell based on intercalation is charged or discharged at constant current, the rate of change of cell voltage with time is

$$\frac{dV}{dt} = \frac{dV}{dx}\frac{dx}{dQ}\frac{dQ}{dt} \tag{3.2.17}$$

where V is the cell voltage, Q is the charge, and t is the time. $\frac{dQ}{dt}$ is the current, I, and $\frac{dQ}{dx}$ is defined to be Q_o, the charge which flowed to change x by 1. Therefore,

$$\frac{dx}{dV} = \frac{I}{Q_o}\frac{dt}{dV}. \tag{3.2.18}$$

This states that $\frac{dt}{dV}$ is proportional to the thermodynamic quantity $\frac{dx}{dV}$. Hence, by measuring the $V(t)$ curve at constant current, $\frac{dx}{dV}$ is inversely proportional to the slope of $V(x)$. This method of measuring $\frac{dx}{dV}$ is called derivative constant current chronopotentiometry (13).

The equation of state 3.2.14 for an intercalation battery is shown schematically in figure 12(a). The corresponding "G vs. x" curve, as shown in (b), is obtained by

$$G - G_o = -\int_{x_o}^{x} V dx \tag{3.2.19}$$

These curves are analogous to those shown in figures 10 and 11 for the gas. Following the analogy, at composition $x < x_1$, phase 1 exists. At composition $x > x_2$, phase 2 exists. In the intermediate range, $x_1 < x < x_2$, a phase transition occurs and phase 1 and 2 coexist. The dashed line, which joins x_1 and x_2, is determined by drawing a common tangent to the lowest free energy of composition x_1 and x_2. It represents the free energy of the two coexisting phases.

For an ideal cell during a phase transition, the surface concentration of lithium remains fixed while the phase boundary moves through the crystal. This means that μ_c is constant, and, from equation 1.1.5, the voltage in a two-phase region is also constant. Thus, a plateau in the $V(x)$ curve

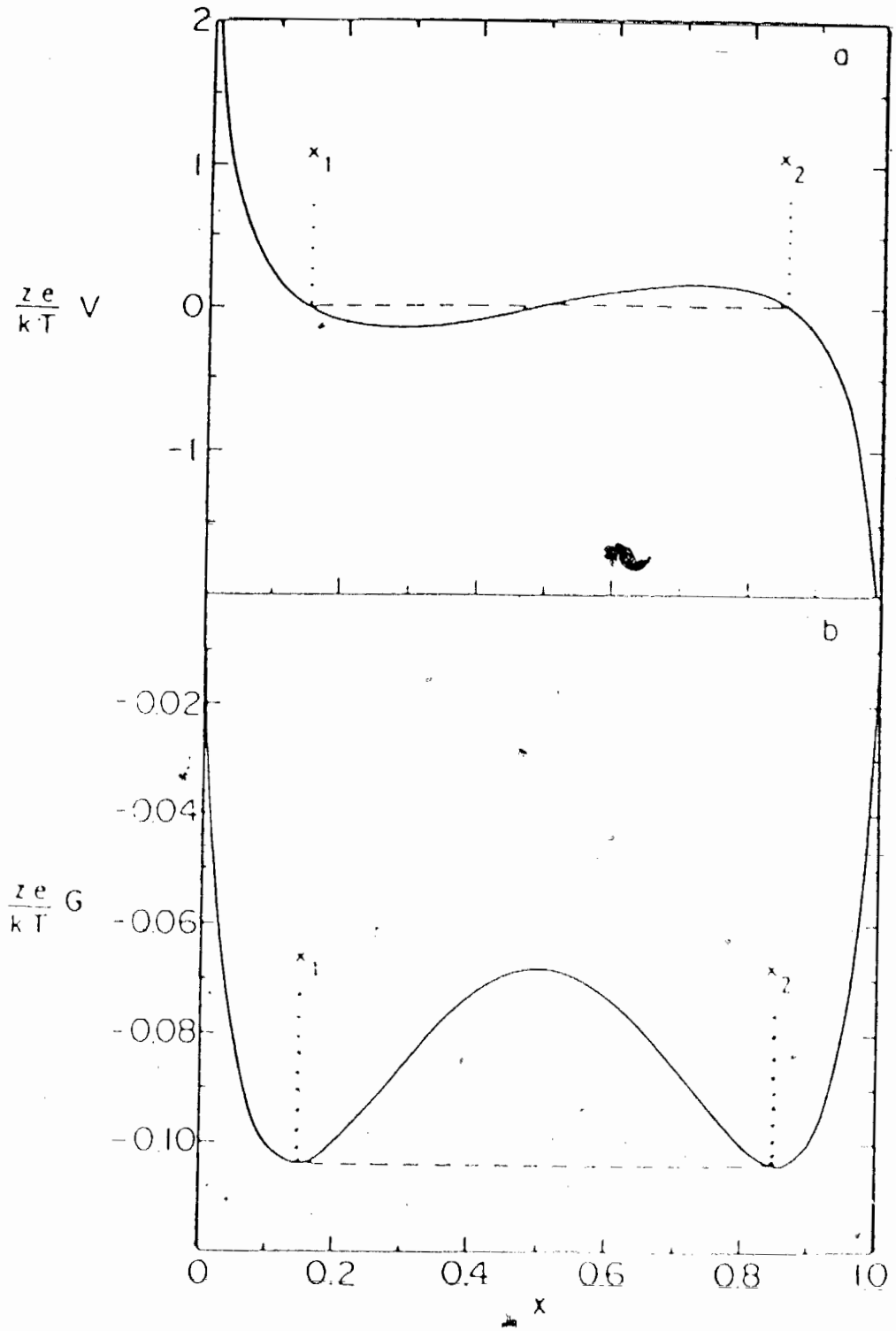

Figure 12: (a) A $V(x)$ curve. (b) The behaviour of $G(x)$ at constant temperature implied by the curve shown in (a).

generally signals a first order phase transition. Since $dV = 0$, according to 3.2.18, a divergence in $\frac{dx}{dV}$ at the transition voltage is observed. In practice, the cell voltage, as measured across the terminals, is not equal to the equilibrium voltage at the surface of the cathode. This difference in voltage is due to various over-voltages and internal impedances. Their effects usually result in distortions of $\frac{dx}{dV}$ from the ideal delta functions into peaks of finite width and area (14). These peaks, as observed in "$\frac{dx}{dV}$ vs. V" plots in figure 30, are unambiguous signals of first order phase transitions.

In summary, in single phase regions of a binary system, the voltage of the cell V varies with x, whereas, in two phase regions of a binary system, V remains constant, independent of x. Similarly, for a '$n - ary$' system, in $[1, 2, ..., (n-1)]$ phase regions, V must vary with x. But in 'n' phase regions V must remain constant, independent of x.

3.2.4 The Constant Current Method

To determine the coarse features of the voltage curve, $V(x)$, electrochemical test cells were charged and discharged at constant current between fixed voltage limits. The cyclers used in these experiments were capable of maintaining a stable current to within $\pm 2\%$. From the mass of the cathode in the cell, x is

$$x = \frac{\mathrm{I}t\mathrm{M}}{m\mathrm{F}} \tag{3.2.20}$$

where I is the current, t is the duration of current flow (sec), M is the molecular weight of the cathode, m is the cathode mass and F is Faraday's constant.

Equation 3.2.20 assumes that the net charge transfer is due totally to the intercalation of lithium into the cathode. In practice, there are two factors which affect the value of x and they must be considered. The first is the "side reactions" as described in section (2.1). The second is "cathode utilization". This problem arises when the entire cathode mass is not electrically connected to the aluminum substrate.

3.2.5 The Constant Voltage Method

The constant voltage technique involved incrementing (or decrementing) the cell voltage and measuring the charge which flowed until the cell reached equilibrium. In-situ X-ray and Mössbauer cells were charged and discharged in this manner so that the lithium content of the cathode could be controlled. This method was used in conjunction with derivative constant current chronopotentiometry (13) to study phase transitions in the lithium intercalation batteries.

Examination of $\frac{dx}{dV}$ plotted against V reveals fine features in the $V(x)$ curves. From these graphs, the stepping voltages are determined. Cells which are charged and discharged by constant voltage are usually stepped beyond a peak to a voltage where $\frac{dx}{dV}$ is minimum. This corresponds to taking the cell across a plateau on the $V(x)$ curve, to the end of the phase transition.

The equipment which is used to step the voltage of a cell is a potentiostat equipped with a digital coulometer. The cell is connected to a series resistor to limit the current flow to less than 200 μamps. Once the current flow through the cell is less than 5 μamps, the cathode is considered to be in equilibrium. X-ray and Mössbauer spectra measured at this point can yield useful information about the phase transition.

3.3 Single Crystal X-ray Diffraction

The literature contains incorrect speculations on the structures of Li_2FeS_2 and $Li_{\frac{1}{3}}Cu_{\frac{2}{3}}FeS_2$ based on techniques such as powder X-ray diffraction (3, 4, 5, 6, 15), Mössbauer spectroscopy (5), and Infrared Spectroscopy (16). Using single crystal X-ray diffraction, the structures of Li_2FeS_2, $Li_2Fe_3S_4$, $LiCuFeS_2$, and $Li_{1-\delta}CuFeS_2$ were determined. Diffraction data were collected on an Enraf-Nonius CAD-4F equipped with a molybdenum tube and a graphite monochromator. Cell dimensions were determined by least-squares refinement of at least 20 accurately centered reflections ($2\theta > 30^o$). Background counts were taken by extending measurements on each side of the scan by 25% of the predetermined scan angle. Intensity measurement of two standards every hour or less showed no evidence of crystal deterioration during data collection.

Computations were performed with complex scattering factors for neutral atoms (17) using programs from the NRC-VAX Crystal Structure System (18). Detailed discussions of the final atomic coordinates, occupancies, and thermal parameters, U, of the individual structures will be given in chapter 4.

3.3.1 Data Acquisition Procedures

Using the unit cells obtained from powder X-ray diffraction, the possible Laue symmetry for these structures are: $\bar{3}$, $\bar{3}m$, $6/m$, $6/mmm$. By analysis of the intensities of the symmetry equivalent reflections (hkl, $hk\bar{l}$, khl, and $kh\bar{l}$), the Laue symmetry of the reciprocal lattice was determined to be $\bar{3}m$ symmetry with no systematic conditions. This led to the six possible space groups: $P31m$, $P3m1$, $P\bar{3}1m$, $P\bar{3}m1$, $P321$, and $P312$.

Table IV summarizes the crystal data acquisition and refinement parameters. Only reflections with intensities greater than 2.5 σ were used in the structure refinement. Intensity scaling, Lorentz, polarization, and absorption corrections were applied to the raw data. Models for the structures were derived by solving the Patterson map. Full matrix, least squares refinement, which minimized $w(|F_o| - |F_c|)^2$ (where w is the weight assigned to an observed reflection, F_o and F_c are observed and calculated structure factors) in the space group $P\bar{3}m1$ yielded acceptable final residual R-values. A weighting scheme, which kept $w(|F_o| - |F_c|)^2$ near constant as a function of $|F_o|$, $\frac{\sin\theta}{\lambda}$, and the Miller indices, h, k, and l, was applied. Finally, refinement was terminated when the shifts in parameters at the end of each least squares cycle over the associated errors dropped to less than 1%.

The final difference map of these structures displays several maxima and minima occurring near the Fe and S. These features are attributed to the error associated with the termination of the Fourier series.

Table IVa - Crystal data acquisition and refinement parameters of $LiFe_{1.5}S_2$ and Li_2FeS_2

COMPOUND	$LiFe_{1.5}S_2$	Li_2FeS_2
Space Group	$P\bar{3}m1$	$P\bar{3}m1$
$a(\AA)$	3.851(2)	3.902(1)
$c(\AA)$	6.305(3)	6.294(2)
$U(\AA^3)$	81.0	83.0
$\mu_{MoK\alpha}(cm^{-1})$	77.5	54.6
$\rho(g/cm^3)$	3.18	2.68
Z	1	1
FW (g/mole)	154.83	133.85
Measurement Temperature (° C)	23	23
Crystal Dimensions (mm)	0.65 ×0.59 × 0.38	0.32 × 0.23 × 0.15
Transmission Coefficient	0.0689 to 0.20160	0.3875 to 0.5519
Scan mode	$\theta - 2\theta$	$\theta - 2\theta$
Scan width (deg)	$1.1 + 0.35\ \tan\theta$	$1.1 + 0.35\ \tan\theta$
Scan speeds(°/min)	0.92 to 5.49	0.97 to 5.49
$2\theta_{max}$(deg)	90	90
Number of Reflections	364 [316 ($\geq 2.5\sigma$)]	373 [283 ($\geq 2.5\sigma$)]
Refined Variables	8	9
R_f †	0.039	0.043
R_{wf} ††	0.054	0.066
$G.O.F.$ ‡	1.807	1.721
k, Instrument Error ‡‡	0.0006	0.0010

† $R_f = \frac{\sum(|F_o|-|F_c|)}{\sum|F_o|}$; for observed data ($I \geq 2.5\sigma(I)$)

†† $R_{wf} = \sqrt{\frac{\sum(w(|F_o|-|F_c|)^2)}{\sum wF_o^2}}$; for observed data ($I \geq 2.5\sigma(I)$)

‡ Goodness of Fit, $G.O.F. = \frac{\sum(w(|F_o|-|F_c|)^2)}{degrees\ of\ freedom}$

‡‡ $w = |\sigma^2(F) + kF^2|^{-1}$

Table IVb - Crystal data acquisition and refinement parameters of $LiCuFeS_2$ and $Li_{1-\delta}CuFeS_2$

COMPOUND	$LiCuFeS_2$	$Li_{1-\delta}CuFeS_2$
Space Group	$P\bar{3}m1$	$P\bar{3}m1$
$a(\AA)$	3.807(2)	3.77(4)
$c(\AA)$	6.352(1)	6.27(10)
$U(\AA^3)$	79.7	77.2
$\mu_{MoK\alpha}(cm^{-1})$	122.1	126.0
$\rho(g/cm^3)$	3.97	4.05
Z	1	1
FW (g/mole)	190.45	184.20
Measurement Temperature (°C)	23	23
Crystal Dimensions (mm)	0.18 × 0.15 × 0.15	0.31 × 0.24 × 0.24
Transmission Coefficient	0.0486 to 0.1552	0.0986 to 0.2109
Scan mode	$\theta - 2\theta$	$\theta - 2\theta$
Scan width (deg)	$1.1 + 0.35\ \tan\theta$	$2.9 + 0.35\ \tan\theta$
Scan speeds(°/min)	0.96 to 5.49	2.75
$2\theta_{max}$(deg)	100	60
Number of Reflections	363 [305 ($\geq 2.5\sigma$)]	109 [109 ($\geq 2.5\sigma$)]
Refined Variables	9	14
R_f †	0.033	0.044
R_{wf} ††	0.043	0.055
$G.O.F.$ ‡	2.014	1.825
k, Instrument Error ‡‡	0.0002	0.0008

†, ††, ‡, ‡‡ – see Table IVa.

3.4 ^{57}Fe Mössbauer Spectroscopy

In principle gamma-radiation, emitted in the de-excitation of a radioactive nucleus should be able to excite another nucleus of the same isotope to give rise to nuclear resonance absorption and fluorescence. However during emission, by conservation of momentum, part of the excitation energy of the nucleus is lost as recoil kinetic energy, E_r, and hence the gamma-ray emitted has an energy $(E_t - E_r)$, where E_t is the nuclear energy level separation. Similarly, for resonance absorption, the required photon energy is $(E_t + E_r)$. As shown in figure 13, the thermal motion of the emitting and absorbing atoms may broaden the observed linewidth sufficiently that a small fraction of the gamma-radiation does indeed undergo nuclear resonance fluorescence.

Mössbauer discovered that when the nucleus is solidly bound in a crystal lattice, emission or absorption of the gamma- ray occurs without nuclear recoil or thermal broadening. Thus, for solids, the observed resonance absorption lines, which are now characterized by the natural linewidth of the gamma- radiation, are usually very sharp. This phenomenon is known as the Mössbauer effect. To observe such an effect with ^{57}Fe nuclei, ^{57}Co is used as radiation source. This isotope undergoes electron capture to give metastable ^{57}Fe ($t_{1/2} = 1.0 \times 10^{-7}$ sec) which decays rapidly to the ground state by emitting gamma-rays. The energy of the gamma-ray monitored is 14.4 KeV. From Heisenberg's uncertainty principle, the natural linewidth of this transition is 4.8×10^{-9} eV. It is this unique production of monochromatic electromagnetic radiation of such a precise energy that gives the technique the capability of resolving minute changes in nuclear energy levels resulting from changes in the atomic environment of the Fe atoms in the sample.

When the 14.4 KeV gamma-ray impinges on the iron-containing absorber, atoms which have the same chemical environment as the source will undergo resonance absorption. But if the atoms in the absorber have a different electronic environment, the energy levels of the iron nuclei of the absorber are shifted. Hence, the energy required for excitation is slightly different than that of the gamma-ray emitted by the radiation source. Typ-

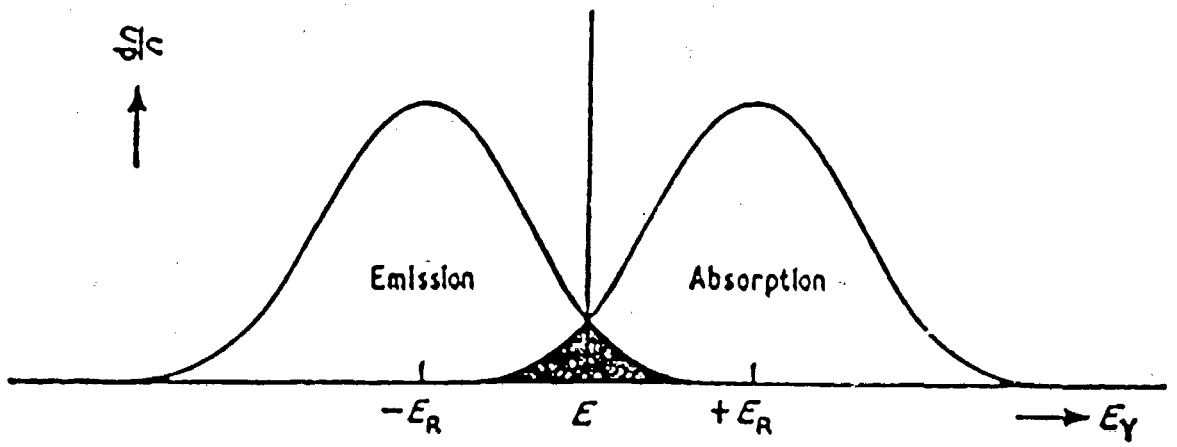

Figure 13: The resonance overlap for free-atoms. Nuclear gamma resonance is the small area shaded in black.

ical changes to the nuclear energy levels are of the order of 10^{-8} eV. In order to investigate such perturbations of the energy levels of the iron nuclei in the absorber, the gamma-ray energy must be modified. This can be achieved by moving the radiation source towards and away from the absorber at velocities of the order of 0.2 mm/s.

The source is mounted on an electromechanical transducer and is driven back and forth at constant acceleration to scan a range of velocities (typically from -8 to 8 mm/s). The experiment is set up in the transmission mode where the gamma-rays emitted by the source pass through the absorber and enter a proportional counter. Thus, the occurrence of resonance absorption is recognized by a decrease in intensity of the radiation. The data is accumulated in a multi-channel analyzer in the multi-scalar mode and a constant increment of velocity can be derived for each channel. The spectrum recorded is a plot of gamma-ray counts at the detector, or relative transmission, against the velocity of the source with respect to the absorber.

A Mössbauer spectrum is characterized by the number, shape, positions, and relative intensities of the absorption lines. These features result from various hyperfine interactions between the nucleus and its surrounding electrons. They are the isomer shift (IS), the quadrupole splitting (QS), and the magnetic splitting (19, 20), and their significance will be addressed in section 4. Curve fitting by least squares analysis allows the determination of these observed shifts and splittings. But the final interpretation of the fitted data must have physical meaning, and be compatible with other scientific supporting evidence.

3.5 Differential Scanning Calorimetry

Calorimetric measurements are made using a Perkin-Elmer DSC-4 differential scanning calorimeter (DSC) Samples were pre-weighed and loaded into stainless steel containers with a copper gasket seal. The prepared sample and an empty reference container were placed in a chamber which was continually purged with dry nitrogen gas. The temperatures of the two containers inside the chamber was programmed to change together at a fixed rate. As the temperature increased, exothermic or endothermic reactions resulting from transitions such as melting, decomposition, crystallization or phase changes in the sample material may occur. The DSC detects the temperature difference between the sample and the reference and adjusts the amount of heating power to each accordingly such that the temperature difference is reduced to zero. The output is a plot of the rate of heat flow, $\frac{dH}{dt}$, in joules/sec versus temperature.

Since heat capacity is defined as

$$C_p = \frac{dH}{dT}\bigg|_{p\,=\,const} \tag{3.5.1}$$

it is related to $\frac{dH}{dt}$ by

$$\frac{dH}{dt} = \frac{dH}{dT}\frac{dT}{dt} \tag{3.5.2}$$

where $\frac{dT}{dt}$ is the heating rate. Thus, ordinate displacement is a direct measurement of the heat capacity, and the change in energy associated with a transition is the integral of the peak with respect to time.

$$\Delta H = \int \frac{dH}{dt} dt \tag{3.5.3}$$

In practice, instrument calibration with high purity indium is necessary.

4 RESULTS AND DISCUSSION

4.1 The Li_xFeS_2 $(0 < x \leq 2)$ System

4.1.1 Materials Synthesized

The family of compounds for the Li_xFeS_2 $(0 < x < 2)$ system were synthesized by NAPH/THF reactions and heated at 600°C and 800°C. Table I summarizes the products of the stoichiometric reactions. Under these reaction conditions, the only compound that exists in pure form is Li_2FeS_2. Furthermore, a study of the reaction temperature (sample A) shows that Li_2FeS_2 forms as low as 300°C.

Powder X-ray patterns show that the compound can be described by a hexagonal unit cell with lattice parameters which agree with those previously reported (3, 4, 5). However, a ten-fold superlattice in a, as suggested by Le Mehaute et al. (15), was not observed. The observed intensities of the diffraction peaks do not fit a CdI_2 type structure as proposed by Brec et al. (6). In fact, to account for the observation of the very intense (002) peak, preliminary model calculations require that the iron atoms be tetrahedrally coordinated by sulfur atoms. Thus, in order to clarify the structure of Li_2FeS_2, a single-crystal structure determination was undertaken.

In the first attempt to solve the structure of Li_2FeS_2 (sample I), an alternate structure with the stoichiometry $LiFe_{1.5}S_2$ was discovered. The crystal structure determination of these two compounds, which will be described under sections 4.1.2 and 4.1.3, was done in collaboration with Dr. R. J. Batchelor. Attempts to re-synthesize $LiFe_{1.5}S_2$ were unsuccessful, as will be described in section 4.1.4.

Upon deintercalation of Li_2FeS_2 in a stirring solution of I_2/AN for 20 hours (sample K), a powder mixture of $Li_{2-x}FeS_2$, ferromagnetic pyrrhotite, FeS_y, and sulfur was obtained. The presence of $Li_{2-x}FeS_2$, as will be discussed in section 4.4, was an indication that chemical deintercalation

was incomplete. Since pyrrhotite exists over a range of compositions, a plot of the variation of lattice parameter c versus y (21), as shown in figure 14, allows a determination of y. From the observed lattice parameters ($a = 3.482(2)$Å, and $c = 5.83(1)$Å), the composition of pyrrhotite in the mixture is $FeS_{1.025}$. The thermal properties of this mixture will be discussed in section 4.4.1.

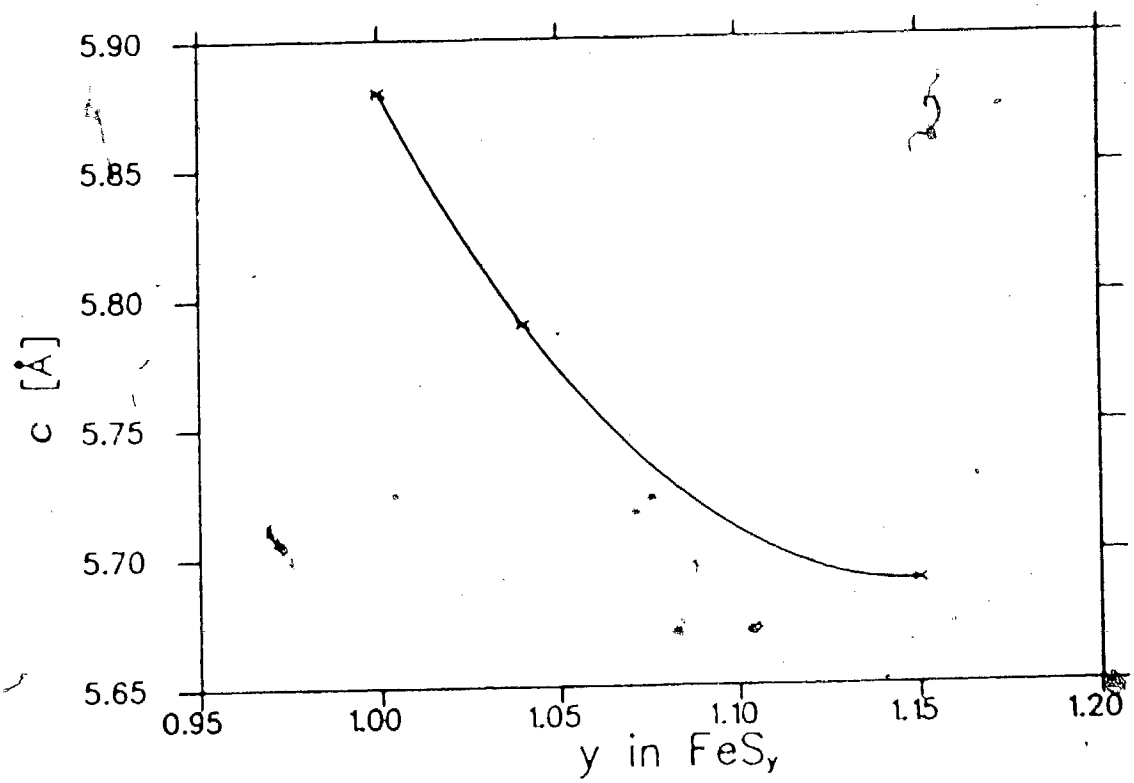

Figure 14: Variation of the lattice parameter c with y in FeS_y.

4.1.2 Crystal Structure of Li_2FeS_2

The crystal structure of Li_2FeS_2 (sample J) has been determined (22). The compound has space group $P\bar{3}m1$ with $a = 3.902(1)$Å, $c = 6.294(2)$Å, and one molecular formula per unit cell. The structure consists of hexagonally close-packed layers of sulfur in the same arrangement as the iodine atoms in the CdI_2 structure. Iron and lithium atoms fill all the tetrahedral interstices equally and randomly between an adjacent pair of sulfur layers (layer 1). The remaining lithium atoms fill the octahedral sites between the other pair of sulfur layers in the unit cell (layer 2). Figure 15a shows a schematic of the layered structure, and a projection in the (110) plane. This arrangement of atoms within the sulfur layers causes layer 1 to have a larger spacing of 3.160(2)Å, and layer 2 to have a smaller spacing of 3.133(2)Å. In the notation of hexagonal close-packed layers, the Li_2FeS_2 structure can be described by the stacking symbol

$$A \begin{smallmatrix} a \\ b \end{smallmatrix} B \ \gamma \ A \begin{smallmatrix} a \\ b \end{smallmatrix} B \ \gamma$$

where the capital letters denote the relative sequence of the sulfur layers, the small letters are the iron or lithium in layer 1, and the greek letters represent the lithium in layer 2.

In our model, the lithium site (0,0,0) has point symmetry $\bar{3}m$ with a $Li - S$ distance of 2.7441(8)Å. The tetrahedrally coordinated iron and lithium have point symmetry $3m$ with $Fe - S$ distances of 2.4126(15)Å along the three-fold axis and 2.3737(7)Å to the three "basal" sulfur atoms. The $M - M$ distance, where M = Fe or Li, is 2.8012(14)Å. The refined occupancy for an iron atom only at a tetrahedral site in layer 1 is 0.533(4). This significant increase over half iron occupancy is attributed to half lithium occupancy in this layer. Since there is no evidence of a superstructure, the iron and the lithium atoms are thought to be equally disordered over all the tetrahedral sites within layer 1.

To a first approximation, assuming the angular dependence of Li and Fe scattering factors, and the movement of Li and Fe are the same, the lithium contribution to the refined occupancy can be calculated using

$$x\ f(\mathrm{Fe}) + (1 - x)\ f(\mathrm{Li}^+) = 0.533(4) \times f(\mathrm{Fe}), \qquad (4.1.1)$$

for Li atoms, and

$$x\ f(\mathrm{Fe}) + (1-x)\ f(\mathrm{Li}) = 0.533(4) \times f(\mathrm{Fe}) \qquad (4.1.2)$$

for Li^+ ions, where x is the fraction of Fe in layer 1, $f(\mathrm{Fe})$, $f(Li^+)$ and $f(\mathrm{Li})$, which are the number of scattering electrons for Fe, Li^+, and Li, are 26, 2, and 3 respectively. For Li^+, $x = 0.49$, whereas for Li, $x = 0.47$. This is consistent with half iron and half lithium occupancy of each tetrahedral site within layer 1. A random distribution of Li and Fe is also consistent with more than one iron site in the Mössbauer spectrum (5). Table V summarizes the atom positions in Li_2FeS_2.

An alternate treatment of the randomly distribution of iron and lithium atoms among the tetrahedral sites using a scattering factor f such that

$$f = 0.5\ f(\mathrm{Fe}) + 0.5\ f(\mathrm{Li}) \qquad (4.1.3)$$

was not attempted. Although this treatment considers the angular dependence of iron and lithium scattering factors, it, again, assumes that the movement of iron to be the same as the lithium. In addition, this treatment assumes full occupancy of the site with 50% iron and 50% lithium, and therefore, does not allow refinement of the occupancy of the site. Since the difference in angular dependence of these scattering factors, over the range of interest, is small, our treatment of data is thought to yield results which are just as accurate.

TABLE V - Atom Positions in Li_2FeS_2

ATOM	OCC.†	x	y	z	$U_{11}(Å^2)$	$U_{33}(Å^2)$	$U_{iso}(Å^2)$
Fe	0.533(4)	$\frac{1}{3}$	$\frac{2}{3}$	0.36775(16)	0.0174(4)	0.0221(5)	—
S	1	$\frac{2}{3}$	$\frac{1}{3}$	0.24894(13)	0.0203(4)	0.0173(5)	—
Li	1	0	0	0	—	—	0.045(4)
Li‡	(0.5)	$\frac{1}{3}$	$\frac{2}{3}$	0.36775	—	—	—

† - OCCUPANCY

‡ - This lithium is disordered among the tetrahedral sites of layer 1 with the iron atoms. It was not included in the refinement but is reflected in the greater than 50% occupancy of the tetrahedral sites by the iron.

4.1.3 Crystal Structure of $LiFe_{1.5}S_2$ ($Li_2Fe_3S_4$)

The compound $LiFe_{1.5}S_2$ (sample I), which belongs to space group $P\bar{3}m1$, is isostructural with Li_2FeS_2. The lattice parameters of this selected crystal are $a = 3.851(2)\AA$, and $c = 6.305(3)\AA$. The unit cell of the two compounds has very similar c axes but differs in a. Refinement proceeded by fixing the iron occupancy at $\frac{3}{4}$.

Like Li_2FeS_2, the structure is based on a hexagonal close-packed arrangement of sulfur atoms. Three-quarters of the tetrahedral sites in layer 1 are randomly filled by iron atoms while lithium atoms occupy all the octahedral sites in layer 2. Figure 15b shows a schematic of this layered structure. The spacing within the sulfur layers of layer 1 shows an increase to $3.181(2)\AA$, whereas layer 2 shows a decrease to $3.123(2)\AA$. The interatomic distances in this compound have decreased in comparison with Li_2FeS_2. The Li-S distance is $2.7170(11)\AA$ and the Fe-S distances are $2.3959(2)\AA$ along the three-fold axis and $2.3583(11)\AA$ to the "basal" sulfur atoms. Table VI summarizes the atom positions in $LiFe_{1.5}S_2$.

TABLE VI - Atom Positions in $LiFe_{1.5}S_2$

ATOM	OCC.†	x	y	z	$U_{11}(\AA^2)$	$U_{33}(\AA^2)$	$U_{iso}(\AA^2)$
Fe	0.75	$\frac{1}{3}$	$\frac{2}{3}$	0.37233(8)	0.0164(2)	0.0172(2)	—
S	1	$\frac{2}{3}$	$\frac{1}{3}$	0.24768(9)	0.0159(2)	0.0141(2)	—
Li	1	0	0	0	—	—	0.035(3)

† - OCCUPANCY

It should be noted that the crystal, from which the structure of $LiFe_{1.5}S_2$ was determined, was selected from a batch of Li_2FeS_2 powder (sample I). Lattice constants determined for the batch had the usual Li_2FeS_2 unit cell dimensions ($a = 3.9063(9)\AA$, $c = 6.2960(23)\AA$). The selected crystal was not typical of the batch and attempts to re-synthesize this phase, as will be discussed in section 4.1.4, were unsuccessful.

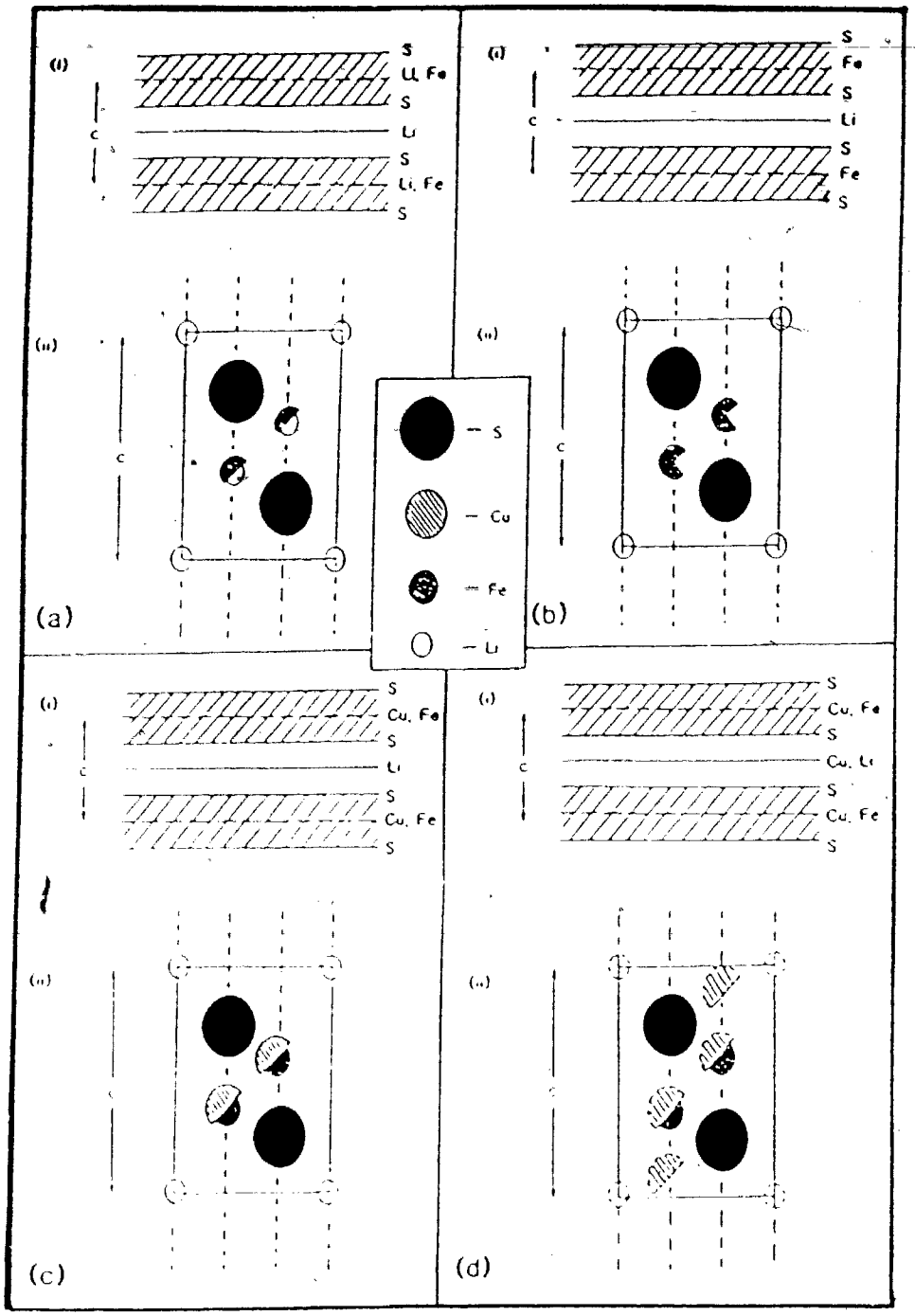

Figure 15: Schematic diagrams of the crystals: (a) Li_2FeS_2, (b) $LiFe_{1.5}S_2$, (c) $LiCuFeS_2$, and (d) $Li_{1-\delta}CuFeS_2$. (i) Schematic diagram of the stacking sequence of the layered structures. (ii) the (110) projection of the structures.

4.1.4 Synthesis of $Li_xFe_3S_4$

Several attempts to synthesize $Li_2Fe_3S_4$ on a large scale yielded mixtures of products, and their lattice constants bore no resemblance to that of $Li_2Fe_3S_4$. Table VII summarizes the reactions and the observed products. The syntheses in table VII demonstrate that $Li_2Fe_3S_4$ is not a stable phase at temperatures above 300°C. Although these experiments were unsuccessful, it does not preclude the existence of the phase. Instead, it leads us to think that the Li-Fe-S phase diagram is far more complex, and that a more detailed study of conditions for synthesis is necessary in order to study this new phase.

The key difference between $Li_2Fe_3S_4$ and Li_2FeS_2 is the lattice constant a. A decrease in the a - axis was observed when one sample of Li_2FeS_2 was briefly exposed to air at room temperature. The refined parameters obtained were $a = 3.888(3)\AA$ and $c = 6.286(3)\AA$. The proposed reaction is

$$3\ Li_2FeS_2 + 4\ H_2O \xrightarrow{R.T.} Li_2Fe_3S_4 + 2\ H_2S + 4\ LiOH \qquad (4.1.4)$$

This implies that $Li_2Fe_3S_4$ is a metastable phase which forms at room temperature. Thus, a plausible explanation is that the crystal from which the crystallographic data was collected may have been briefly exposed to air.

TABLE VII - Attempted Synthesis of $Li_xFe_3S_4$

Sample Name	Proposed Reaction	Observed Products
U	$2\ Li + 2\ FeS_2 + Fe \xrightarrow[NAPH/THF]{300°C} Li_2Fe_3S_4$	$Li_2S + FeS_2 + FeS + Fe$
V	$2\ Li + 2\ FeS_2 + Fe \xrightarrow[NAPH/THF]{400°C} Li_2Fe_3S_4$	$Li_2FeS_2 + FeS$
W	$3\ Li + 2\ FeS_2 + Fe \xrightarrow[NAPH/THF]{400°C} Li_3Fe_3S_4$	$Li_2S + FeS + Fe + S$
X	$4\ Li + 2\ FeS_2 + Fe \xrightarrow[NAPH/THF]{400°C} Li_4Fe_3S_4$	$Li_2FeS_2 + Fe$
Y	$2\ Li_2S + 3\ FeS_2 + 3\ Fe \xrightarrow{900°C} 2\ Li_2Fe_3S_4$	$Li_2FeS_2 + FeS$
Z	$6\ Li_2S + 5\ FeS_2 + 7\ Fe \xrightarrow{400°C} 4\ Li_3Fe_3S_4$	$Li_2S + FeS_2 + Fe$
AA	$6\ Li_2S + FeS_2 + 5\ Fe \xrightarrow{400°C} 2\ Li_6Fe_3S_4$	$Li_2S + FeS_2 + Fe$

4.2 The $Li_{2-x}Cu_xFeS_2$ $(0 \leq x \leq 1)$ Phase

4.2.1 Materials Synthesized

The $Li_{2-x}Cu_xFeS_2$ phase, where $x = 1, \frac{2}{3}$, and $\frac{1}{4}$, was prepared. Over this range of composition, this copper substituted phase forms a solid solution. Powder X-ray patterns show that these compounds can be indexed with a hexagonal unit cell. Figure 16 shows the variation of the lattice parameters with x. As the amount of copper substituted for lithium increases the a - axis decreases, while the c - axis increases. The lattice parameters for $Li_{\frac{1}{3}}Cu_{\frac{2}{3}}FeS_2$ ($a = 3.836(2)$Å and $c = 6.333(3)$Å) are in good agreement with those reported by Melandres and Tani et al. (5).

The preparations of these compounds were carried out by the NAPH/THF procedure followed by heating to 800°C. The products had a golden metallic lustre, whereas Li_2FeS_2 was dark grey. A 50 g batch of $LiCuFeS_2$ (sample R) was prepared at 800°C. Following heating, the weight of the sample changed from 49.916 g to 49.595 g, corresponding to a weight loss of 0.321 g. This is equivalent to, at most, $\Delta x = 0.204$ in $Li_{1-x}CuFeS_2$, assuming that the weight loss can be accounted for only by the loss of lithium. A similar weight loss was also observed in the preparation of Li_2FeS_2 crystals. There, a weight loss of 0.434 g which corresponded to $\Delta x = 0.194$ in $Li_{2-x}FeS_2$ is observed. But in both cases, since the reaction was carried out in a continuous flow of Argon, under unsealed conditions, it is possible that the weight loss may also involve sulfur evaporation.

Deintercalaton of lithium for this phase was carried out by using I_2/AN. Unlike the removal of lithium in Li_2FeS_2, these compounds do not disproportionate. Instead, they retain the hexagonal close-packed framework, and form the Cu_xFeS_2 phase. Figure 17 shows the lattice parameters of Cu_xFeS_2 versus x.

Several attempts were made to prepare single crystals of the Cu_xFeS_2 phase. Delithiation by the conventional method (ie. with stirring), pro-

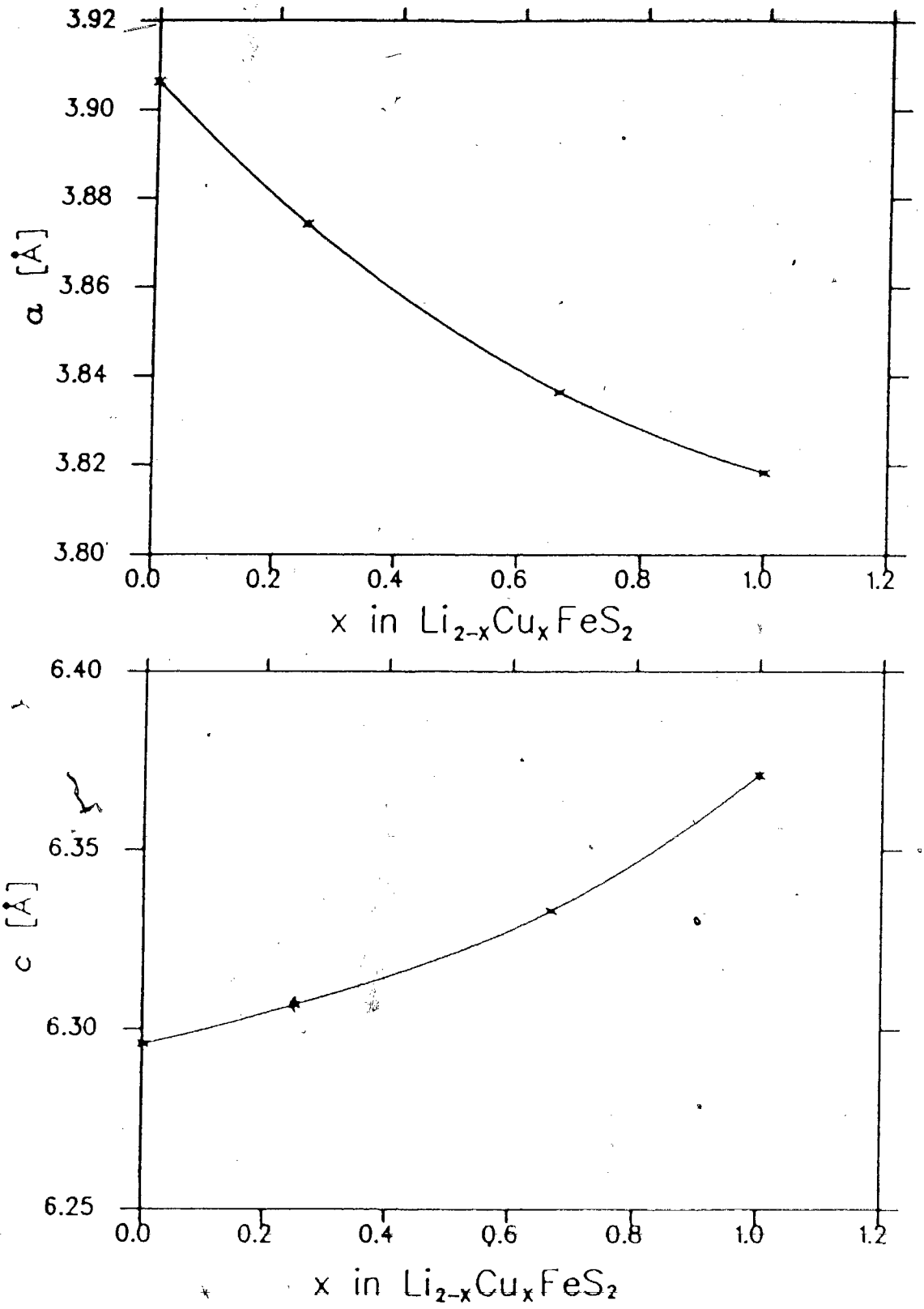

Figure 16: Variation of lattice parameters a, and c in $Li_{2-x}Cu_xFeS_2$ with x.

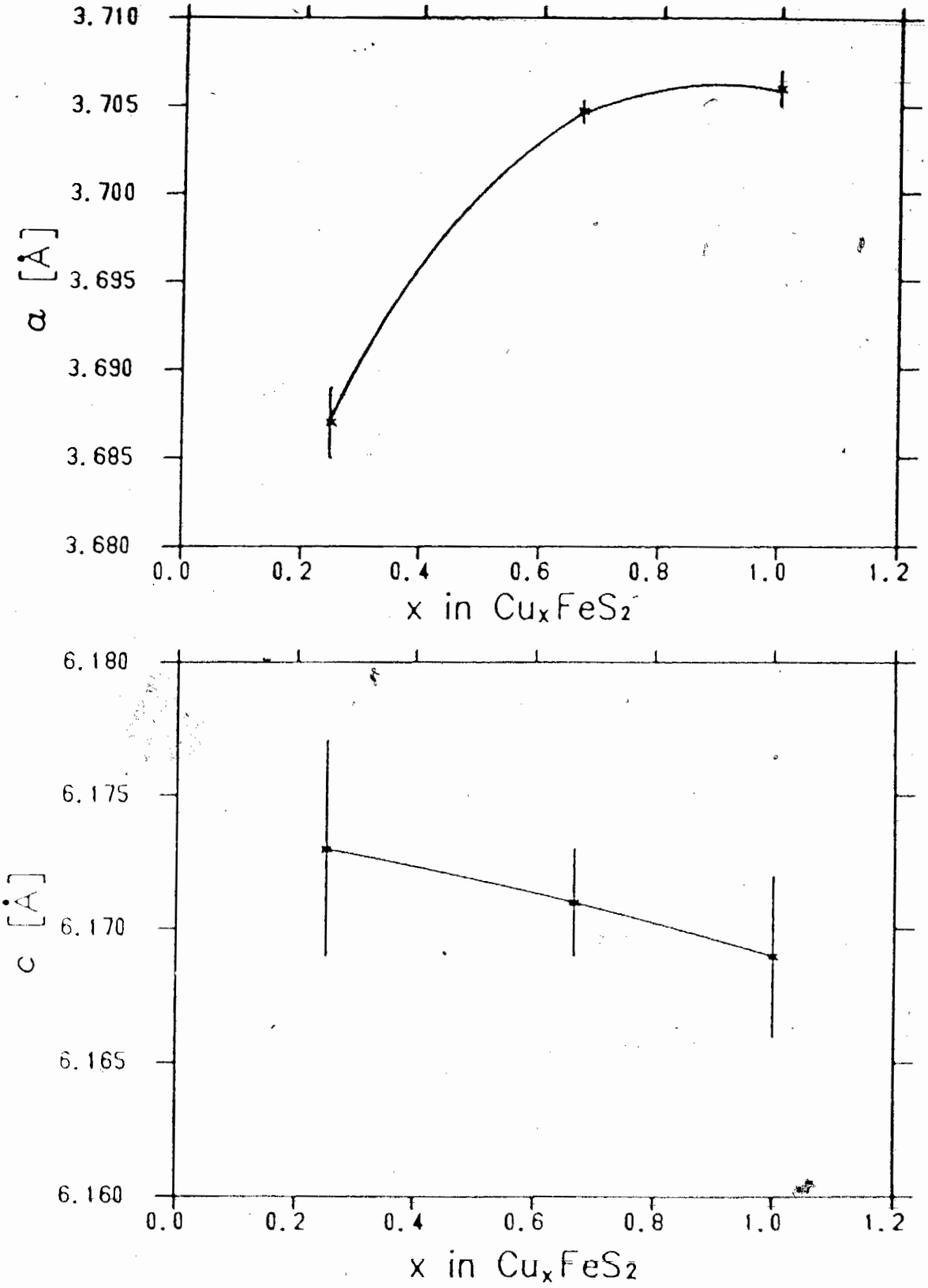

Figure 17: Variation of lattice parameters a, and c in Cu_xFeS_2 with x.

duced unsuitable microcrystalline plate-like crystals less than 0.05 mm. In another attempt, fragments of the lithiated compound were placed in a solution of I_2/AN. The reaction was allowed to proceed without disturbance for a week, and powder X-ray diffraction confirmed that Cu_rFeS_2 had formed. However, structure determination was unsuccessful because the crystal allowed only 2 or 3 diffraction peaks to be observed, and they were very broad and weak.

A third attempt was made to obtain a single crystal of a partially delithiated compound, $Li_{1-\delta}CuFeS_2$. The batch (sample S) from which the structure of $Li_{1-\delta}CuFeS_2$ was determined was prepared without stirring. But more importantly, delithiation was done more slowly. It was hoped that under these conditions the crystals would be more likely to retain their crystallinity and yet would still give indications of any structural changes. The initial amount of iodine dissolved in AN was equivalent to $\delta = 0.35$. The reaction was allowed to proceed until the solution turned clear; an indication that the reaction was complete. At this stage, a single crystal was selected, and the empirical formula, based on the iodine added, was $Li_{0.65}CuFeS_2$.

4.2.2 Crystal Structure of $LiCuFeS_2$

Analysis of symmetry equivalent reflections showed that $LiCuFeS_2$ (sample R) belonged to the space group $P\bar{3}m1$. Refinement began with the atomic parameters taken from the Li_2FeS_2 analogue. The three atoms which were included in the refinement were Fe, S, and Li. Initial refinement assumed that all the tetrahedral sites within layer 1 were only filled by iron atoms. Thus, the refined occupancy of Fe, as shown in table VIII, was 1.055(7). This is equivalent to full occupancy of the tetrahedral sites by a species with 27.5 electrons, or a 50% probability of each site being filled by either an iron or a copper atom, since $\frac{26+29}{26+26} = 1.058$. Thus, copper is present in layer 1 and the ratio of Fe to Cu is 1:1. Figure 15c shows the schematic of this structure and table VII summarizes the atom positions of $LiCuFeS_2$.

TABLE VIII - Atom Positions in $LiCuFeS_2$

ATOM	OCC. †	x	y	z	$U_{11}(Å^2)$	$U_{33}(Å^2)$	$U_{iso}(Å^2)$
Fe/Cu ‡	1.055(7)	$\frac{1}{3}$	$\frac{2}{3}$	0.37327(8)	0.0150(2)	0.0196(2)	—
S	1	$\frac{2}{3}$	$\frac{1}{3}$	0.24587(12)	0.0115(2)	0.0130(3)	—
Li	1	0	0	0	—	—	0.032(3)

† OCCUPANCY

‡ - The copper is disordered among the tetrahedral sites of layer 1 with the iron atoms. It was not included in the refinements but the greater than 100% occupancy of the tetrahedral sites of the iron gives full occupancy of a species with 27.5 electrons. This is the averaging effect arising from the disordered arrangement of iron and copper atoms within layer 1.

An absorption correction was applied using the empirical method. This involved measuring the transmission of X-rays of a series of single reflections while the crystal rotated 360°. Although preferrence is given to applying absorption correction by the analytical procedure, this method was not used since an adequate description of the crystal was not possible.

For comparison, refinement proceeded using both methods of correction. The analytical method yielded a R_f value of 0.046 but the empirical method gave a significantly lower R_f value of 0.033.

The crystal structure of $LiCuFeS_2$ is isostructural with Li_2FeS_2. Since no superstructure is found, the copper and iron atoms are randomly and equally distributed over the tetrahedral sites in layer 1. The lithium atoms occupy the octahedral sites between the adjacent sulfur layer. The copper substitution for lithium in layer 1 has resulted a slightly increased spacing of 3.228(2)Å and a decreased spacing of 3.124(2)Å for layer 2.

4.2.3 Crystal Structure of $Li_{1-\delta}CuFeS_2$

As mentioned in section 4.2.1, the empirical formula of the partially delithiated compound, based on the reaction with iodine, was $Li_{0.65}CuFeS_2$ (sample S). Analysis of symmetry equivalent reflections showed that this compound belonged to the space group $P\bar{3}m1$. The diffraction peaks were in general broad (base scan width $\doteq 2.9°$) and weak. Thus, data collection only extended up to 60° in 2θ. The lattice constants for this compound are $a = 3.7724(18)$Å, and $c = 6.2646(15)$Å. Evidence shows that these lattice constants describe the unit cell of a substructure, and that an unsolved superstructure exists.

Initial structure refinement proceeded with three atoms, Fe, S, and Li. A partial occupancy of the Fe site was obtained during the initial cycles of refinement. A difference map at this point showed a peak near the three-fold axis in the layer occupied by the lithium atoms. A copper atom, Cu, was placed at this site and the occupancy was refined. It was evident that the removal of lithium atoms from the structure has resulted in a movement of copper atoms from layer 1 to the adjacent layer 2. Figure 15d shows the schematic of this structure and table IX summarizes the atom positions of the compound

TABLE IX Atom Positions in $Li_{1-\delta}CuFeS_2$

ATOM	OCC. †	x	y	z	$U_{11}(Å^2)$	$U_{33}(Å^2)$	$U_{iso}(Å^2)$
Fe ‡	0.869(13)	$\frac{1}{3}$	$\frac{2}{3}$	0.37131(19)	0.0139(6)	0.0213(8)	
Cu	0.131(5)	$\frac{1}{3}$	$\frac{2}{3}$	0.1300(12)	—	—	0.020(29)
S	1	$\frac{2}{3}$	$\frac{1}{3}$	0.25114(29)	0.0127(9)	0.0228(11)	—
Li	0.90(18)	0	0	0			0.063(17)

† OCCUPANCY

‡ - the refined occupancy of 0.869(13) gives approximately $\frac{1}{2} : \frac{1}{3}$ Fe:Cu ratio in layer 1.

Layer 1 consists of tetrahedral sites partially filled by iron and copper atoms. The refined occupancy of 0.869(13) gives $\frac{1}{2} : \frac{1}{3}$ iron to copper ratio within the layer. As a result, the occupancy of Cu in the tetrahedral sites

in layer 2 should be approximately $\frac{1}{6}$. The refined occupancy for an iron atom in layer 2 is 0.145(7). This corresponds to an equivalent copper atom occupancy of 0.131(5).

Layer 2 consists of octahedral sites partially filled by lithium atoms, and tetrahedral sites partial filled by copper atoms. It is probably the ordering of the filled sites that leads to the existence of a superstructure.The occupancy of lithium in layer 2 refined to 0.9(2). Since lithium is a weak scatterer of X-rays, the error associated with this value is large and is only a qualitative indication that the amount of lithium in this compound is reduced. The empirical formula, derived from the amount of iodine, gives an accurate determination of the amount of lithium present.

Of the four atoms, the position of the Cu atom in layer 2 is least accurately placed. A description of the motion anisotropically gives thermal parameters which are effectively equal in magnitude. Therefore, inclusion of these extra parmeters is not justified. Attempts to reduce the motion result in a slight displacement of the atom from the three-fold axis. Since thermal motion and position are correlated, it is impossible, with the present data, to arrive at a more accurate position for this atom.

4.3 Electrochemical Measurements

4.3.1 Li/FeS_2 and Li/Li_2FeS_2 Cells

The discharge mechanism for the first discharge of Li/FeS_2 cells has been studied. Figure 18 shows the first discharge of these cells at 21, 30, 37, 55, and 75°C at a rate of 20 hours for $\Delta x = 1$. When the cells are discharged at temperatures above 37°C, the reaction proceeds step-wise, as follows.

$$2\ Li + FeS_2 \longrightarrow \underset{(\text{'}I\text{'}phase)}{\text{''}Li_2FeS_2''} \qquad (4.3.1)$$

$$\underset{(\text{'}I\text{'}phase)}{2\ Li + \text{''}Li_2FeS_2''} \longrightarrow 2\ Li_2S + Fe \qquad (4.3.2)$$

These reactions are reflected as double plateaus in the $V(x)$ curves. From the thermodynamics of the cell, as discussed in section 3.2.3, these plateaus are indications of two distinct phase transitions in a ternary system (represented by the equilateral triangle in figure 3). Although figure 3 shows the equilibrium phases of the Li-Fe-S system at 450°C, there are similarities between this phase diagram and that which is observed at lower temperatures. The top plateau which involves reaction 4.3.1, is a phase transition along a tie line joining FeS_2 and Li_2FeS_2. This corresponds to moving along A to E on the ternary phase diagram in figure 3. Since coexisting phases on the tie line have the same chemical potential, the voltage of the cell, at any point on the tie line, is the same. At the end of the plateau at $x = 2$, the cathode is entirely converted to the intermediate 'I' phase. Upon further discharge to $x = 4$, a lower plateau which involves reaction 4.3.2 occurs. This reaction corresponds to the movement through E to L in figure 3. Thermodynamics states that the number of coexisting phases on a plateau of a ternary system must be three. From in-situ X-ray diffraction experiments, two of the three phases, as shown in figure 19, are unambiguously identified as Li_2S and Fe. The third phase, although undetected by X-ray diffraction, must be the intermediate product, the 'I' phase. The inability of X-ray diffraction to detect this phase leads to the conclusion that 'I' phase, formed electrochemically, must be amorphous. Furthermore, it

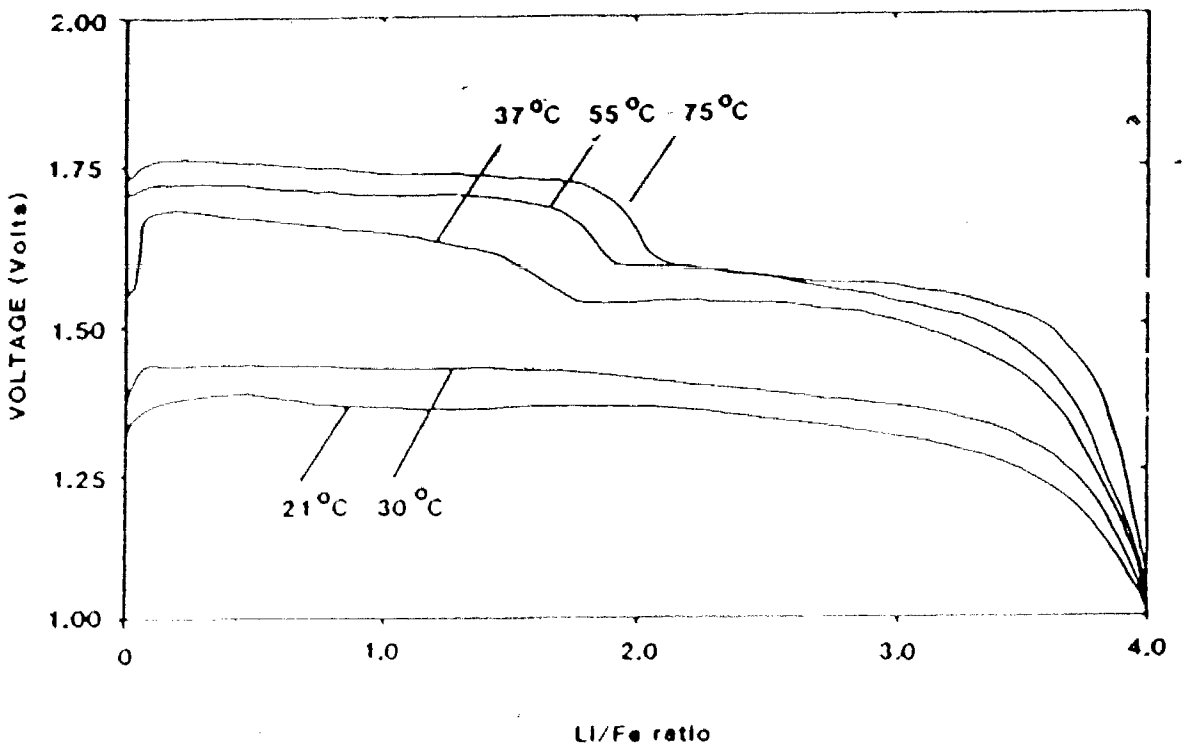

Figure 18: The $V(x)$ curves of the first discharge of Li/FeS_2 at temperatures ranging from 21 to 75°C. The appearance of the double plateau is observed at temperatures > 37°C.

will be shown, later in this section, that the intermediate 'I' phase which coexists with Li_2S and Fe on the lower plateau is Li_2FeS_2.

At room temperature the discharge mechanism is a one-step reaction.

$$4\ Li + FeS_2 \longrightarrow 2\ Li_2S + Fe \qquad (4.3.3)$$

Here, the coexisting phases on the single plateau are FeS_2, Li_2S, and Fe. At the end of the phase transitions, the cathode is comprised of a mixture of Li_2S and Fe. These plateau voltages are extremely temperature sensitive, and their temperature dependence are shown in figure 20.

Recently, a step-wise reaction at 20°C was observed (23). Figure 21 shows the discharge characteristics of Li/FeS_2 cells (SONY Energytec Inc.) under various loads, 10, 22, 30, 47, and 100 kohms. Assuming 100% cathode utilization, they are equivalent to discharge rates of approximately 75, 154, 208, 321, and 662 hours for $\Delta x = 1$ respectively. It seems that the discharge mechanism proceeds via the formation of an intermediate phase, even at room temperature, when the discharge rate is slowed to and beyond 154 hours for $\Delta x = 1$.

To support the proposed step-wise formation of an intermediate 'I' phase at elevated temperatures, the voltage profiles of the first recharge of a Li/FeS_2 cell which had been discharged to $x = 2$ at 37°C, and the charging of a cell assembled with Li_2FeS_2 cathode (Li/Li_2FeS_2) were compared. These voltage curves which are shown in figure 22 appear to be similar in shape. Since $V(x)$ curves reflect thermodynamic properties, the observed similarity of $V(x)$ curves indicates that the intermediate 'I' phase must be Li_2FeS_2. From the chemical deintercalation of Li_2FeS_2 with I_2/AN, the reaction products are $Li_{2-x}FeS_2$, FeS_y, and S. Therefore, the coexisting phases on the plateau at 2.5 volts must be $L_{2-x}FeS_2$, FeS_y, and S. For the voltage region between 1.7 and 2.4 volts, a detailed discussion can be found in section 4.3.2.

By contrast, the first recharge of a Li/FeS_2 cell which has been discharged to $x = 2$ or $x = 4$ at room temperature has the general appearance shown in figure 23. The difference between this and figure 22 is because, in the former case, lithium is removed from the intermediate compound,

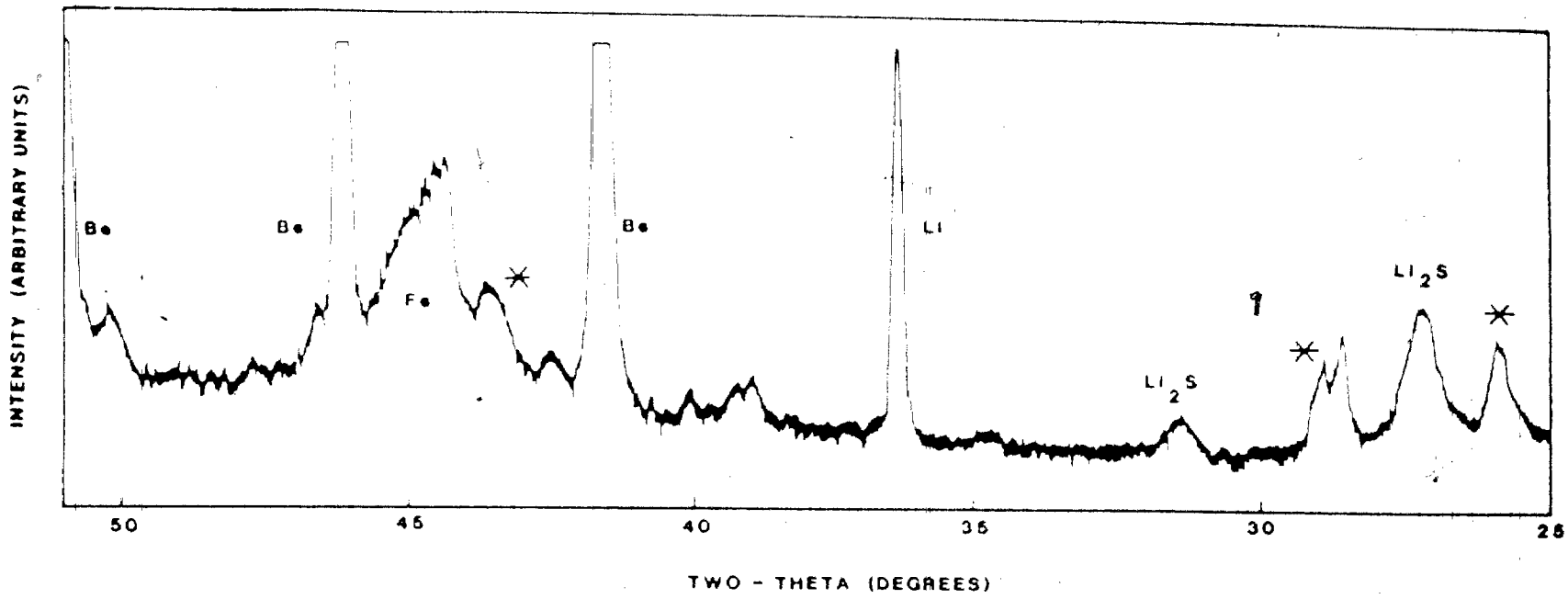

Figure 10. As Li/FeS_2 discharges through the lower plateau, the formation of Li_2S and Fe is observed by in-situ powder X-ray diffraction. '*' indicates extraneous peaks due to the cell holder and the separator in the cell. 'Be' indicates peaks due to beryllium.

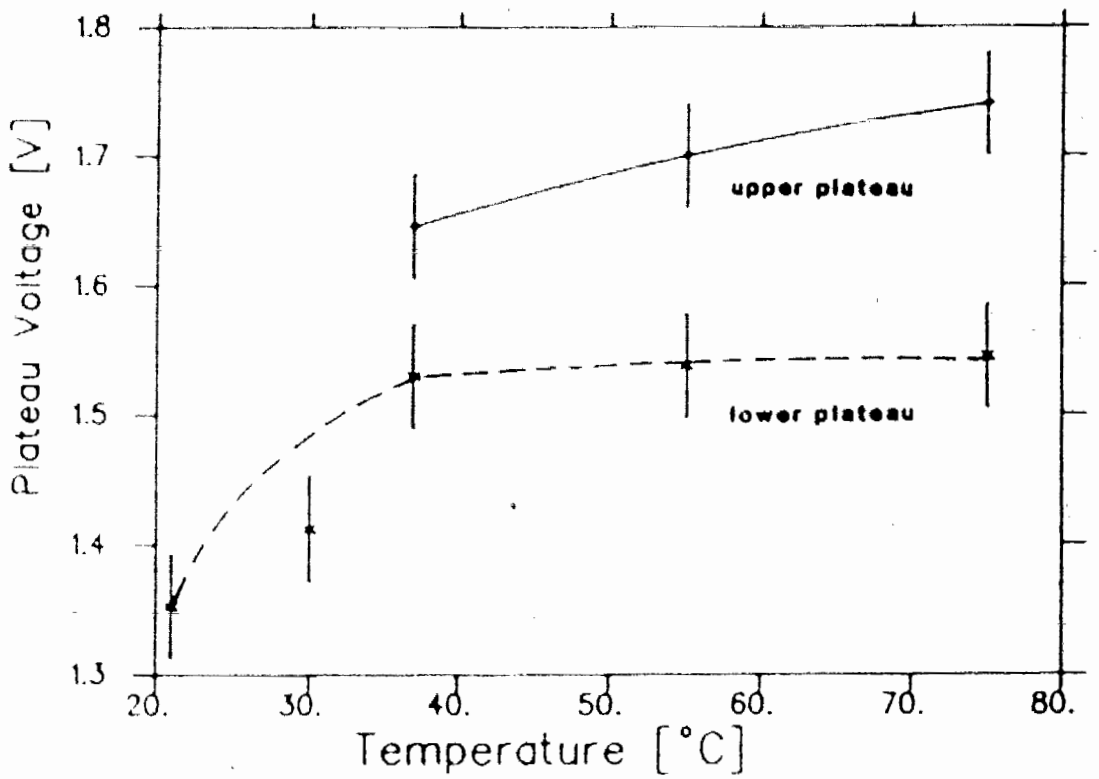

Figure 20: The temperature dependence of the upper and lower plateau voltages of the first discharge of Li/FeS_2.

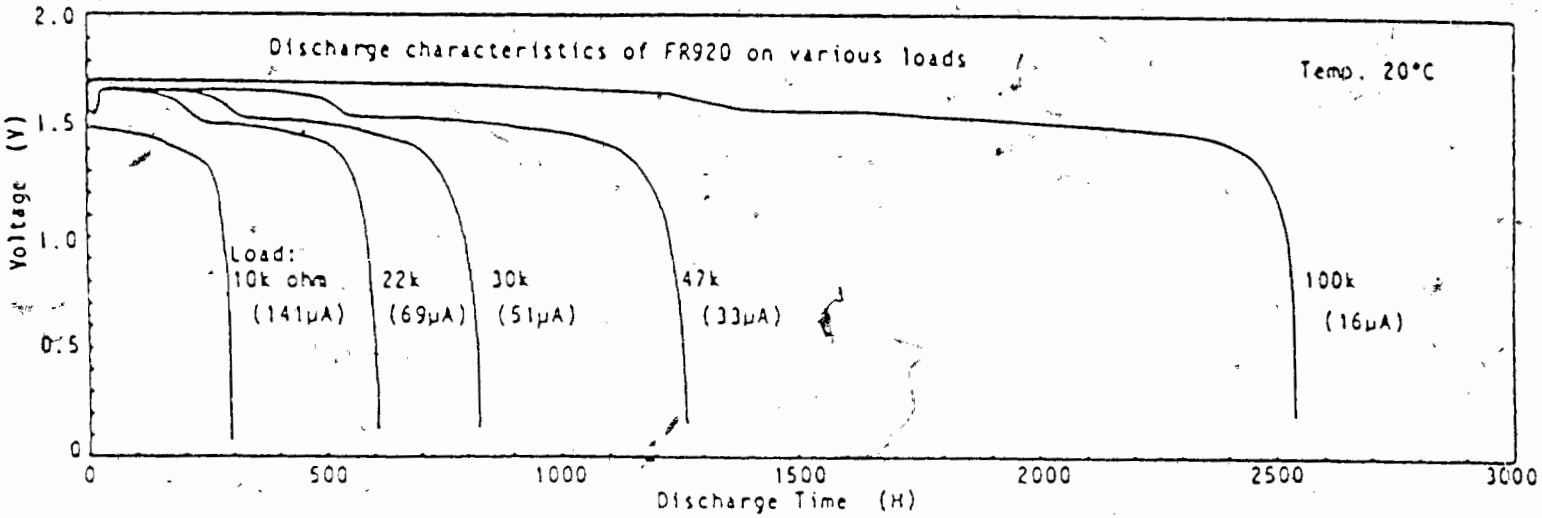

Figure 21. The discharge characteristics of Li/FeS_2 (SONY Energytec Inc.) under various loads at 20°C. At sufficiently slow discharge rate, the double plateau is observed at room temperature discharge.

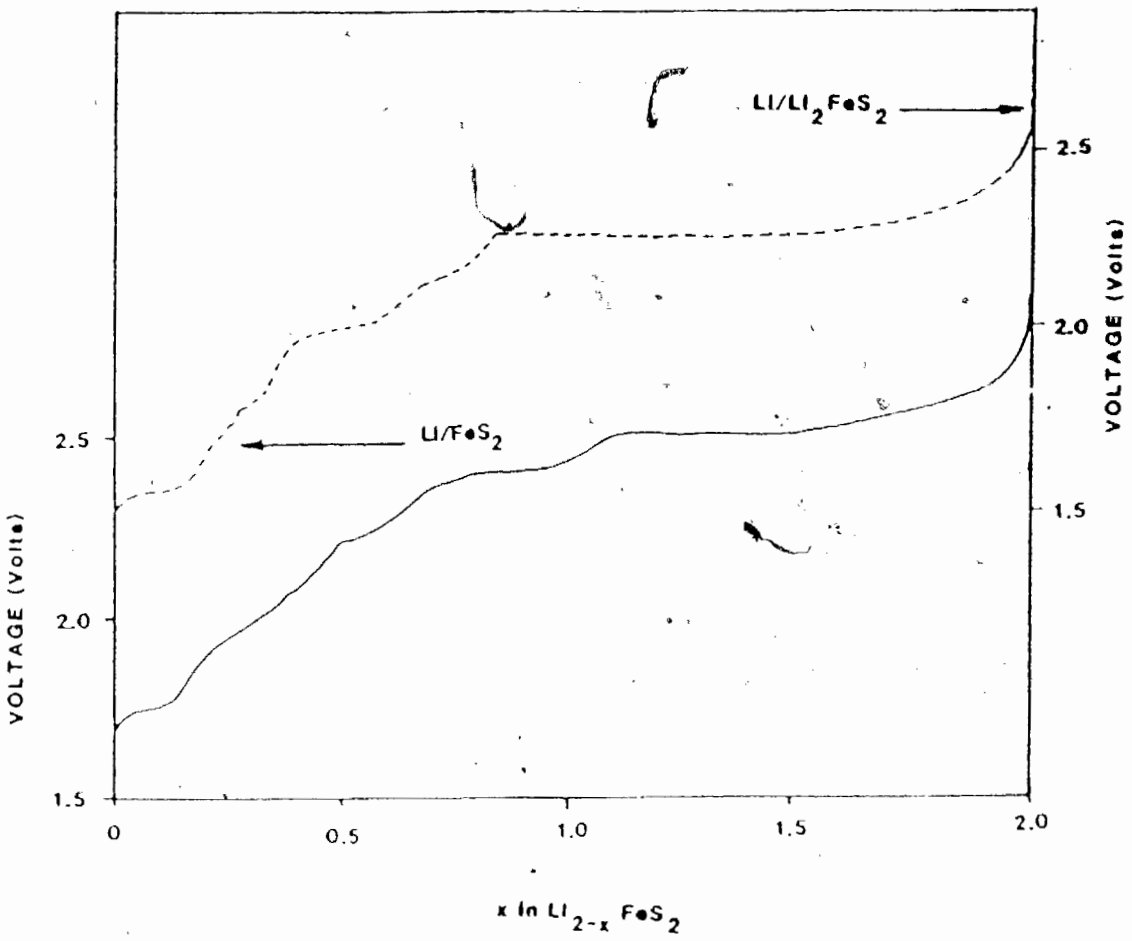

Figure 22: A comparison of the recharge of Li/Li_2FeS_2 at 21°C and Li/FeS_2 which has been discharged to $x = 2$ at 37°C. In both cases, lithium is removed from the intermediate compound, Li_2FeS_2.

Li_2FeS_2, while in the latter case, the removal of lithium is from a mixture of Li_2S and Fe. The three coexisting phases on the lower plateau at 1.7 volts are Li_2S, Fe, and Li_2FeS_2. This corresponds to moving through L to E in the ternary phase diagram in figure 3. By the same argument, the first recharge of Li/FeS_2 cells which had been discharged to $x = 4$ at elevated temperature should exhibit similar features since according to equation 4.3.2, at $x = 4$, the reaction product is a mixture of Li_2S and Fe. Figure 23 compares these voltage curves and shows that they are indeed similar. Furthermore, subsequent to a complete discharge to 1.0 volt, the voltage profiles of Li/FeS_2 and Li/Li_2FeS_2 cells exhibit similar characteristics. This is because after the discharge to 1.0 volt, both cathodes are comprised of a mixture of Li_2S and Fe, and therefore, the cell chemistries of these cells in subsequent charge and discharge are the same. These voltage profiles are shown in figure 24.

As shown in figure 25, the voltage curve of the first and second discharge of a Li/FeS_2 cell bear no resemblance. This difference is observed because at the start of the second discharge the cathode is not comprised of the starting material, pyrite. Instead, from X-ray diffraction, at the onset of the second discharge, the cathode is comprised of a mixture of FeS_y and S. The reason for the formation of FeS_y and S instead of pyrite is not understood. But it is one of the major differences between Li/FeS_2 cells operated at low temperatures and at 450°C.

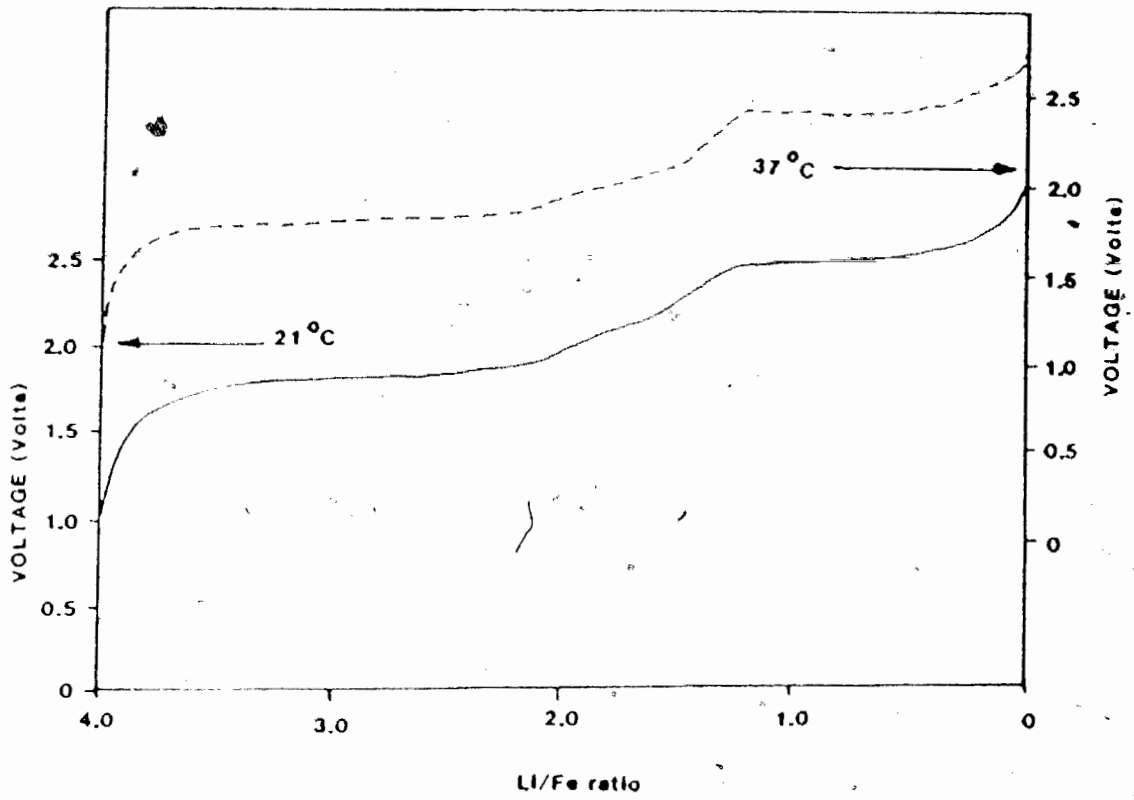

Figure 23: A comparison of the recharge of Li/FeS_2 at 37°C after a previous discharge to 1.0 volt, and the recharge of Li/FeS_2 which has been discharged to $x = 2$ or 4 at 21°C. In both cases, lithium is removed from a mixture of Li_2S and Fe.

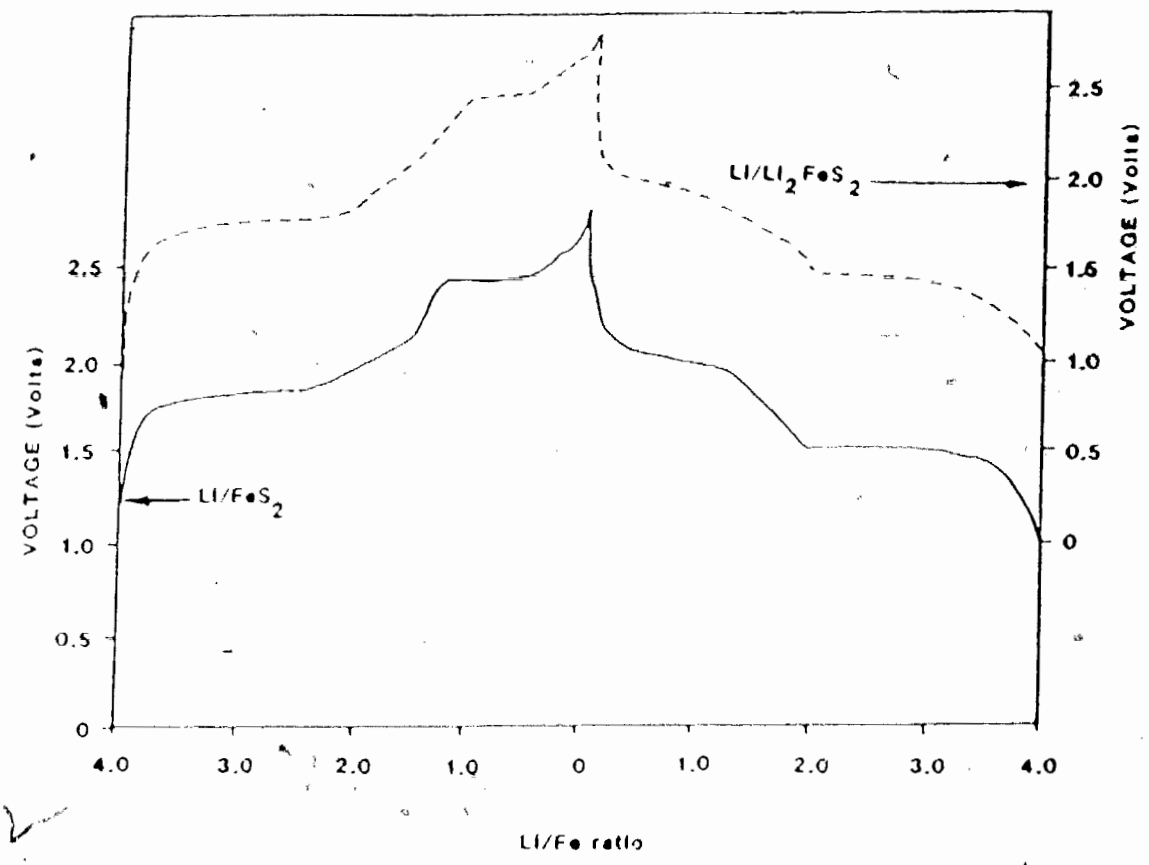

Figure 24:, Subsequent to a complete discharge to 1.0 volt, the $V(x)$ curves of Li/Li_2FeS_2 and Li/FeS_2 are similar.

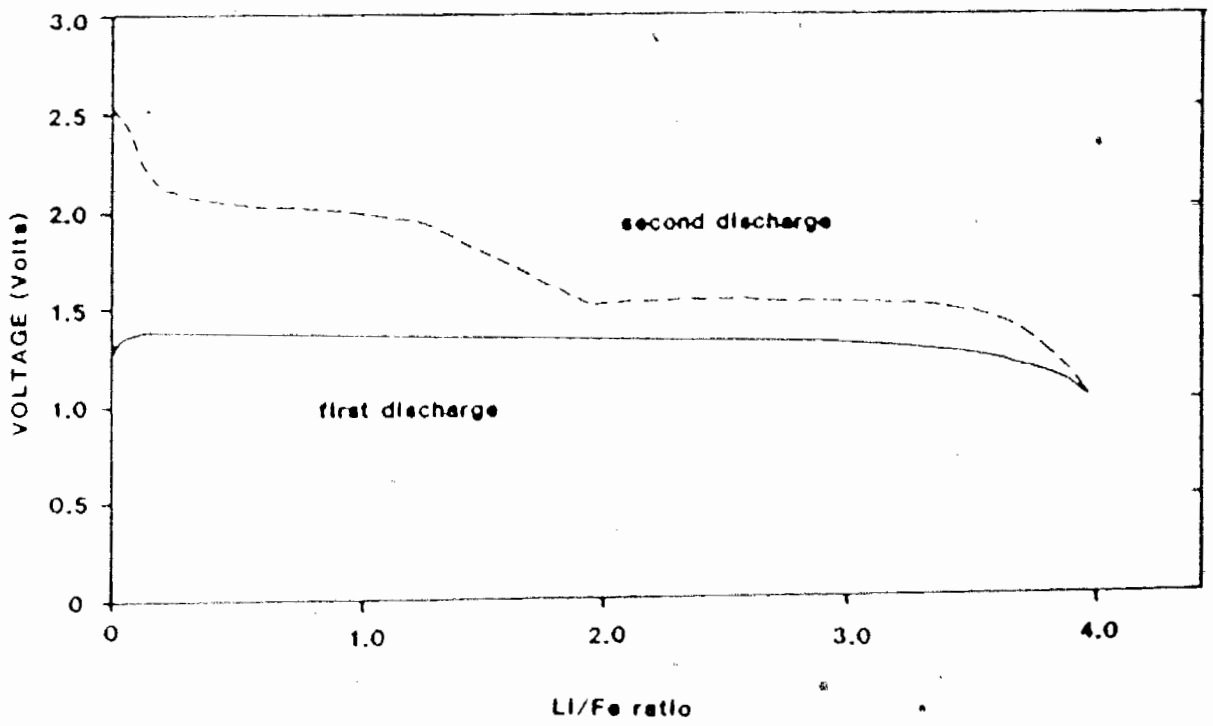

Figure 25: The first and second discharge of Li/FeS_2.

4.2.2 The Reversible Voltage Range in Li/Li_2FeS_2 Cells

An in-situ X-ray diffraction study on Li/Li_2FeS_2 cells shows that between the voltage range of 1.5 to 2.4 volts, the cycling behaviour of Li_2FeS_2 is reversible. A Li/Li_2FeS_2 cell has an open circuit voltage of about 1.71 volts. Upon recharge to 2.4 volts, the diffraction peaks associated with Li_2FeS_2 shrink and broaden, and several new broad peaks appear. When the cell is discharged to 1.71 volts, the diffraction pattern returns to that of the newly assembled cell. Figure 26 shows portions of the X-ray diffraction patterns taken during these experiments.

From the cycling results of Li/Li_2FeS_2 cells at constant current, it is concluded that the reversible voltage regime actually extends between 1.45 and 2.4 volts. Figure 27 shows the $V(x)$ curve of such a cell. Its behaviour is thought to be reversible in that each charge and discharge has the same shape. Cycling through this region, bounded between the upper and lower plateaus at 2.5 and 1.4 volts respectively, is thought to correspond to moving through E and F in the ternary phase diagram in figure 3

For a ternary system, when the voltage varies with x thermodynamics predicts that the number of phases present over this voltage range must be one or two. From a knowledge of the $Li_{1-\delta}CuFeS_2$ structure, it is believed that during the recharge of Li_2FeS_2 to 2.4 volts, as lithium atoms are gradually removed from layer 2, the vacant sites are filled by the diffusion of lithium from layer 1 into layer 2. This gives a single phase of varying composition, $Li_{2-x}FeS_2$, where $x \simeq 0.8$, at 2.45 volts. If lithium ordering occurs, then this region may have two phase regions within it. At 2.45 volts, a phase with approximate composition of $Li_{1.2}FeS_2$ exists. It is thought that the movement of Li from the tetrahedral sites near the Fe atoms introduces large stresses to the structural framework, and hence, as observed from the X-ray patterns, poor crystallinity results. On discharge, the process is reversible in that, as lithium is inserted back into the octahedral sites of layer 2, the lithium atoms which are already in layer 2 diffuse back into the tetrahedral sites of layer 1. Therefore, for $0 < x \leq 0.8$ (between 1.45 and 2.45 volts), $Li_{2-x}Fes_2$ is a true intercalation compound.

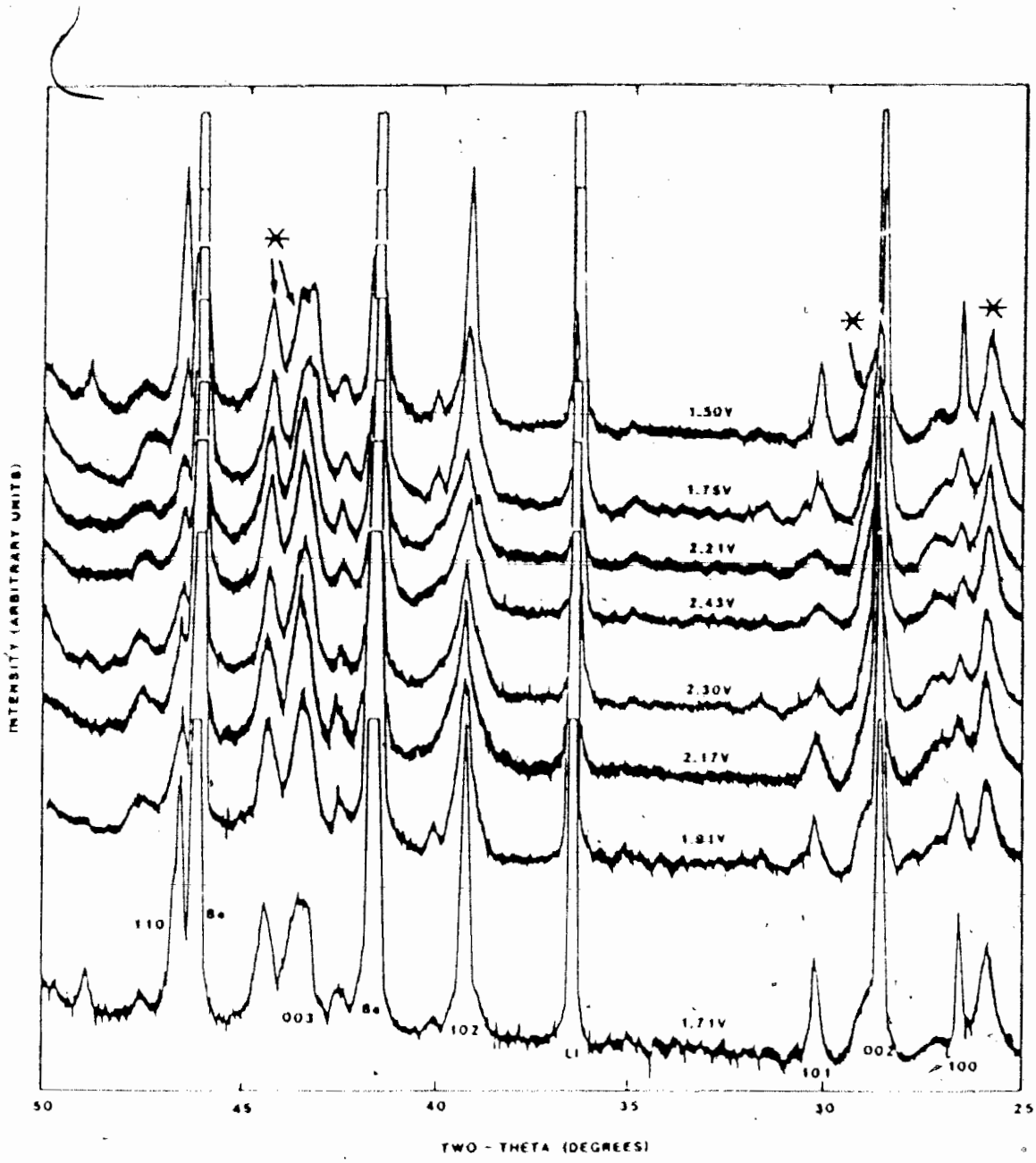

Figure 26: Portions of the X-ray diffraction patterns showing the peak variations in the reversible voltage range, 1.45 volts to 2.4 volts, of Li/Li_2FeS_2. The diffraction peaks due to Li/Li_2FeS_2 are labelled. '*' indicates extraneous peaks due to the cell holder and the separator in the cell. 'Be' indicates peaks due to beryllium.

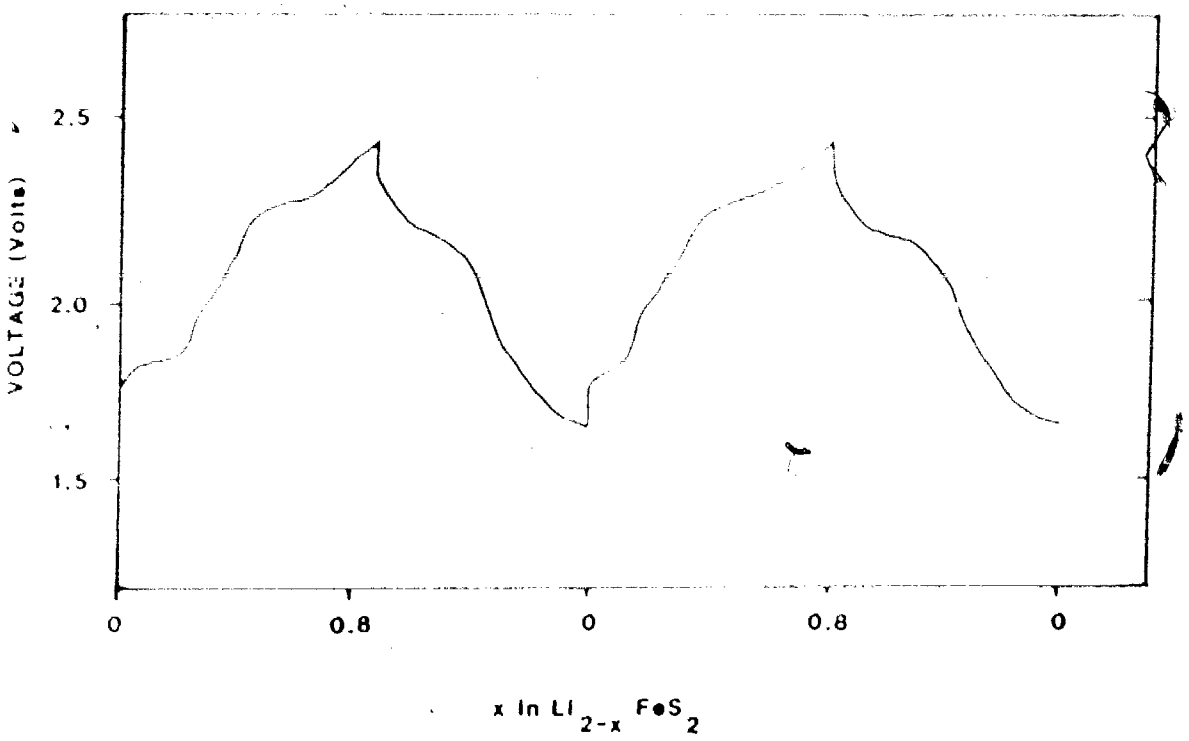

Figure 27: The voltage profile of the reversible voltage range in Li/Li_2FeS_2 cells.

Beyond these voltage limits, disproportionation to materials of different Fe and S ratio results.

4.3.3 Mössbauer Study on FeS_2 and Li_2FeS_2

4.3.3.1 Li_2FeS_2 and Delithiated Li_2FeS_2

Mössbauer spectra of Li_2FeS_2 and delithiated Li_2FeS_2, prepared by I_2/AN, were measured at room temperature. Figure 28a shows the fitted room temperature spectrum of crystalline Li_2FeS_2 (sample J). The spectrum is consistent with the presence of two quadrupole split doublets. These quadrupole splittings arise from interaction of the electric quadrupole moment of the excited ^{57}Fe nucleus with the electric field gradient. Two major contributions to the electric gradient are due to the electronic environment about the nucleus arising from the valence electrons, and the asymmetry in the arrangement of atoms around the Mössbauer nuclei. Hoggins et al. (24) reviewed a number of closely related systems containing iron which is tetrahedrally coordinated by sulfur. These compounds are of the general form $M_xFe_yS_z$ where M = Na, K, Rb, Cs, and Ba. Examination of these data suggests that an IS of 0.17-0.20 mm/sec with an associated quadrupole splitting of 0.4 - 0.6 mm/sec is diagnostic for high-spin tetrahedral Fe^{3+}. Whereas, an isomer shift of approximately 0.6 mm/sec with a large QS is indicative of high-spin tetrahedral Fe^{2+}. The final IS and QS values of the spectrum, fitted with two overlapping quadrupole doublets of equal IS, but of unequal intensity and splittings, is in agreement with empirically predicted IS and QS ranges for Fe^{2+} which is tetrahedrally coordinated by sulfur, and results reported by Melandres et al. (5). The goodness of fit is given by the parameter χ^2, of which a value of 2.1 is obtained for this spectrum. The consistently lower QS values reported by Melandres is a result of the large scatter observed in his fitted spectrum of Li_2FeS_2 (5).

The overlapping quadrupole doublets, which suggest nonequivalent crystallographic iron sites, are consistent with structural data obtained by single crystal X-ray diffraction. The structure of Li_2FeS_2, as discussed in section 4.1.2, has more than a single iron environment. In fact, a random distribution of iron and lithium in layer 1 results in four different iron environments in the ratio of 3:3:1:1, two of which are apparently sufficiently well resolved by Mössbauer spectroscopy. Table X tabulates the fitted parameters, as well as results reported by Melandres et al (5).

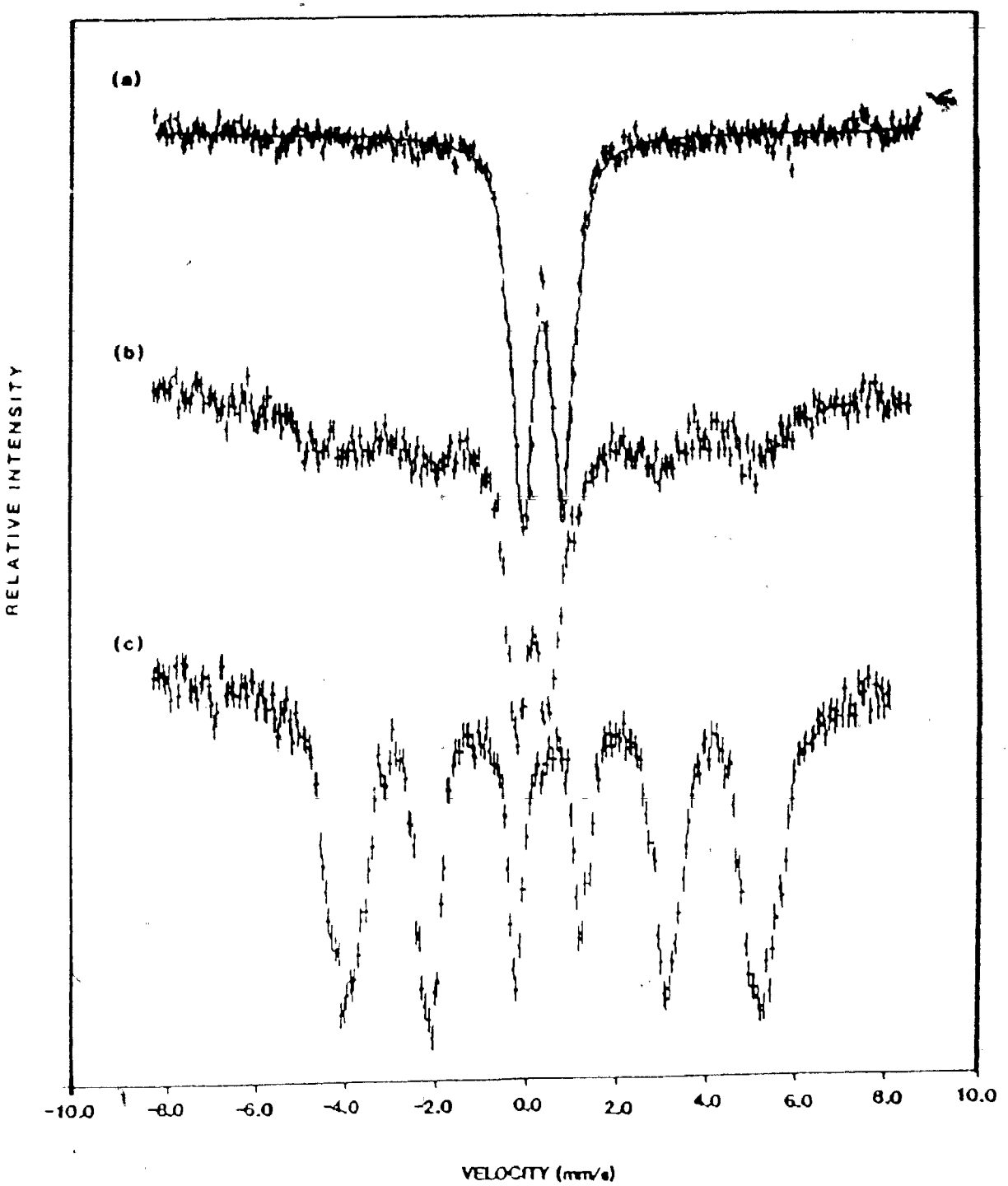

Figure 28: Mössbauer spectra of (a) crystalline Li_2FeS_2, (b) delithiated Li_2FeS_2, and (c) synthesized FeS_y (where $y = 1.064$) from its elements at 450°C.

Figure 28b is a spectrum of delithiated Li_2FeS_2, prepared by I_2/AN (sample K). The spectrum is dominated by several overlapping resonance peaks attributable to the electric field gradient at the iron nucleus. In addition, six broad magnetic hyperfine lines, two of which are hidden beneath the quadrupole doublets, are produced by the interaction of nuclear magnetic dipole moment with the magnetic field present at the nucleus. The magnitude of this hyperfine field, which exists at the iron nucleus, is 292 kG. As mentioned in section 4.1.1, the sample is a mixture of non-stoichiometric $Li_{2-x}FeS_2$, pyrrhotite (FeS_y), and sulfur. Qualitatively, shown in figure 28c, the magnitude of these magnetic splittings compares well to those observed in the spectrum of a mixture comprising of FeS_y, synthesized from its elements at 450°C (sample T). From figure 14, the value of y is determined to be 1.064. At 4.2°K, the center doublets of the chemically delithiated Li_2FeS_2 sample (sample K) become magnetically split, and the spectrum profile bears resemblance to the general features of Li_2FeS_2 measured at 4.2°K (see section 4.3.3.4). Mössbauer spectroscopy shows that the reaction product contains an amorphous and partially delithiated $Li_{2-x}FeS_2$ phase as well as FeS_y and S. This indicates that a reaction time of 20 hours with I_2/AN does not completely remove all the lithium in Li_2FeS_2.

TABLE X - A comparison of the experimentally determined parameters of crystalline Li_2FeS_2 and results reported by Melandres et al. (5).

Crystalline Li_2FeS_2	Experimental Fitted Parameters	Results reported by Melandres et al.
Doublet 1:		
Isomer shift (mm/s)	0.53(2)	0.50(2)
Quadrupole splitting (mm/s)	0.89(6)	0.62(2)
FWHM (mm/s)	0.53(2)	0.4
% Area	94(4)	
Doublet 2:		
Isomer shift (mm/s)	0.53(2)	0.49
Quadrupole splitting (mm/s)	1.69(6)	1.46(2)
FWHM (mm/s)	0.23(2)	0.4
% Area	6(4)	

4.3.3.2 Initial Discharge of Li/FeS_2 Cell at 55°C

An in-situ Mössbauer experiment on the discharge of Li/FeS_2 at 55°C shows evidence which supports reactions 4.3.1 and 4.3.2. Figure 29 shows Mössbauer spectra of such a cell at $x = 0$, 2, and 4. At $x = 0$, the FeS_2 spectrum, modelled by a pair of quadrupole doublets can be fitted to yield a χ^2 of 1.5. At $x = 4$, the spectrum is fitted to iron metal, and unreacted FeS_2. In the intermediate stage of discharge, at $x = 2$, the spectrum bears no resemblance to that of crystalline Li_2FeS_2, shown in figure 28a. But since Li_2FeS_2, formed electrochemically, is amorphous, it is not unlikely that their Mössbauer spectra are different. Due to poorly resolved features, fitting of this spectrum is not attempted. But more importantly, as predicted by the step-wise reactions, the magnetic dipole splitting due to iron metal is not observed at $x < 2$. A summary of final IS and QS values are tabulated in table XI.

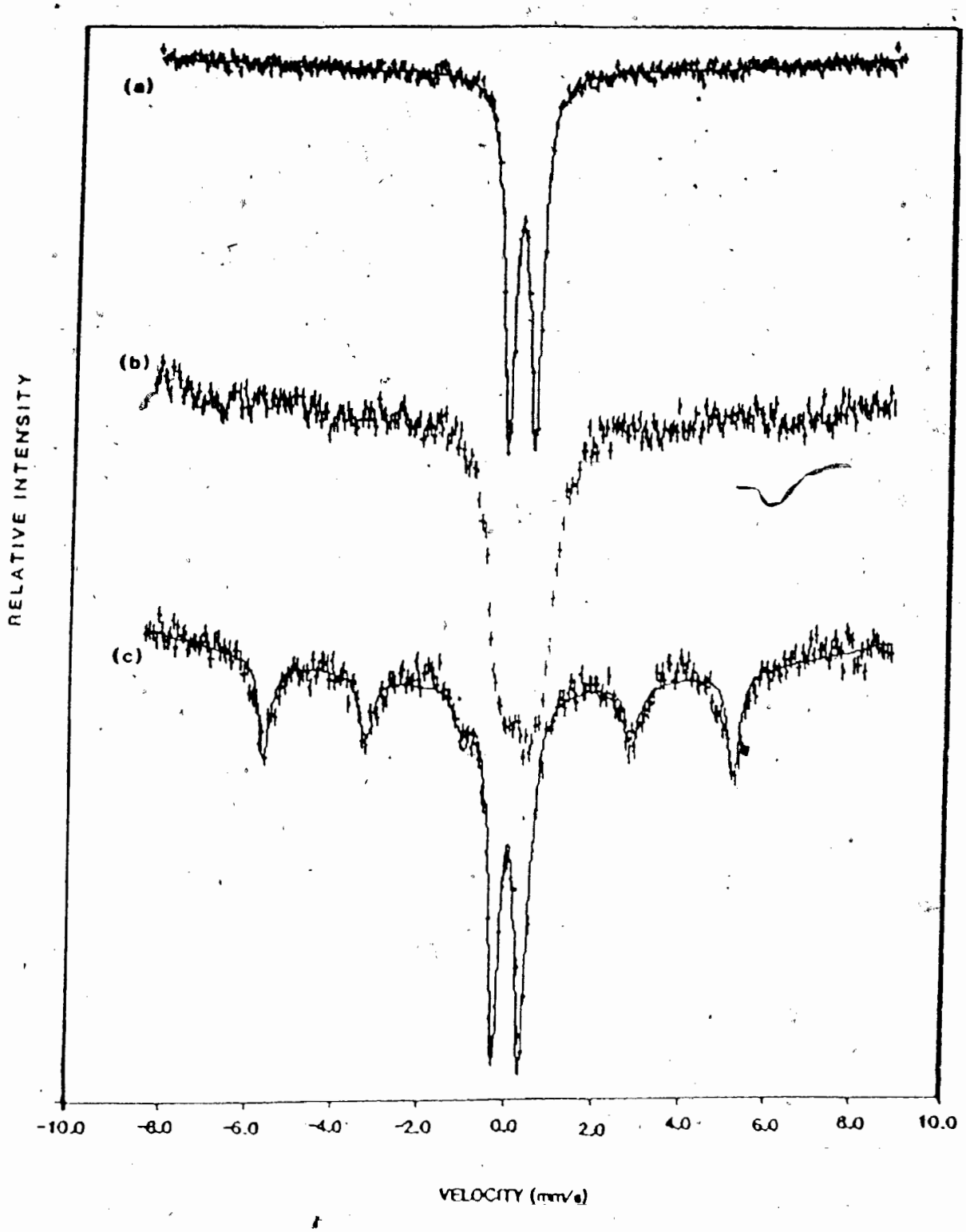

Figure 29: Mössbauer spectra of the discharge of an in-situ Li/FeS_2 cell at 55°C, at (a) $x = 0$, (b) $x = 2$, and (c) $x = 4$.

TABLE XI - The fitted parameters of the first discharge of a Li/FeS_2 cell at 55°C at $x = 0$, and 4.

Li/FeS_2 Cell	Isomer shift (mm/s)	Quadrupole Splitting (mm/s)	Magnetic Field (kG)	FWHM (mm/s)	% AREA
at x = 0; FeS_2	0.28(2)	0.61(6)	—	0.32(2)	100
at x = 4;					
(1) Fe	0.00(2)	—	330	0.29(2)	37
(2) unreacted FeS_2	0.28(2)	0.61(6)	—	0.32(2)	64

4.3.3.3 Comparative Study of Li/FeS_2 and Li/Li_2FeS_2 Cells

Figure 30 shows a typical $V(x)$ curve of the first recharge of a Li/Li_2FeS_2 cell. Marked on the curve are the equilibrium voltages at which spectra of in-situ Mössbauer cells are measured. These cells, Li/FeS_2 and Li/Li_2FeS_2, are maintained at their operating temperatures of 55°C and 25°C respectively. The Li/FeS_2 cell is initially discharged at a rate of 20 hours for $\Delta x = 1$ to a voltage limit of 1.58 volts. From figure 18, this is equivalent to taking the cell to the end of the upper plateau and thus, converting the cathode to the intermediate 'I' phase, Li_2FeS_2. At this point, both cells are subsequently charged by the constant voltage method described in section 3.2.5. After measuring the spectra at 2.80 volts, the cathodes of these cells are recovered and transferred into gas-tight sample holders for Mössbauer measurements at liquid helium temperature (4.2°K).

Electrochemical oxidation of Li/Li_2FeS_2 shows that up to the removal of 0.8 lithium, the species which undergoes oxidation is iron. As mentioned in section 4.3.3.1, Mössbauer spectroscopy can resolve two of the four different crystallographic iron sites in Li_2FeS_2. Thus, the fitting of the sequence of Mössbauer spectra, displayed in figure 31, modelled consistently with two sets of quadrupole doublets, is attempted. In the fitting procedure, the FWHM (full-width-half-maximum) of each doublet is constrained to the values which best fitted the initial compound, Li_2FeS_2. A correction to base-line curvature is applied to the spectra at $x < 1$. At $x > 1$, magnetic hyperfine splittings are observed. The magnitude of these splittings corresponds well to those observed in figure 28c, the spectrum of non-stoichiometric FeS_y, synthesized from its elements at 450°C. Since pyrrhotite, formed electrochemically is a non-stoichiometric mixture of FeS_y, fitting a mixture of magnetic sites was not attempted.

At 2.80 volts, the spectrum is similar in some respects to that of chemically delithiated Li_2FeS_2. This resemblance is also observed in the spectrum measured at 4.2°K, where the center doublets, observed in the room temperature spectrum, are magnetically split, and overlapping the magnetic lines of pyrrhotite (section 4.3.3.4). This complex spectrum sug-

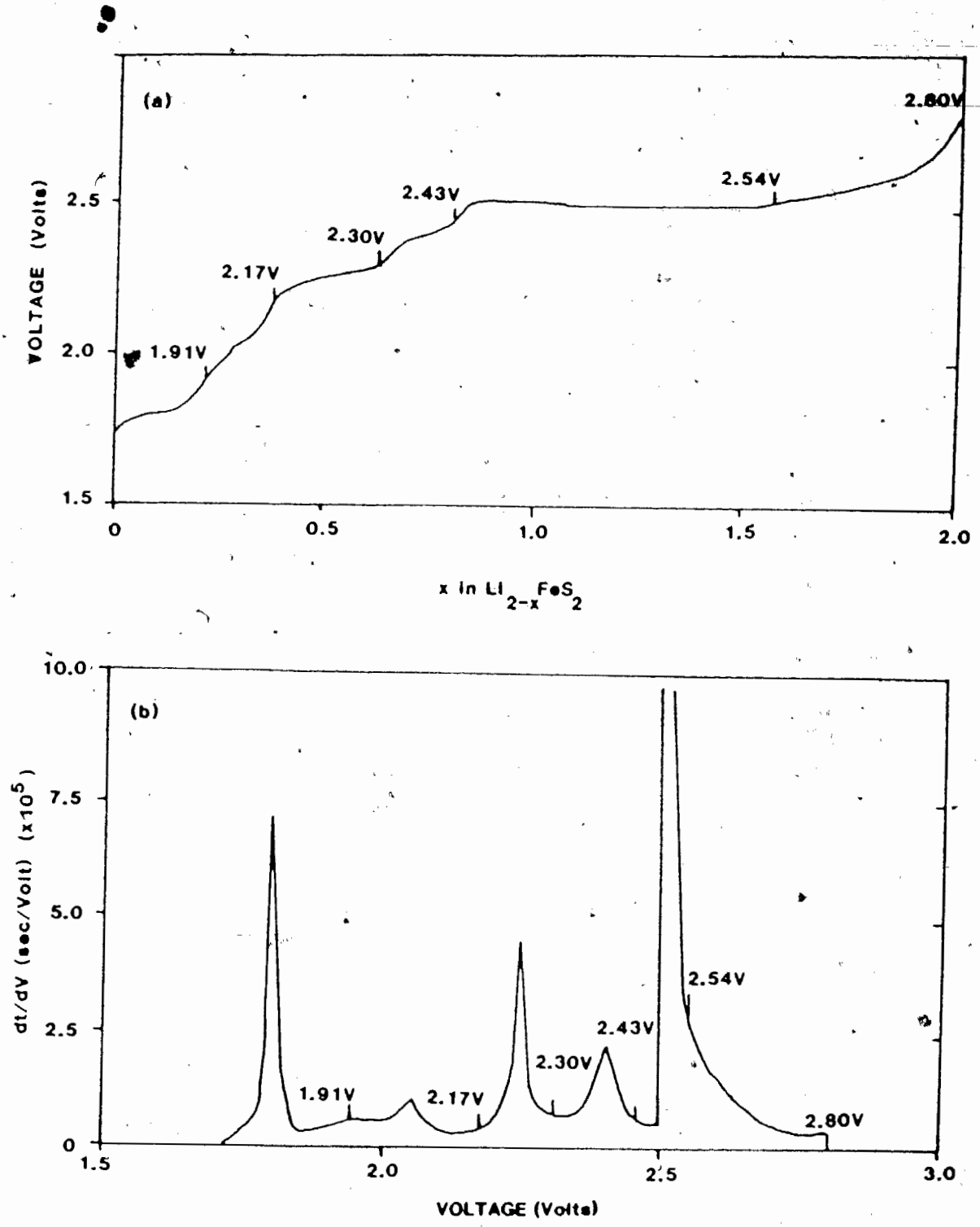

Figure 30. (a) The $V(x)$ curve of the first recharge of Li/Li_2FeS_2. (b) The dt/dV vs. V curve of (a). Indicated on these curves are the voltages at which Mössbauer spectra are measured.

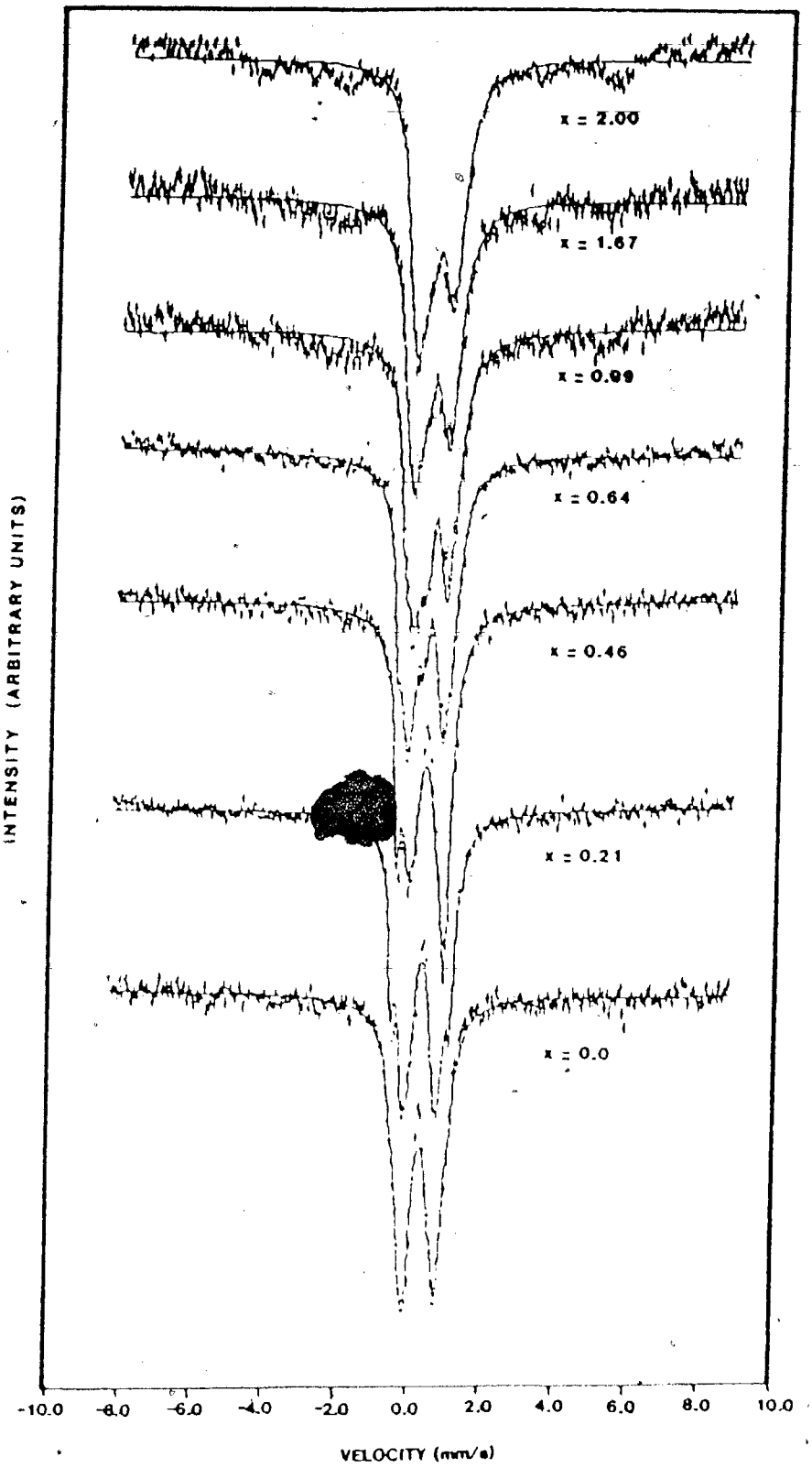

Figure 31. The sequence of Mössbauer spectra obtained at various stages of recharge of a Li/Li_2FeS_2 in-situ Mössbauer cell. These spectra are recorded at room temperature.

$Li_{2-x}FeS_2$ is in coexistence with FeS_y and S. The presence of $Li_{2-x}FeS_2$ means incomplete removal of lithium from the cathode. From the point of view of thermodynamics, it means that the Li/Li_2FeS_2 cell has not reached equilibrium at a voltage of 2.80 volts. However, since the Mössbauer cell is fabricated between two 0.025 cm thick beryllium squares, the cell is very sensitive to beryllium flexing. Excessive flexing can be caused by uneven pressure on the electrode surfaces due to non-uniform lithium plating. As mentioned in section 2.1.2, this leads to poor electrical contact which can result in even poorer cathode utilization. During the recharge of the Li/Li_2FeS_2 cell, beryllium flexing inducing reduced cathode utilization may have been observed. At 2.80 volts, the residual $Li_{2-x}FeS_2$ observed in the Mössbauer spectrum is likely to have been from the portion of the cathode which has become electrically disconnected.

Empirical correlation of isomer shifts of iron with oxiation states are based on the relationship between IS and s-electron densities.

$$IS \propto \frac{\Delta R}{R}\left(\psi_a^2(0) - \psi_s^2(0)\right) \qquad (4.3.4)$$

where $\psi_a^2(0)$ and $\psi_s^2(0)$ refer to the s-electron densities at the nuclei in the absorber and source respectively, R is the mean nuclear radius at the ground state, and $\Delta R = R_{ex} - R_{gr}$. For ^{57}Fe, when the nucleus emits a gamma-ray, the size of the nucleus expands. Thus, the physical constant, $\frac{\Delta R}{R} < 0$. Since s-electron density at the nuclei in the absorber is usually greater than that of the source (ie - $\psi_a^2(0) > \psi_s^2(0)$), higher s-electron densities at the iron nuclei are reflected in a decrease in isomer shifts. As a result, Fe(II), which has a d^6 configuration, has a more positive isomer shift than Fe(III). The removal of a d-electron in the latter species effectively increases the s-electron density at the iron nucleus.

Hoggins et al. (24) empirically correlated the isomer shift, IS_{OS} , of iron (high-spin, and tetrahedrally coordinated by sulfur) with oxidation state, OS, assuming that the magnitude of IS varies linearly with valence state.

$$IS_{OS}(mm/s) = A - B\ (OS), \qquad (4.3.5)$$

where A is a constant, and $B \equiv (IS_{2+} - IS_{3+})$. As mentioned in section 4.3.3.1, Hoggins et al. examined a number of closely related systems which

contained high-spin iron atoms which are surrounded by tetrahedra of sulfur atoms, and chose IS_{3+} to be 0.20 mm/sec, and IS_{2+} to be 0.60 mm/sec. This suggested an empirical relationship,

$$IS\ (\text{mm/s}) = 1.4 - 0.4\ (OS) \tag{4.3.6}$$

Equation 4.3.6 was improved by Goodenough (25), and an alternate empirical formula,

$$IS\ (\text{mm/s}) = 1.68 - 0.5\ (OS) \tag{4.3.7}$$

was obtained.

Since the iron in Li_2FeS_2 is tetrahedrally coordinated by sulfur, an attempt to correlate the series of isomer shifts to the oxidation states of iron for the recharge of a Li/Li_2FeS_2 cell is made. Table XII summarizes the oxidation states for each iron site, the overall weighted average oxidation state of the cathode, and the final IS and QS values obtained from fitting the two overlapping doublets. As shown in figure 32, the IS and QS of doublets 1 and 2 decrease with increasing x in $Li_{2-x}FeS_2$. This means that as lithium is removed from the cathode, both types of iron nuclei are oxidized. The variation of OS with x during the recharge of the Li/Li_2FeS_2 cell is shown in figure 33. In this model, as lithium atoms are removed from the structure, the IS of doublet 1 gradually decreases. Whereas, the IS of doublet 2 drops rather suddenly from 0.37 to 0.03 mm/s at x=0.64. This observed feature is not understood, but, as shown in figure 30, it coincides to the region of the $V(x)$ plot where a change in slope in the curve is observed.

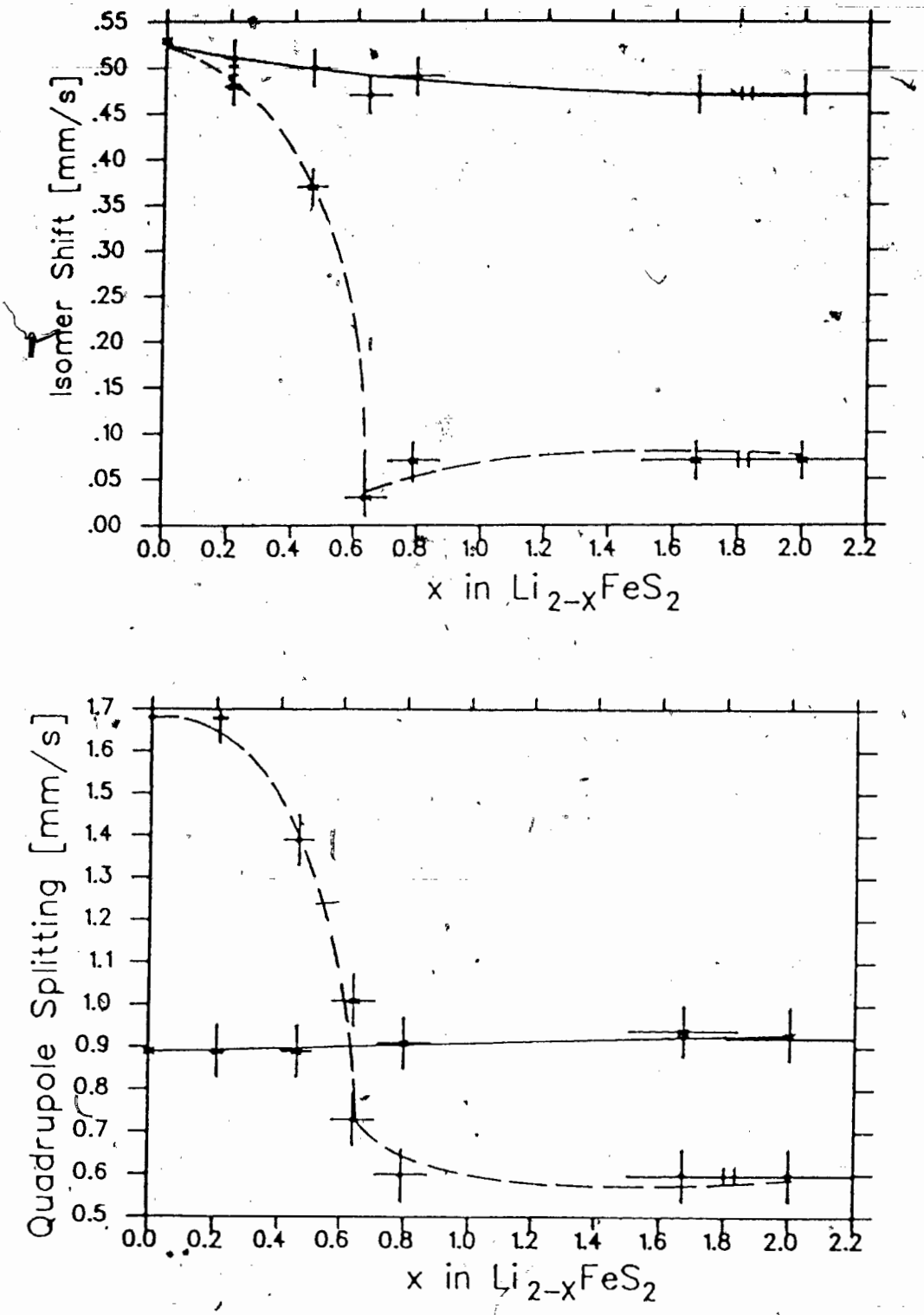

Figure 32. The variations of IS and QS of the two doublets with x in $Li_{2-x}FeS_2$. The solid curve indicates doublet 1 and the dashed curve indicates doublet 2.

TABLE XII - The fitted parameters of the recharge of a Li/Li_2FeS_2 cell.

x in $Li_{2-x}FeS_2$ (±10%)	IS (mm/s) (±0.02)	QS (mm/s) (±0.06)	% AREA (±4)	FWHM (mm/s) (±0.02)	OS (±0.05)	OS of Cathode (±0.05)
$x = 0.00$; (1.71V)						
Doublet 1	0.53	0.89	94	0.53	2.18	2.18
Doublet 2	0.53	1.69	6	0.23	2.18	
$x = 0.21$; (1.91V)						
Doublet 1	0.51	0.89	86	0.53	2.23	2.24
Doublet 2	0.48	1.68	14	0.23	2.30	
$x = 0.46$; (2.17V)						
Doublet 1	0.50	0.89	83	0.53	2.25	2.31
Doublet 2	0.37	1.39	17	0.23	2.58	
$x = 0.64$; (2.30V)						
Doublet 1	0.47	1.01	91	0.53	2.33	2.43
Doublet 2	0.03	0.73	9	0.23	3.43	
$x = 0.79$; (2.43V)						
Doublet 1	0.49	0.91	85	0.53	2.28	2.44
Doublet 2	0.07	0.60	15	0.23	3.33	
$x = 1.67$; (2.54V)						
Doublet 1	0.47	0.94	81	0.53	2.33	2.52
Doublet 2	0.07	0.60	19	0.23	3.33	
$x \simeq 2$; ($\simeq$ 2.8V)						
Doublet 1	0.47	0.93	78	0.53	2.33	2.55
Doublet 2	0.07	0.60	22	0.23	3.33	

During the recharge,the QS of doublet 2 decreases by nearly a factor of three, whereas the QS of doublet 1 remains unchanged. Qualitatively, the quadrupole splitting reflects the symmetry of the bonding environment and the local symmetry of the iron nuclei. At $x = 0.64$, the QS of the outer doublet shows a 50% decrease, as the valency of the iron nuclei change from 2.58 to 3.43. This is because high spin Fe(III) nucleus has a nearly spherically symmetric d^5 electronic configuration. Therefore, a smaller quadrupole splitting is usually observed. A high spin Fe(II) nucleus usually exhibits large quadrupole splitting arising from the asymmetry in the d^6 electronic environment.

The Fe-Fe bond in $Li_{2-x}FeS_2$, at $0 < x < 0.8$, can be assessed by analogy to the previously reported structures in the Ba-Fe-S system (25, 26, 27, 28). These structures are based on a structural scheme consisting of FeS_4 tetrahedra which link, by edge or corner sharing, into infinite chains. These chains are separated by about 6Å from adjacent units and they are in turn linked laterally by barium ions located between the sulfur atoms of the chains. Structural refinement shows that the $Fe-Fe$ distances in these compounds range from 2.83Å to 2.75Å. These bond lengths are comparable to the Fe-Fe bond length in Li_2FeS_2.

Figure 34 displays the sequence of Mössbauer spectra for the Li/FeS_2 cell. Fitting the complete set of spectra was not attempted because the features are poorly resolved. The general changes of the absorption peaks resembles that of the Li_2FeS_2 series, shown in figure 31. A comparison of the spectra of these two cells measured at $x = 0.64$ is shown in figure 35. The sudden decrease of the IS of doublet 2 in the Li_2FeS_2 cell is also observed in the Li/FeS_2 cell. The IS of the outer doublet suddenly shifts to lower velocity, showing a small portion of its peak on the spectrum (labelled A) in figure 35b. This spectrum is fitted with three sets of doublets, doublets $1'$ and $2'$ for Li_2FeS_2, and a doublet for unreacted FeS_2. Doublet $2'$, fitted with the final IS, QS, and FWHM parameters from the Li/Li_2FeS_2 cell, is approximately $\frac{1}{10}$ the area of doublet $1'$. This ratio, tabulated in table XIII, is in agreement with the observed relative areas of these doublets in the Li/Li_2FeS_2 cell. Thus, the series of spectra for both of these cells shows similar features which further supports the previous conclusion, based on

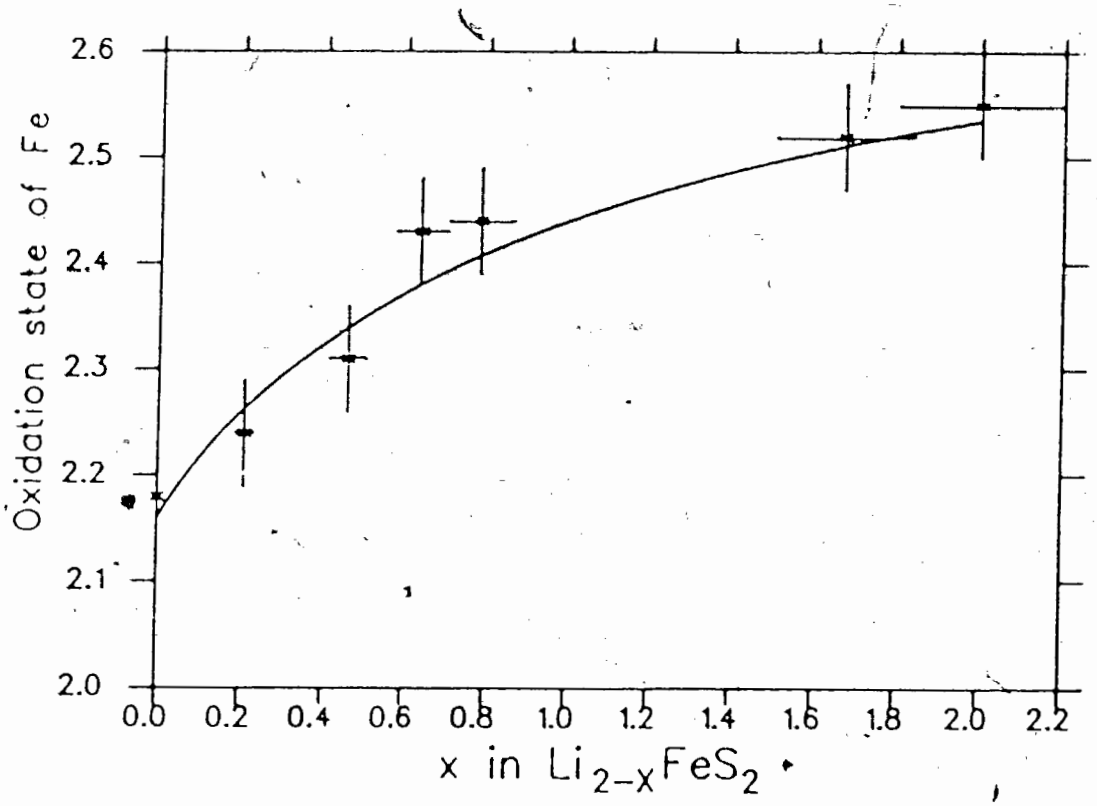

Figure 33: The variation of the overall oxidation state of iron with x in $Li_{2-x}FeS_2$.

electrochemical data, that upon discharge of Li/FeS_2 at temperatures above 37°C, an intermediate phase, which exhibits properties similar to that of Li_2FeS_2, is formed.

TABLE XIII - The fitted parameters of a half-discharged Li/FeS_2 cell on recharge at $x = 0.64$.

x = 0.64 in	Li_2FeS_2 doublets		unreacted FeS_2
$Li_{2-x}FeS_2$	Doublet 2	Doublet 1	
IS (mm/s)	0.03(2)	0.36(2)	0.28(2)
QS (mm/s)	0.73(6)	1.31(6)	0.67(6)
FWHM (mm/s)	0.20(2)	0.56(2)	0.32(2)
% Area	5(2)	56(2)	39(2)

As with the Li/Li_2FeS_2 cell, at voltages above 2.43 volts, magnetic splittings due to pyrrhotite begin to appear. At 2.80 volts, unlike that of the Li/Li_2FeS_2 cell, the spectrum consists of two distinct species, a single doublet due to unreacted FeS_2, and six broad magnetic hyperfine lines split to give a field of the same magnitude as that of non-stoichiometric FeS_y (sample T). At 4.2°K, the spectrum confirms the above interpretation. Thus, it appears that, for the Li/FeS_2 cell at 2.80 volts, complete removal of lithium from the cathode is observed. The fitted doublets of the spectra at $x = 0.99$ and $x = 2.00$, shown in figure 34, are that of unreacted pyrite in the cathode.

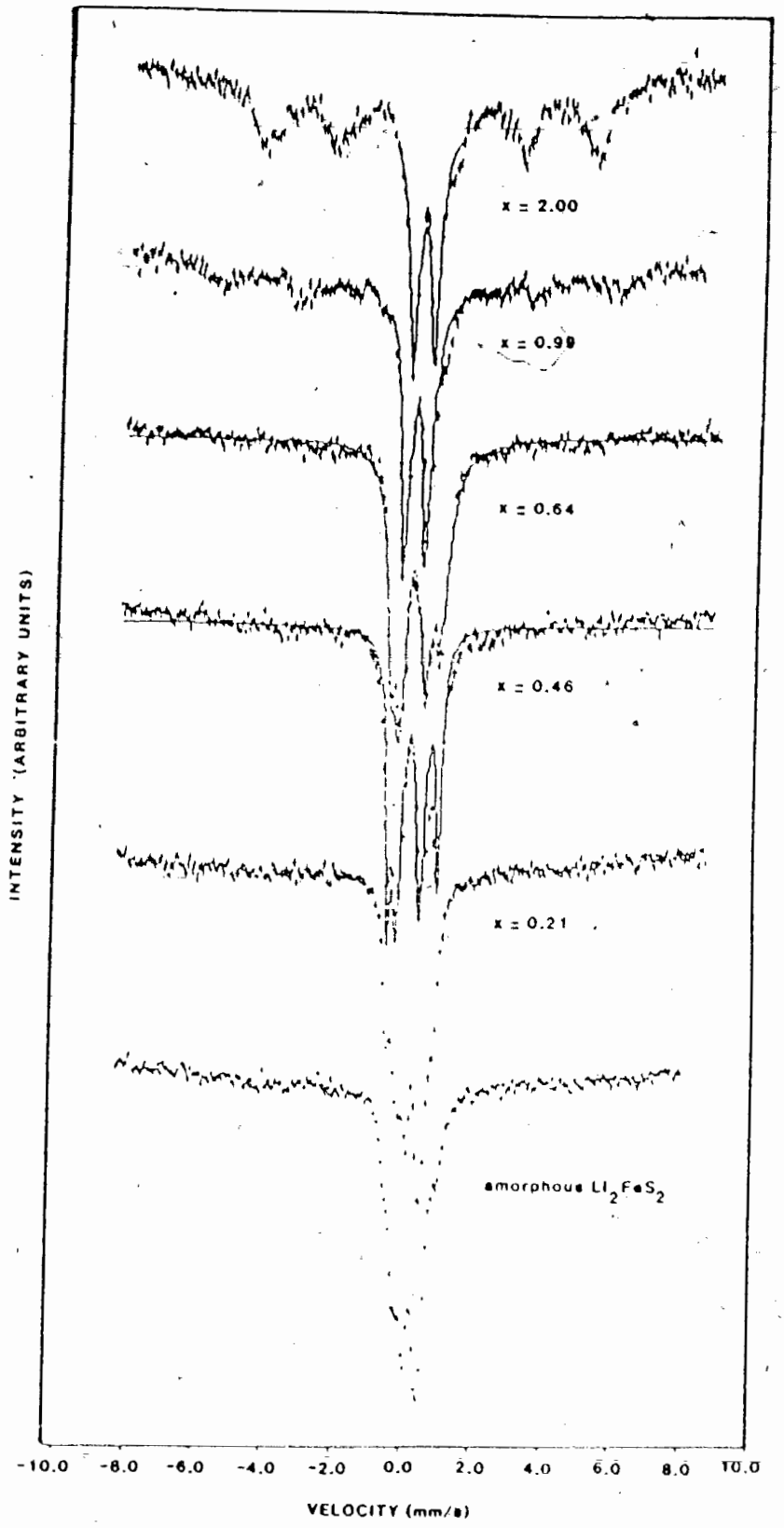

Figure 34. The sequence of Mössbauer spectra obtained at various stages of recharge of a Li/FeS_2 in-situ Mössbauer cell which has been discharged to $x = 2$. The operating temperature of the cell is 55°C.

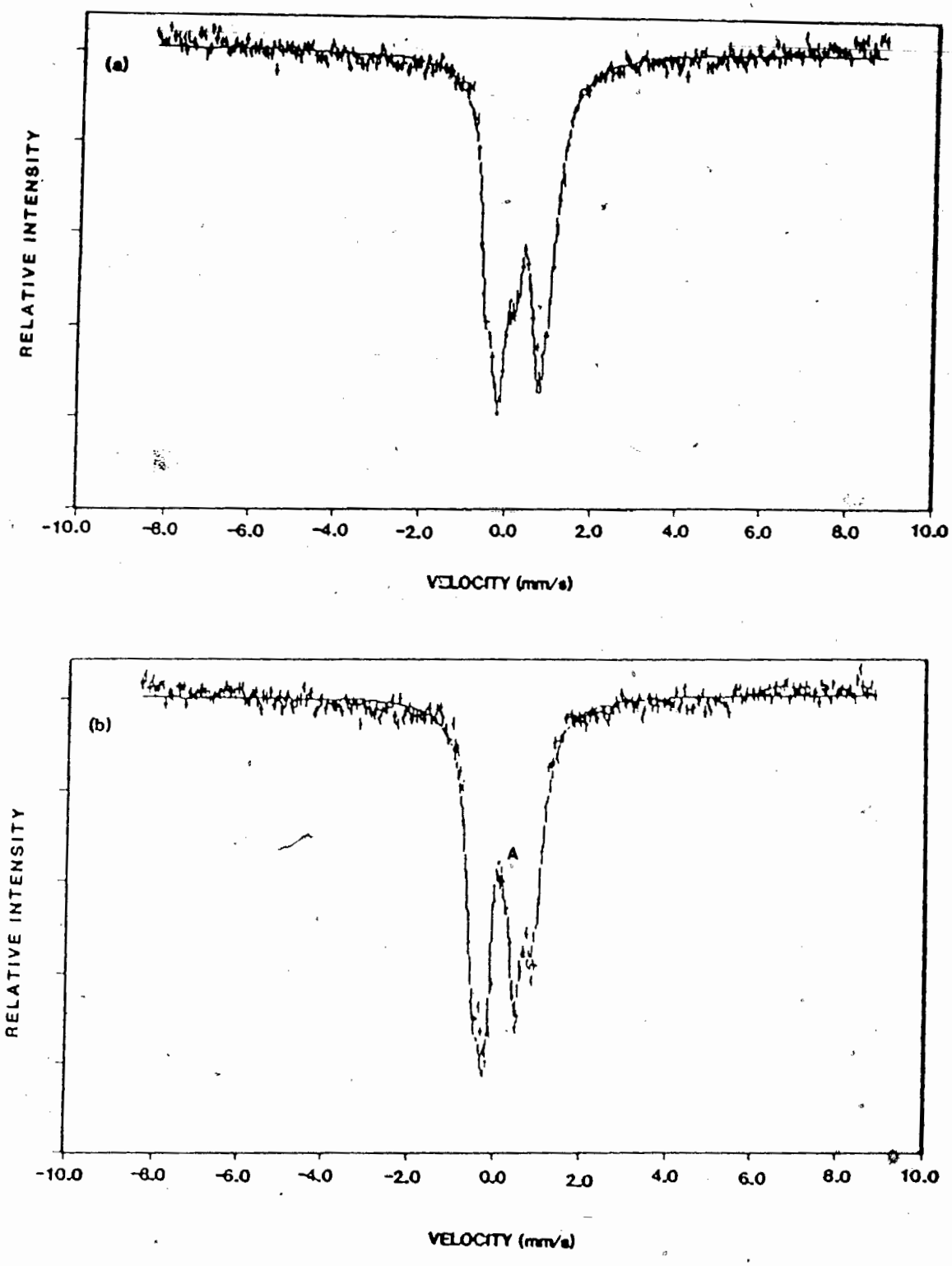

Figure 35. A comparison of the Mössbauer spectra of (a), a Li/Li_2FeS_2 cell at $x = 0.64$ in $Li_{2-x}FeS_2$, to (b) a Li/FeS_2 cell at $x = 0.64$ in $Li_{2-x}FeS_2$. These spectra are taken from the series of spectra in figures 31 and 34.

4.3.3.4 Mössbauer Spectra at Liquid Helium Temperature (4.2°K)

Magnetic hyperfine interactions occur if a magnetic field is present at the iron nucleus. This magnetic field can derive from the atom itself, from the crystal via exchange interactions, or as a result of an externally applied magnetic field. Regardless of how the field originates, it introduces asymmetry into the system such that the nuclear levels of spin I is split into $(2I + 1)$ nondegenerate states. For ^{57}Fe, this results in six magnetic hyperfine lines.

Not all compounds containing unpaired valence electrons show a hyperfine magnetic splitting effect because a factor, known as electronic spin relaxation, must be considered. In paramagnetic compounds, the spin relaxation time is usually short, such that the electronic spins which generate magnetic fields are changing directions very rapidly. The net result is a magnetic field which has a time-average of zero over the time scale of the Mössbauer experiment, and no magnetic splitting is seen. By lowering the temperature, the spin-lattice relaxation time, which involves energy transfer from the spin system to the lattice, is increased. If the spin relaxation is sufficiently slow, the generated magnetic field is nonzero and an interaction with the nucleus which results in magnetic hyperfine splitting can be observed.

Magnetic hyperfine interactions were observed in several of the Mössbauer spectra measured at liquid helium temperature. The spectra of various Li_2FeS_2 and delithiated Li_2FeS_2 samples, as shown in figures 36 and 37, are very complex. For the purpose of this thesis, they are only interpreted qualitatively. These spectra are discussed in sections 4.3.3.1, 4.3.3.2, and 4.3.3.3. In order to determine the ferromagnetism or antiferromagnetism of these samples, further work which involves measurements of these samples in the presence of an applied magnetic field is required.

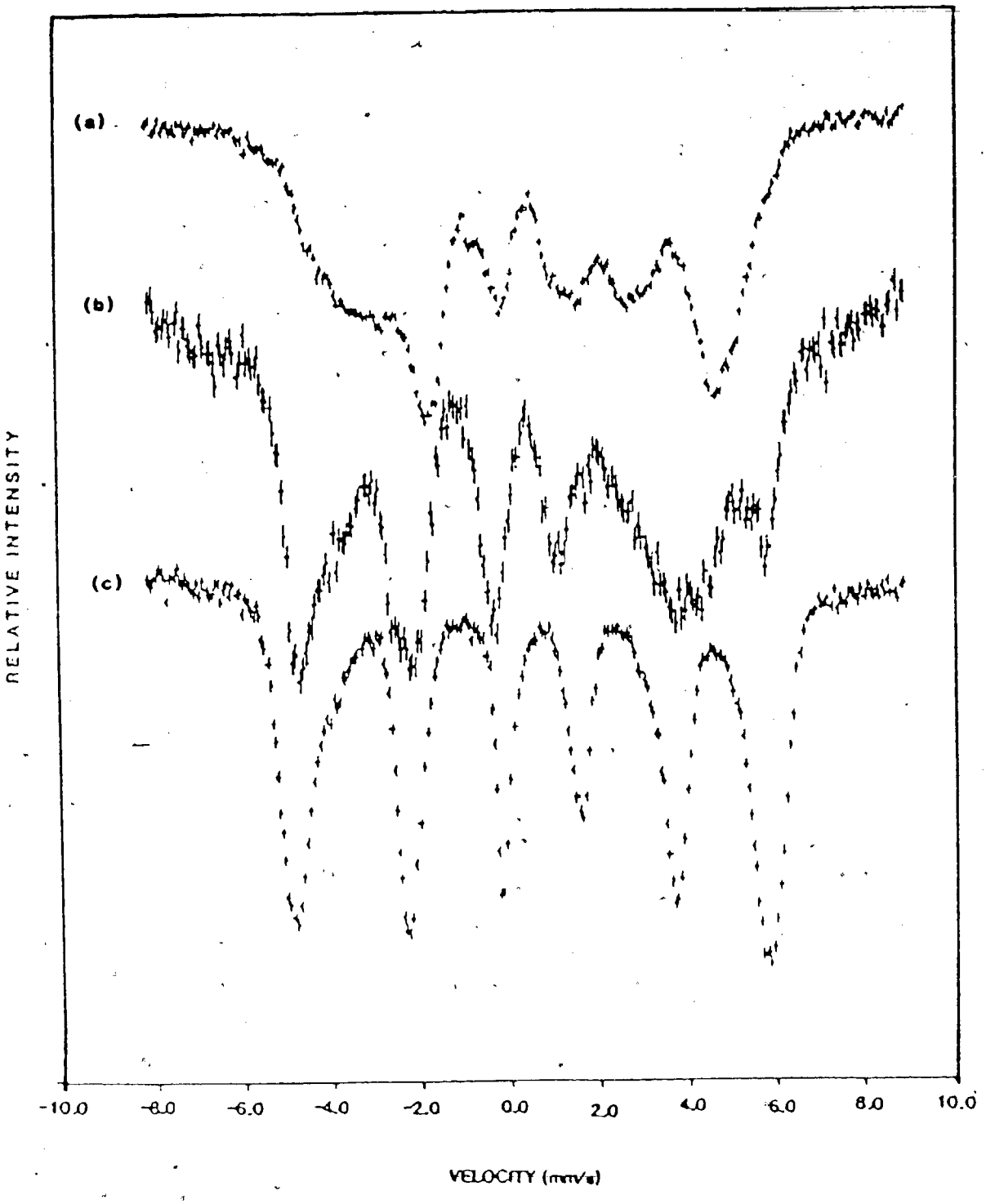

Figure 36. Liquid helium spectra of chemical synthesized compounds: (a) crystalline Li_2FeS_2, (b) delithiated Li_2FeS_2 with I_2/AN; the spectrum is composed of $Li_{2-x}FeS_2$ and FeS_y, and (c) non-stoichiometric FeS_y (where $y = 1.064$) synthesized from its elements.

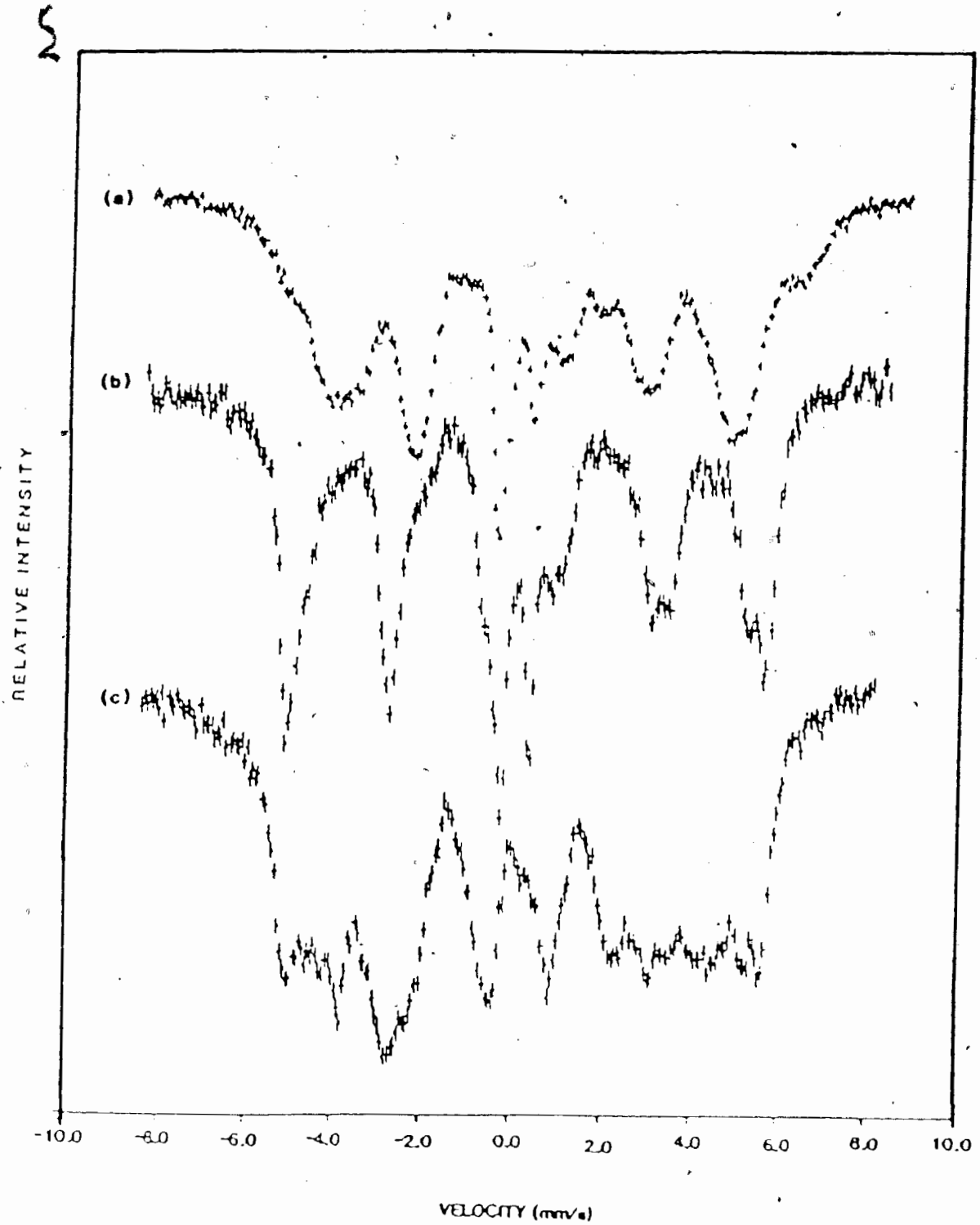

Figure 37. Liquid helium spectra of cathodes: (a) Li/FeS_2 discharged to $x = 2$ at 55°C; the spectrum is composed of an amorphous intermediate Li_2FeS_2 and unreacted pyrite, (b) Li/FeS_2 which has been discharged to $x = 2$ and recharged to 2.80 volts; the spectrum is composed of FeS_y and unreacted pyrite, and (c)Li/Li_2FeS_2 recharged to 2.80 volts; the spectrum is composed of $Li_{2-x}FeS_2$ and FeS_y.

4.3.4 $Li/CuFeS_2$ and $Li/LiCuFeS_2$ Cells

The discharge mechanism of $Li/CuFeS_2$ cells is a one-step reaction. Unlike FeS_2 cells, chalcopyrite cells do not discharge via an intermediate phase. After an initial region of small capacity, a single plateau is observed. The proposed cell reaction,

$$4\ Li + CuFeS_2 \longrightarrow 2\ Li_2S + Cu + Fe \qquad (4.3.8)$$

describes a phase transition in a quartenary system. Therefore, the four co-existing phases on this plateau are $CuFeS_2$, Li_2S, Cu, and Fe. At $x = 4$, the cathode is comprised of a mixture of the reaction products of reaction 4.3.8. Figure 38 shows the first discharge of these cells at temperatures between 21 and 75°C.

The voltage profile of the $Li/LiCuFeS_2$ cell is shown in figure 39. The $V(x)$ curves for the $Li/LiCuFeS_2$ and Li/Li_2FeS_2 cells differ in that for LiCuFeS2 cells, a recharge to 3.4 volts results in a gradual voltage variation with x. For Li_2FeS_2 cells, a plateau at 2.5 volts is observed, because beyond the removal of lithium to $x \simeq 0.8$, the compound disproportionates to FeS_y and S. In contrast, when lithium is removed from $Li_{2-x}Cu_xFeS_2 (0 < x \leq 1)$, well defined Cu_xFeS_2 phase result.

The subsequent discharge of $Li/LiCuFeS_2$ cell, shown in figure 40, exhibits similarities to that of the first discharge of a $Li/CuFeS_2$ cell (figure 38). Therefore, it is believed that the cell reaction at this stage of discharge is

$$(4 - \delta)\ Li + Li_\delta CuFeS2 \longrightarrow 2\ Li_2S + Cu + Fe \qquad (4.3.9)$$

where δ is the amount of lithium which was not removed from the compound after the initial recharge. A further investigation of reactions 4.3.8 and 4.3.9, using in-situ X-ray diffraction, will be discussed in section (4.3.5).

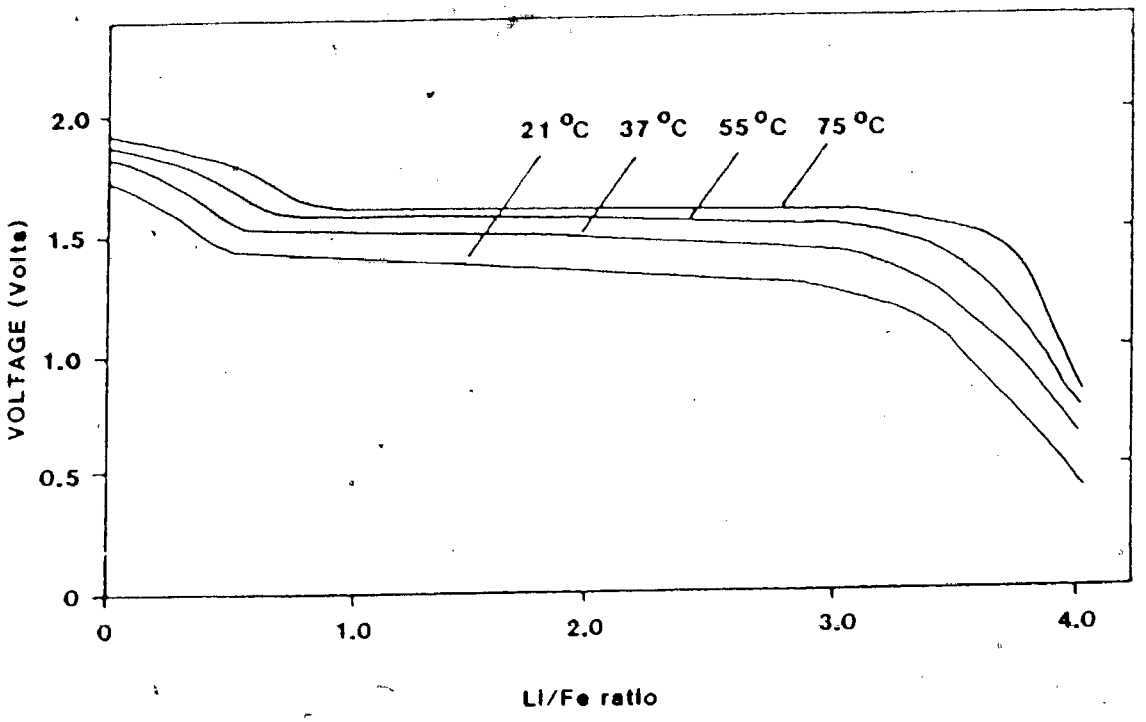

Figure 38: The first discharge of $Li/CuFeS_2$ at temperatures from 21 to 75°C.

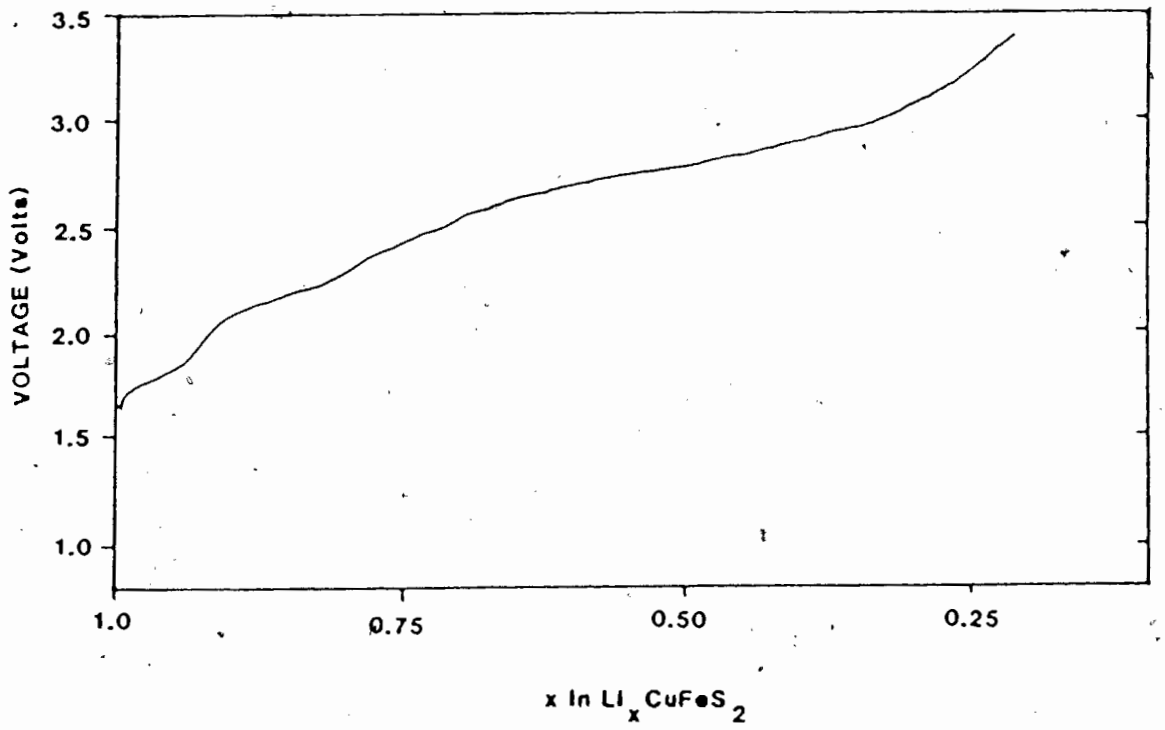

Figure 39: The first recharge of a Li/$LiCuFeS_2$ cell to 3.4 volts.

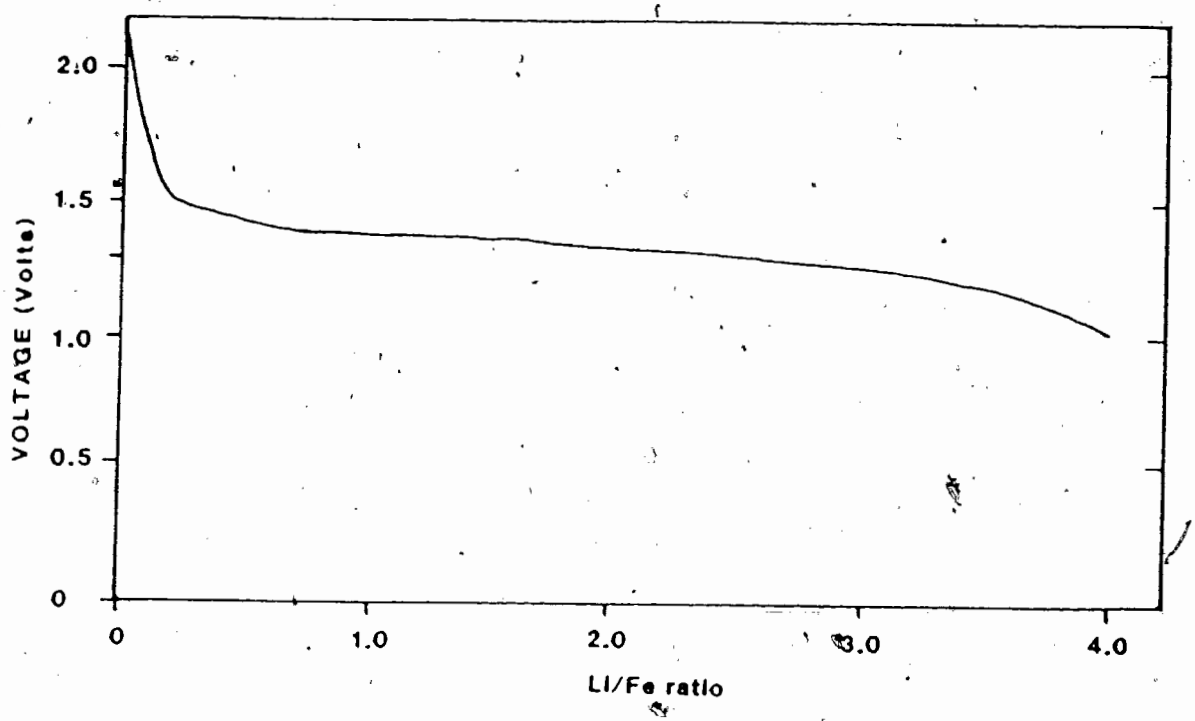

Figure 40: The second discharge of Li/LiCuFeS$_2$ cell.

4.3.5 Gas Evolution Study of $Li/CuFeS_2$ Cells

A gas evolution study at 55°C shows that the small plateau in the initial region of the $Li/CuFeS_2$ cell (figure 38) is due to gas production resulted from electrolyte breakdown.

$$4\ Li(s) + PC(l) + EC(l) \longrightarrow 2\ Li_2CO_3 + propene(g) + ethene(g) \quad (4.3.10)$$

Figure 41a shows $V(x)$ for the first discharge of a $Li/CuFeS_2$ cell assembled as described in sections 2.1.1 and 2.1.2. This cell, which had a 0.068 g cathode, was discharged at a rate of 40 hours for $\Delta x = 1$. Figure 41b shows the volume of gas evolved per gram of $CuFeS_2$ at 50°C and 1 atm. The rate of evolution of gas declines substantially when the cell locks on to the long plateau. By analogy to the gas evolution of propene during discharge of a Li/MoS_2 cell in 1 M $LiAsF_6$/PC electrolyte (9), the gases evolved during the discharge of a $Li/LiCuFeS_2$ cell in 1 M $LiAsF_6$/PC/EC electrolyte are probably propene and ethene.

Although the mechanisms which govern the production of gas are still not well understood, these experiments have shown that the amount of gas produced (ie - the length of the small plateau) is dependent on the operating temperature of the cell. A higher temperature favors electrolyte breakdown, and therefore, increases the production of gas.

The capacity, x_{gas}, for reaction 4.3.10 can be determined by

$$x_{gas} = \frac{n_{Li}}{n_{CuFeS_2}} \quad (4.3.11)$$

where n_{Li}, the moles of Li required to support reaction 4.3.10, is related to the volume of gas produced by the ideal gas law, and n_{CuFeS_2} is the number of moles of $CuFeS_2$. For the first discharge of $Li/CuFeS_2$ at 50°C, 20.6 ml of gas per gram of $CuFeS_2$ was generated. This corresponds to $x_{gas} = 0.50$. Figure 42 shows the temperature dependence of x_{gas}, the small plateau capacity, obtained from the set of discharge curves in figure 38.

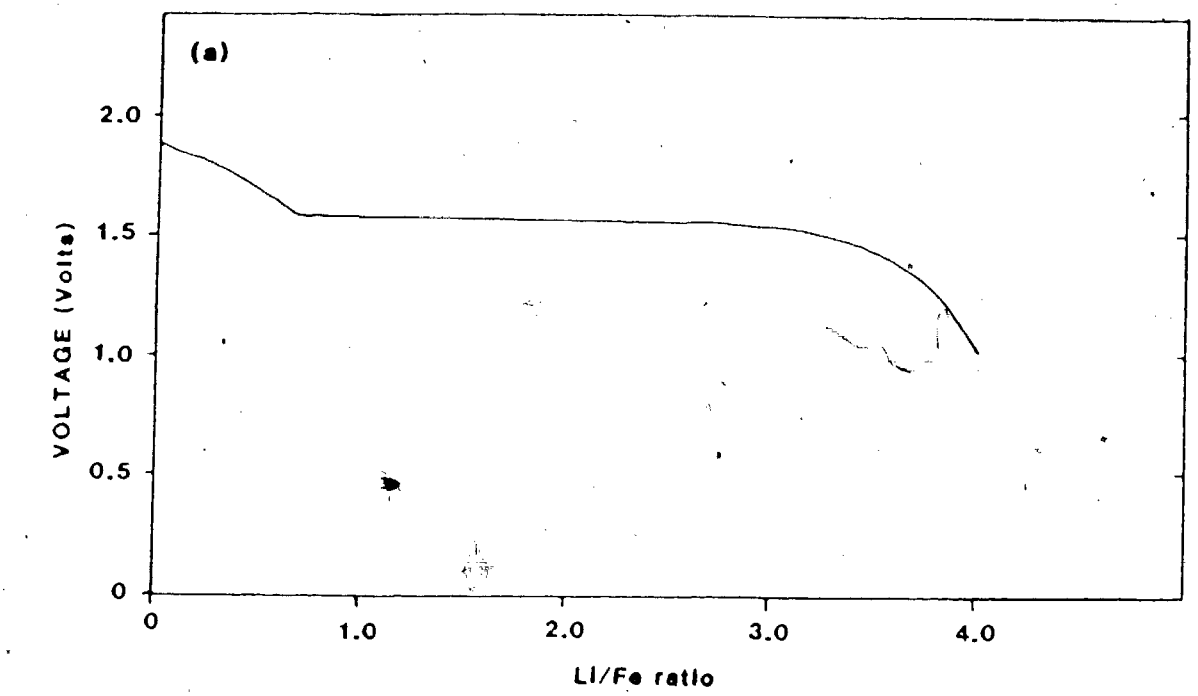

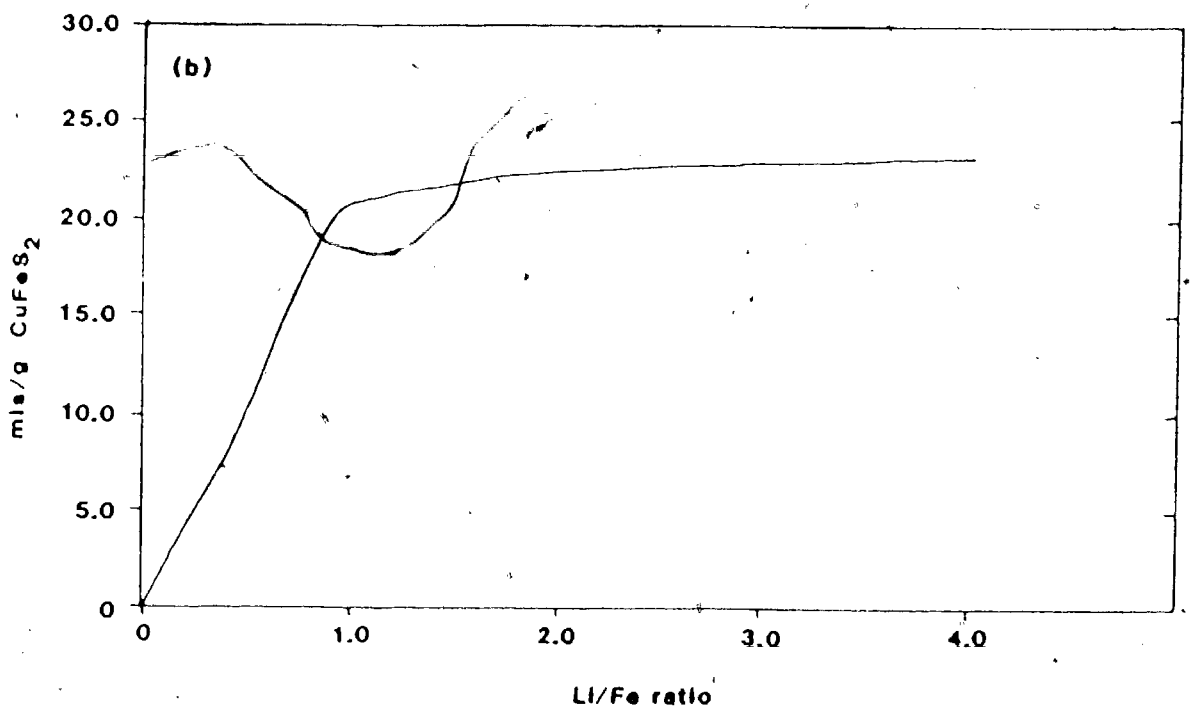

Figure 4: (a) The $V(x)$ curve and, (b) volume of gas evolved vs. x in Li/Li_xCuFeS_2 cell during the first discharge.

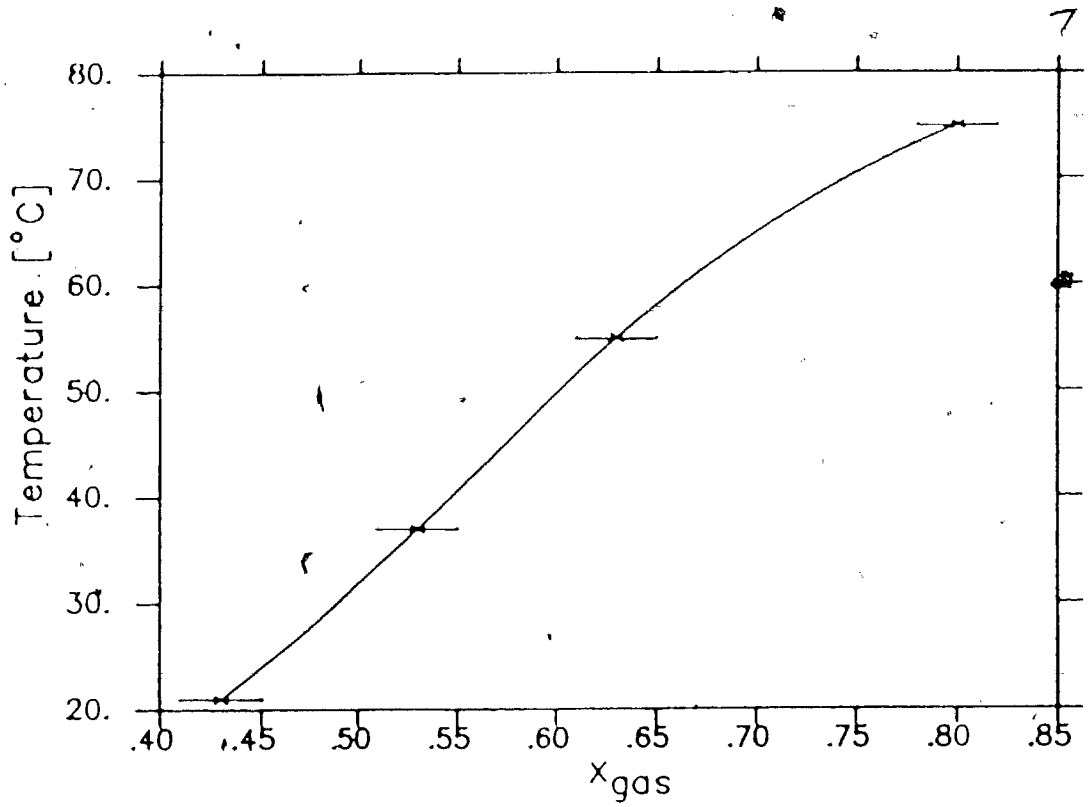

Figure 42: The variation of x_{gas} with temperature.

4.3.6 In-situ X-ray Diffraction Measurements of $Li/LiCuFeS_2$ Cells

Figure 43 shows the voltages at which X-ray measurements are taken along the $V(x)$ curve of a $Li/LiCuFeS_2$ cell. As lithium is removed from $LiCuFeS_2$ electrochemically, the hexagonal framework of this compound does not collapse. Instead, at voltages above 1.45 volts, the unit cell lattice constants can be determined by indexing the powder pattern with a hexagonal cell. Table XIV summarizes the lattice constants of the Li_xCuFeS_2 compound observed at each voltage.

TABLE XIV - Lattice constants of Li_xCuFeS_2 from in-situ X-ray measurements of a $Li/LiCuFeS_2$ cell.

Scan Name	Recharge/ Discharge	Voltage (volts)	Lattice Constants Å	
			a	c
A (Brand new cell)	—	1.76	3.807(2)	6.347(4)
B	recharge	2.40	3.806(2)	6.280(3)
C	recharge	2.80	3.769(2)	6.268(3)
D	discharge	2.20	3.769(1)	6.271(1)
E	discharge	1.80	3.792(2)	6.321(4)
F†	discharge	1.45	—	—

† the diffraction peaks of Li_xCuFeS_2 at this point are very broad. At this voltage, peaks which are due to Li_2S, Cu, and Fe begin to appear in the diffraction patterns.

From the knowledge of the crystal structure of the partially deintercalated compound, $Li_{1-\delta}CuFeS_2$, as discussed in section 4.2.3, the mechanism of the initial recharge of the $Li/LiCuFeS_2$ cell becomes obvious. As lithium is removed from the octahedral sites in layer 2, copper atoms from the tetrahedral sites in layer 1 gradually fill the tetrahedral sites in layer 2. At 2.80 volts (scan C) the measured lattice constants, $a = 3.769(2)$Å and $c = 6.268(3)$Å, differ from those determined using I_2/AN (sample K; $a = 3.706(1)$Å and $c = 6.169(3)$Å). The observed difference is not understood, but is believed to have resulted from poor kinetics of the in-situ X-ray cell at this voltage. Therefore, although scan C was measured when the current flow through the cell was less than 5μamps, the kinetics, which

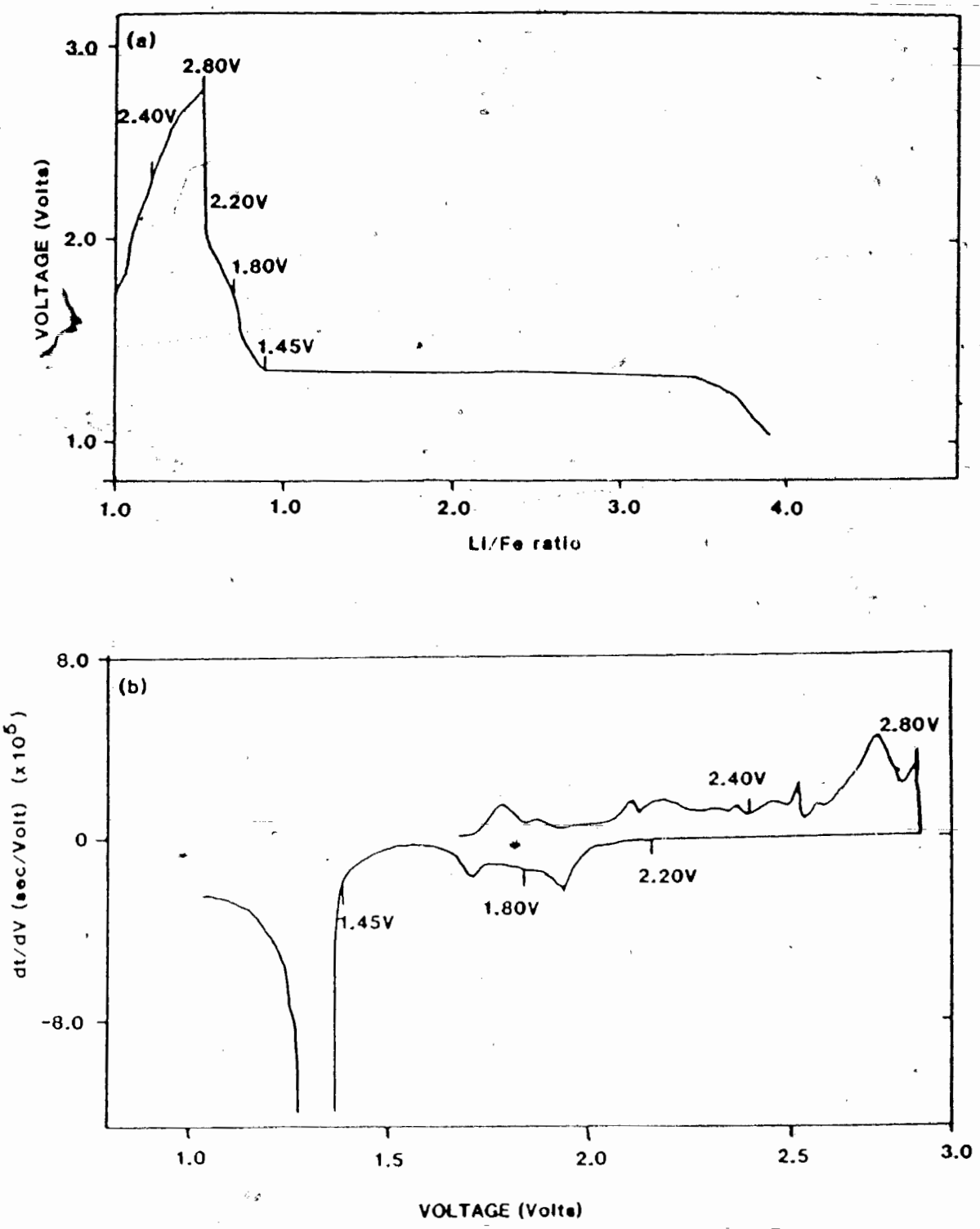

Figure 43. (a) The $V(x)$ curve of the first charge and discharge of $Li/LiCuFeS_2$. (b) The dt/dV vs. V curve of (a). Indicated on these curves are the voltages at which X-ray spectra are measured.

are governed by the diffusion of lithium, are so slow that not all the lithium within the cathode is removed. In contrast, chemical delithiation (sample Q) proceeds to completion under vigorous stirring for 2-3 days with material less than 0.05 mm in size. This ensures good chemical contact of each cathode particle with iodine, which is present in excess, such that poor kinetics may be overcome. At 1.45 volts (scan F), the diffraction peaks of Li_xCuFeS_2 are very broad. The hexagonal framework begins to decompose, and, as shown in figure 44, Li_2S, Fe, and Cu begin to appear. Thus, it is evident that as $Li/CuFeS_2$ and $Li/LiCuFeS_2$ cells are discharged across the plateau at approximately 1.2 volts, reactions 4.3.8 and 4.3.9 occur respectively.

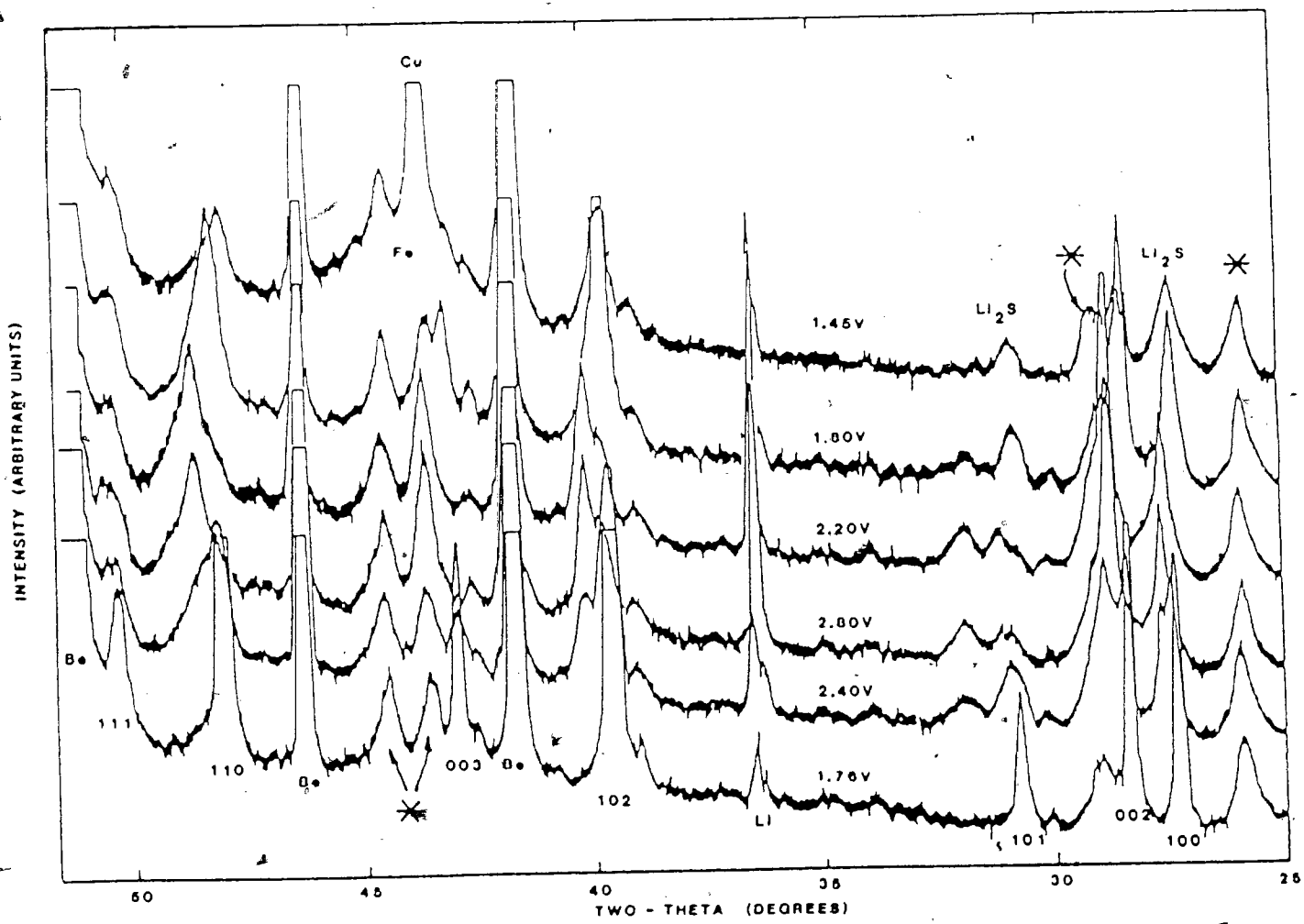

Figure 44. Portions of the X-ray diffraction patterns of the Li/$LiCuFeS_2$ in-situ X-ray cell. The diffraction peaks due to $LiCuFeS_2$ are labelled. '*' indicates extraneous peaks due to the cell holder and the separator in the cell. 'Be' indicates peaks due to beryllium.

4.4 Calorimetric Measurements

4.4.1 Delithiated Li_2FeS_2

As mentioned in section 4.3.3.1, the Mössbauer spectrum of chemically delithiated Li_2FeS_2 (sample K, prepared by I_2/AN) measured at 4.2°K indicates the presence of a $Li_{2-x}FeS_2$ phase. This suggests that under vigorous stirring for 20 hours, the removal of lithium from Li_2FeS_2 remains incomplete. It was thought that an investigation of the thermal stability of the delithiated mixture by DSC may lead to an understanding of the products of recharge of a Li/Li_2FeS_2 cell.

Calorimetric data of the delithiated powder, recorded as a plot of $\frac{dH}{dt}$ vs temperature, are shown in figure 45. The 0.028 g sample was heated at a rate of 10°C/min from 25°C to 550°C. At temperatures below 265°C the spectrum contains two peaks, an endothermic peak at 118°C, and an exothermic peak at 197°C. Beyond 265°C, the spectrum, which consists of overlapping exothermic peaks, is very complex. X-ray diffraction spectra of the powder, which had been heated to temperatures of 235°C and 550°C, are measured.

The endothermic peak at 118°C corresponds to the melting of sulfur. Since the heat of fusion for sulfur is 38.309 joules/gram (29), the amount of melted sulfur, calculated by integrating under the endothermic peak, is 0.004(1) g. The exothermic peak at 197°C corresponds to the heat of reaction of FeS_2 from FeS and S.

$$FeS + S \longrightarrow FeS_2 \qquad (4.4.1)$$

Theoretically, the heat of reaction, ΔH_f, of reaction 4.4.1 can be calculated from the heats of formation of FeS and FeS_2 from its elements. These are -89.33 KJ/mole and -154.31 KJ/mole respectively (29). Hence, the heat of reaction of reaction 4.4.1 is -64.98 KJ/mole. Assuming that the entire sample consists of FeS and S, integration of the exothermic peak yields an experimental heat of reaction of -23.14 KJ/mole. The calculated ΔH_f and weight of melted sulfur consistently show that only approximately

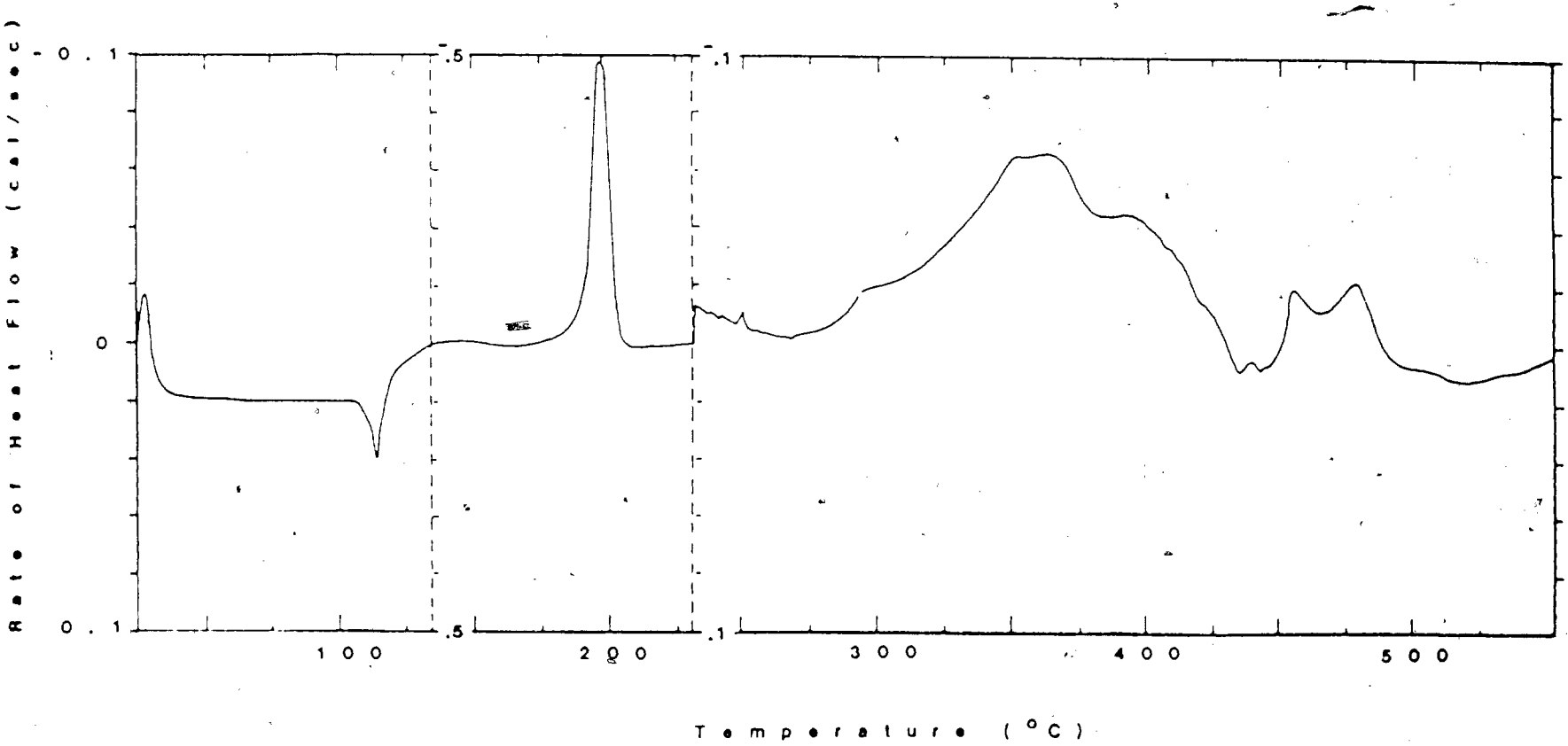

Figure 45. Calorimetric data of delithiated Li_2FeS_2.

35% of the powder is FeS and S. Mössbauer spectroscopy suggests that the remainder of the powder may be $Li_{2-x}FeS_2$. However, it is not possible to draw any further conclusions from the present data.

The X-ray diffraction pattern, measured at 235°C, confirms that the product is marcasite, the orthorhombic form of FeS_2. At 550°C, some residual marcasite is observed, but the diffraction pattern is dominated by peaks which are due to pyrite, the cubic form of FeS_2.

4.4.2 Delithiated $Li_{2-x}Cu_xFeS_2$

Calorimetric data on chemically delithiated $Li_{\frac{1}{3}}Cu_{\frac{2}{3}}FeS_2$ (sample O) and $LiCuFeS_2$ (sample Q) are shown in figure 46 and 47. Both samples were heated at a rate of 10°C/min from 25°C to 550°C. Because of the complexity of these spectra, interpretation of the data, aided by the diffraction patterns measured at different temperatures, is purely qualitative.

Delithiated $Li_{\frac{1}{3}}Cu_{\frac{2}{3}}FeS_2$ and $LiCuFeS_2$ data show a small endothermic peak near 118°C which corresponds to the melting of sulfur. The size of the peak indicates that both delithiated samples contained trace amounts of sulfur. In the delithiated $Li_{\frac{1}{3}}Cu_{\frac{2}{3}}FeS_2$ data, broad peaks near 205°C and 530°C were observed. Diffraction pattern measured at 355°C indicates that the products of the exothermic reaction near 205°C are the naturally ocurring minerals chalcopyrite, $CuFeS_2$, and marcasite, FeS_2. The reaction can be described in terms of the phase transition

$$Cu_{\frac{2}{3}}FeS_2(\text{hexagonal}) \longrightarrow \tfrac{2}{3}\ CuFeS_2(\text{tetragonal}) + \tfrac{1}{3}\ FeS_2(\text{orthorhombic}) \qquad (4.4.2)$$

At 447°C and 550°C, the diffraction pattern remains that of chalcopyrite, but FeS_2 is present as a mixture of marcasite and pyrite.

The general features observed in the delithiation of $Li_{\frac{1}{3}}Cu_{\frac{2}{3}}FeS_2$ are also observed for delithiated $LiCuFeS_2$. The exothermic reaction which occurred near 205°C, now occurs near 340°C. Diffraction spectra of the powder which had been ramped to temperatures of 365°C and 550°C both display the powder patterns of chalcopyrite. Thus, it is evident that the Cu_xFeS_2 phase, prepared by I_2/AN, is a metastable phase at room temperature. At elevated temperatures it undergoes a phase transition to form chalcopyrite.

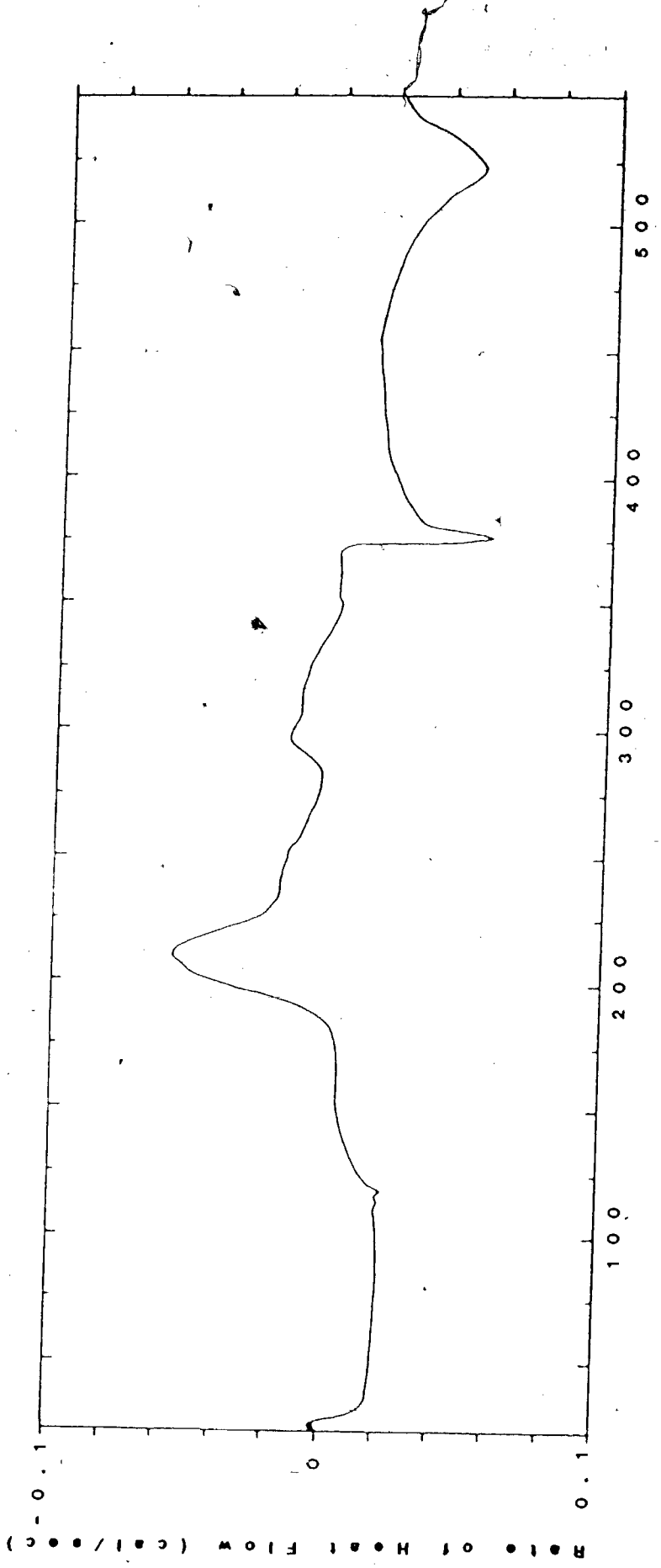

Figure 46. Calorimetric data of delithiated $Li_{\frac{1}{3}}Cu_2FeS_2$.

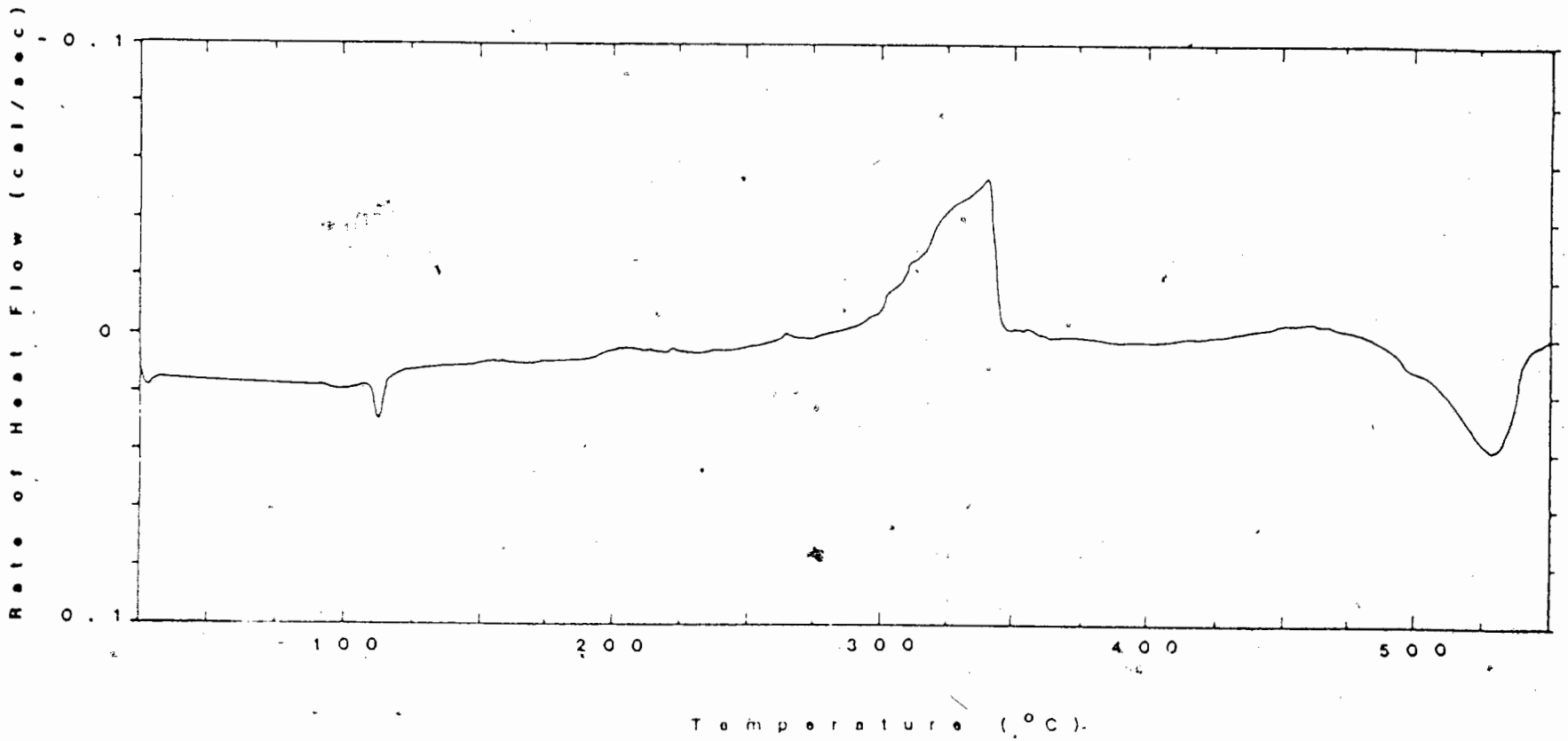

Figure 47. Calorimetric data of delithiated $LiCuFeS_2$.

4.4.2.1 Metastable Cu_xFeS_2 and Chalcopyrite

The structure of chalcopyrite contains four molecules in a tetragonal unit of the dimensions, $a = 5.24$Å, and $c = 10.30$Å (30). The atomic arrangement is essentially that of zinc blende, where metallic atoms are surrounded by tetrahedra of sulfur atoms, while each sulfur atom in turn resides in a tetrahedron; formed by two iron atoms and two copper atoms. Figure 48 shows the atom arrangement of zinc and sulfur atoms in zinc blende. Two views are shown, one down an axis and the other, in the [111] direction, to emphasize the layers of metal and sulfur atoms. In the latter view, the planar sulfurs form a honeycomb hexagonal lattice. Geometric calculations show that the planar S-S distance is 3.71Å. In the notation of hexagonal close-packed layers, chalcopyrite has a three layer sulfur stacking sequence, and can be described by the stacking symbol

$$A_a B_b C_c A_a B_b C_c A_a$$

where the capital letters denote the relative sequence of the sulfur layers, the small letters represent the Cu and Fe atoms, in a 1:1 ratio occupying half of the tetrahedral sites between two layers of sulfur. Figure 49a is a schematic diagram of such an arrangement. The interplanar S-S distance, from S_A to S_C, is calculated to be 6.1Å. This distance is equivalent to the two layers sulfur stacking sequence, as observed in the Cu_xFeS_2 phase, where x=1.

The metastable Cu_xFeS_2 phase, where $x = 1$, has a unit cell dimension of $a = 3.708(1)$Å and $c = 6.188(2)$Å. The schematic diagram in figure 49b shows the major difference in the arrangement of metal atoms of this phase and that of chalcopyrite. The Cu and Fe atoms of the metastable phase do not reside between the same layers of sulfur. Instead, the Cu and Fe atoms occupy the tetrahedral sites in alternating layers of sulfur. Since the dimension of the hexagonal framework is almost identical to that of chalcopyrite, the phase transition from metastable Cu_xFeS_2 to chalcopyrite becomes easy to envisage. Upon heating, when enough energy is supplied, the sulfur planes slip, and the metal atoms within the hexagonal framework undergo rearrangement into new positions such that a minimum free energy state in the crystal is achieved. This lowest energy state, not surprisingly,

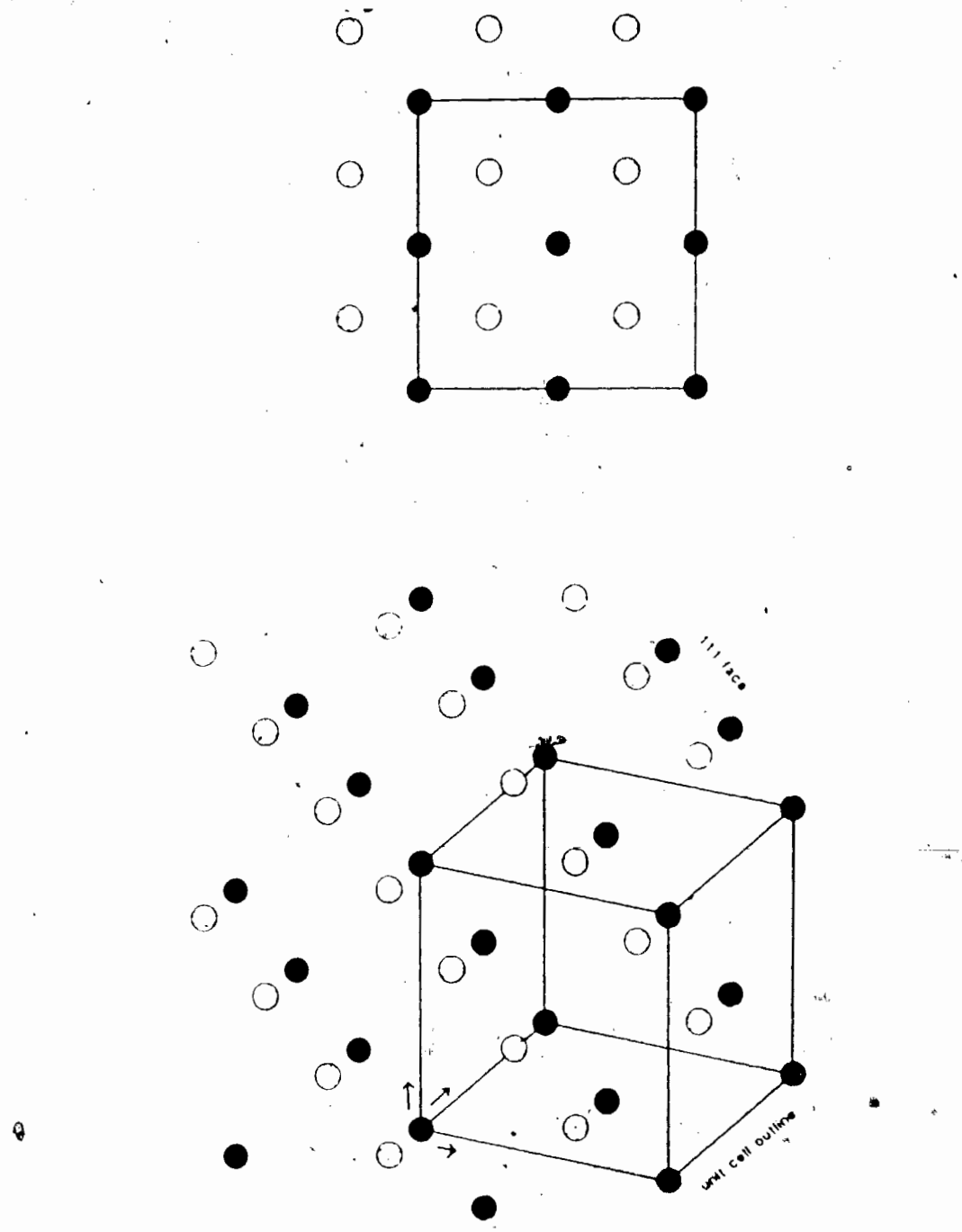

Figure 48. The structure of zinc blend, showing the arrangement of the zinc and sulfur atoms. Two views are shown, one down an axis and the other to show the planes of atoms in the [111] direction.

occurring mineral, chalcopyrite.

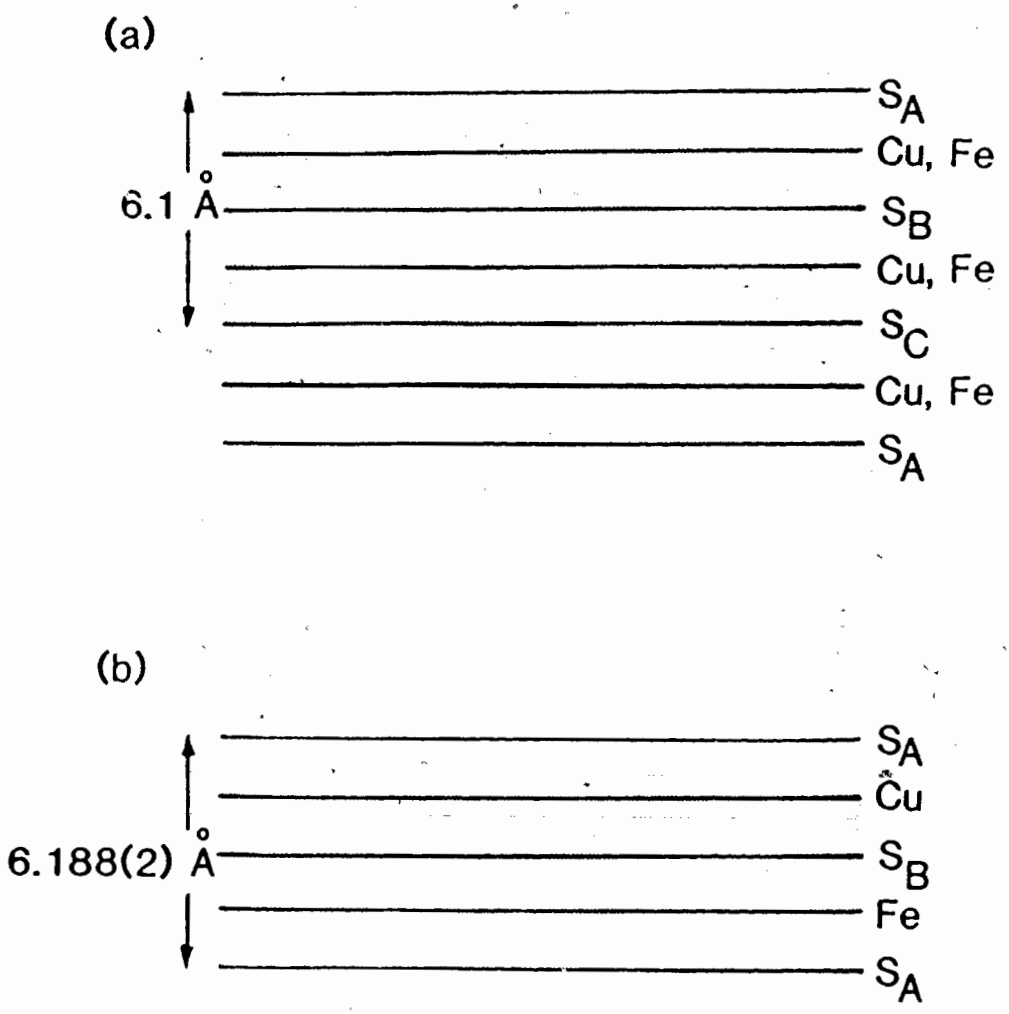

Figure 49. A schematic diagram of the stacking sequence of (a) chalcopyrite in the [111] direction, and (b) the layered Cu_xFeS_2 phase, where $x = 1$.

5 SUMMARY AND SUGGESTIONS FOR FUTURE WORK

5.1 Summary of the Thesis

The purpose of this thesis was to investigate the chemistry and electrochemisty of pyrite and chalcopyrite as ambient temperature lithium rechargeable battery electrodes. The thesis began with a brief introduction to the concept of intercalation, and a summary of the previous work, which contained many incorrect speculations based on analogies to the well-known intercalation system Li_xTiS_2. Fabrication of the different types of electrochemical cells and methods of chemical syntheses of materials which were used in this study were described.

The thermodynamics of an intercalation battery, based on the analogy to the isotherm of a gas, was reviewed. Based on the similarity of the two systems, a set of thermodynamic quantities for the intercalation battery was derived (section 3.2.2). From these fundamental quantities, features of $V(x)$, and $-\frac{dx}{dV}$ curves can be used to detect first order phase transitions. The methods of measurements and the interpretations of these quantities are described (sections 3.2.4 and 3.2.5). Other techniques which were used to aid in verifying the interpretations of the $V(x)$ curves were discussed.

Experimental results were presented in chapter four. A summary of the results is given below.

1. In the high temperature Li_xFeS_2 series ($0 < x \leq 2$), $LiFeS_2$ is the only compound which exists in pure form. This compound forms at a temperature of 300°C (section 4.1.1).

2. Copper substitution for one of the two types of lithium in Li_2FeS_2 results in a series with composition $Li_{2-x}Cu_xFeS_2$ where, over the range of $0 < x \leq 1$, a solid solution forms (section4.2.1).

3. The crystal structures of lithiated pyrite, Li_2FeS_2, and lithiated chalcopyrite, $LiCuFeS_2$, were determined (sections 4.1.2, and 4.2.2). These materials are synthesized at high temperatures from the naturally occurring minerals pyrite and chalcopyrite.

4. The crystal structure of a partially delithiated compound, $Li_{1-\delta}CuFeS_2$, was determined (section 4.2.3). As lithium atoms are removed from the compound, copper atoms move from one layer of sulfur to another.

5. A $LiFe_{1.5}S_2$ crystal was selected from a batch of Li_2FeS_2 powder. Its structure was determined (section 4.1.3). Attempts to synthesize this phase at temperatures above 300°C were unsuccessful. Thus $LiFe_{1.5}S_2$ is not a stable phase above 300°C (section 4.1.4).

6. Upon the removal of lithium from Li_2FeS_2 with I_2/AN, disproportionation of the compound is observed. The reaction product is a mixture of partially delithiated $Li_{2-x}FeS_2$, FeS_y, and S (section 4.3).

7. Calorimetric measurements on delithiated Li_2FeS_2 show that only approximately 35% of the mixture is comprised of FeS_y and S. The remaining 65% is made up of the partially delithiated phase, $Li_{2-x}FeS_2$. Upon heating, FeS and S react to form marcasite, which then undergoes phase transition to pyrite (section 4.4.1).

8. Delithiated $Li_{2-x}Cu_xFeS_2$ ($0 < x \leq 1$) with I_2/AN results in well-defined Cu_xFeS_2 phases. A gradual variation of the lattice parameters of this series with x is observed. The structures of these compounds are similar to natural chalcopyrite but has Cu and Fe atoms between different sulfur planes (section 4.2.1).

9. When heated to 550°C, the metastable Cu_xFeS_2 phases, for $x < 1$, undergo phase transitions to form chalcopyrite, marcasite, and pyrite. For $x = 1$, only chalcopyrite is formed (section 4.4.2). The dimensions of the honeycomb hexagonal sulfur framework of Cu_xFeS_2 and chalcopyrite are almost identical. Therefore, phase transitions at high temperature only involve minor sulfur slipping and rearrangements of the metal atoms in the crystal lattice (section 4.2.3).

10. The discharge mechanism of the first discharge of a Li/FeS_2 cell at high discharge rate at room temperature is

$$4\ Li + FeS_2 \longrightarrow 2\ Li_2S + Fe$$

At temperatures above 37°C, and at low rate discharge at room temperature, the reaction proceeds step-wise, forming an intermediate phase, Li_2FeS_2 (section 4.3.1).

$$2\ Li + FeS_2 \longrightarrow Li_2FeS_2$$
$$2\ Li + Li_2FeS_2 \longrightarrow 2\ Li_2S + Fe$$

Related experiments to confirm these equations are found in sections 4.3.1, and 4.3.3.

11. The first and second discharges of a Li/FeS_2 cell bear no resemblance since at the start of the second discharge, the cathode does not comprise the starting material, pyrite. Instead, it contains a mixture of FeS_y and S (section 4.3.1).

12. The chemistries of Li/FeS_2 cells and Li/Li_2FeS_2 cells, after a complete discharge to 1.0 volt, are the same (section 4.3.1).

13. In the Li/Li_2FeS_2 cell, the reversible voltage range is between 1.45 and 2.45 volts. This corresponds to $0 < x < 0.8$ in $Li_{2-x}FeS_2$, where the observed cycling mechanism is that of intercalation. Beyond this

range, new phases with other Fe:S ratios are formed (section4.3.2).

14. A Mössbauer study shows that in the initial stage of recharge of a Li/Li_2FeS_2 cell, there is evidence that indicates that the species which undergoes oxidation is iron. The rate at which the two different types of iron in Li_2FeS_2 undergo oxidation is significantly different (section 4.3.3.3).

15. The discharge mechanism of $Li/CuFeS_2$ cells is

$$4\ Li + CuFeS_2 \longrightarrow 2\ Li_2S + Cu + Fe$$

(section 4.3.4, and 4.3.6). Unlike Li/Li_2FeS_2 cells, an intermediate phase is not formed (section 4.3.4). In the initial region of discharge, gas production resulting from electrolyte breakdown is observed (section 4.3.5).

5.2 Suggestions for Future Work

In this thesis, we have discussed the chemistry and electrochemical reactions of cells fabricated with pyrite and chalcopyrite. More experiments are required to probe into the mechanisms which are responsible for the subtle features observed in the voltage curves.

Measurements of the changes in electronic properties such as conductivity, and magnetic susceptibility as a function of temperature would be useful. Further structural work includes investigating the occurrence of lithium ordering in Li_2FeS_2 and $Li_{2-x}FeS_2$, and growing crystals of fully delithiated Cu_xFeS_2 phases. In-situ resistivity measurements of these electrochemical cells are required in order to understand the kinetics of these materials. Variable temperature Mössbauer measurements on the starting materials may yield useful information on magnetic interactions which may facilitate the interpretation of the complex spectra observed at 4.2°K. Finally, a detailed study of synthesis is required in order to study the $LiFe_{1.5}S_2$ phase, as it has the characteristics of an intercalation compound.

6 BIBLIOGRAPHY

1. R.R. Haering, J.A.R. Stiles, and K. Brandt U.S. Patent 4224390 (1980).

2. A.E. Martin, in "High Performance Batteries for Electric Vehicle Propulsion and Stationary Energy Storage", Argonne National Laboratory Report ANL-78-94, p.167 (1980).

3. Z. Tomczuk, B. Tani, N.C. Otto, M.F. Roche and D.R. Vissers, J. Electrochem. Soc., **129**, 926 (1982).

4. R.A. Sharma, J. Electrochem. Soc., **123**, 448 (1976).

5. C.A. Melendres and B. Tani, J. Phys. Chem., **82**, 2850 (1978).

6. R. Brec and A. Dugast, Mater. Res. Bull., **15**, 619 (1980).

7. J.R. Dahn, W.R. McKinnon, R.R. Haering, W.J.L. Buyers and B.M. Powell, Can. J. Phys., **58**, 207 (1980).

8. S.P.S. Badwal and R.J. Thorn, J. Solid State Chem., **43**, 163 (1982).

9. R. Fong, M.C. Reid, R.S. McMillan, and J.R. Dahn, J. Electrochem. Soc., **134**, 516 (1987).

10. J.R. Dahn, M.A. Py, and R.R. Haering, Can. J. Phys., **60**, 307 (1982).

11. D.W. Murphy, and P.A. Christian, Science, **205**, 651 (1979).

12. B.D. Cullity, "Elements of X-ray Diffraction", Second Edition, Addison-Wesley Publishing Company, Inc. (1978).

13. J.R. Dahn, and W.R. McKinnon, J. Electrochem. Soc., **131**, 1825 (1984).

14. J.R. Dahn, and R.R. Haering, Solid State Ionics, **2**, 19 (1981).

15. A. Le Mehaute, R. Brec, A.Dugast, and J. Rouxel, Solid State Ionics, **3/4**, 185 (1981).

16. P. Gard, C. Sourisseau, G.Ouvrard, and R. Brec, Solid State Ionics, **20**, 231 (1986).

17. "International Tables for X-ray Crystallography"; Kynoch Press: Birmingham, England, (1974); Vol. IV, Tables 2.2B and 2.3.1.

18. E.J. Gabe, A.C. Larson, F.L. Lee, Y. LePage, NRC VAX Crystal Structure System. Ottawa, National Research Council (1984).

19. N.N. Greenwood, and T.C. Gibb, "Mössbauer Spectroscopy", Chapman and Hall Ltd. (1971).

20. L. May, "An Introduction to Mössbauer Spectroscopy", Plenum Press (1971).

21. M. Hansen, "Contribution of Binary Alloys", Second Edition, McGraw-Hill Book Company (1985).

22. R.J. Batchelor, F.W.B. Einstein, C.H.W. Jones, R. Fong, and J.R. Dahn, "The Crystal Structure of Li_2FeS_2" - accepted by Phys. Rev. B.

23. J. E. C. Battery Newsletter **2**, 23 (1987).

24. J.T. Hoggins, and H. Steinfink, Inorganic Chem., **15**, 1682 (1976).

25. J.B. Goodenough, and G.A. Fatseas, J. Solid State Chem., **41**, 1 (1982).

26. J.B. Goodenough, Mat. Res. Bull., **13**, 1305 (1978).

27. H.Y. Hong, and H. Steinfink, J. Solid State Chem., **5**, 93 (1972).

28. W.M. Reiff, I.E. Grey, A. Fan, Z. Eliezer, and H. Steinfink, J. Solid State Chem., **13**, 32 (1975).

29. CRC Handbook of Chemistry and Physics, CRC Press Inc., 68th edition.

30. R.W.G. Wyckoff, Crystal Structures, Volume 2, Interscience Publishers, (1960).